8-10-2015

Nanomaterials Based Fluorescent Sensors for Sensitive and Selective Nitro-explosives Detection

Xiangcheng Sun
xiangcheng.sun@uconn.edu

Nanomaterials Based Fluorescent Sensors for Sensitive and Selective Nitro-explosives Detection

Xiangcheng Sun, Ph.D.

University of Connecticut, 2015

The reliable detection of explosives is one of the pressing concerns in anti-terrorism efforts and environmental pollution controls. Up to date, fluorescence-based sensing technology represents one of the most promising approaches for trace explosives detection due to the advantages such as short response time, excellent sensitivity, and instrumental simplicity. The Ph.D. project aims at developing novel fluorescent nanomaterials for fast, sensitive, selective, reliable and cost-effective detection of nitro-explosives.

Early research focused on the pyrene-doped polymer systems. Firstly, pyrene-polystyrene fluorescent nanoporous films have been prepared through a simple dip-coating process, and used for explosives vapour detection with ultra-sensitivity and selectivity. Morphology investigations revealed that the fluorescent polymer films consisted of a large-surface, three-dimensional nanoporous array of holes and the possible molecular origin of fluorescence quenching was investigated through structural XRD studies and the electronic structure of the polymer film. Later super-hydrophobic sand was prepared and applied for buried explosives detection. In order to detect nitro-explosives in aqueous phase, pyrene-polyethersulfone electrospun nanofibers were synthesized through electrospinning. The effects of mixed solvent ratio and polymer/fluorophore concentrations on nanofiber's morphology as well as its sensing performance were systematically investigated and optimized. The current sensor demonstrated excellent sensitivity, selectivity and reusability to nitro-explosives detection. Further fluorescence lifetime studies have revealed a dominant static quenching mechanism.

An ultrafast and facile method for the preparation of fluorescent nitrogen-doped carbon nanoparticles (CNPs) has also been developed from a single precursor (ammonium citrate dibasic) under microwave conditions. The obtained CNPs showed strong blue fluorescence, which could be quenched by picric acid sensitively and selectively. Furthermore, fluorescent carbon dots co-doped with nitrogen and phosphorus were synthesized with high quantum yield and dual (blue and green) fluorescence emission, and applied as ratiometric sensors for explosives detection. Finally, a fully biodegradable and environmental-friendly biopolymer (protein) showed sensitive, selective and rapid detection of picric acid, and its excellent sensing performance was attributed to the synergistic effect of the low molecular orbital, presence of fluorescent resonance energy transfer as well as acid-base interactions. This dissertation opens an avenue in the design and synthesis of fluorescent nanomaterials for wide applications beyond nitro-explosives detection.

Nanomaterials Based Fluorescent Sensors for Sensitive and Selective Nitro-explosives Detection

Xiangcheng Sun

B.E., Harbin Institute of Technology, **2008**

M.E., Graduate University of Chinese Academy of Sciences, **2011**

A Dissertation
Submitted in Partial Fulfillment of the
Requirements for the Degree of

Doctor of Philosophy

at the

University of Connecticut

2015

APPROVAL PAGE

Doctor of Philosophy Dissertation

Nanomaterials Based Fluorescent Sensors for Sensitive and Selective Nitro-explosives Detection

Presented by

Xiangcheng Sun, M.E.

Major Advisor _____
Dr. Yu Lei

Associate Advisor _____
Dr. Christian Brückner

Associate Advisor _____
Dr. Mu-Ping Nieh

Associate Advisor _____
Dr. Steven L. Suib

Associate Advisor _____
Dr. Jing Zhao

University of Connecticut
2015

This work is dedicated to my beloved parents,
for the pride and hope they always hold on their son,
for the love and life they devote to their son.

2015

Acknowledgements

First of all, I'd like to express my sincere gratitude to my major advisor Prof. Yu Lei for his guidance throughout my graduate study. This work is impossible without his encouragement and support. During the recent four years, he has offered me the opportunity to be a Ph.D. student, provided me with comfortable environment for research, given me the freedom to explore, and when necessary, guided me back on the right track. Furthermore, he cared about the students' growth outside scientific areas. I am grateful to him as a great mentor in both scientific and extracurricular aspects.

In addition, I wish to thank my advisory committee for their valuable guidance, support, and feedback during my Ph.D. research. Prof. Christian Brückner helped me on fluorescence knowledge, experimental design, manuscript composition, and he also encouraged me to explore the mechanisms behind the data. Furthermore, his enthusiasm, cautiousness and kindness greatly impressed me. Prof. Mu-Ping Nieh helped me a lot on the polymer background, English improvement, career development, etc. Prof. Steven L. Suib gave me great convenience in using various equipments in his lab, and Prof. Jing Zhao helped me through the "Optical Analysis" class, valuable discussion and lab equipment.

I also appreciate many collaborators such as Prof. Pu-Xian Gao and Dr. Haiyong Gao for high temperature gas sensing, Prof. Hanchen Huang and Dr. Stephen Stagon for surface enhanced Raman scattering based glucose detection, and Prof. Challa Kumar for protein based sensors.

I need to thank staff, Dr. Gary Lavinge, Dr. Lichun Zhang, Dr. Heng Zhang, Dr. Jack Gromek in IMS for materials characterization and Ms. Susan Soucy and Ms. Leah Winterberger in Department of Chemical and Biomolecular Engineering for their help in my Ph.D. studies.

Furthermore, for the excellent group, efficient cooperation and harmonious atmosphere, I acknowledge my labmates such as Ying Wang, Liang Su, Yixin Liu, Xiaoyu Ma, Jun Chen, George Shaw, Andrew Carrier, Jorge Paz Soldan, Qiuchen Dong, Sichen Zhang, Jing Bao, etc. I would also like to thank Yongtao Meng and Junkai He in Prof. Suib's lab, Swayandipta Dey in Prof. Zhao's lab for their help and suggestions in my research. Kan Fu and Wenxiao Huang are greatly appreciated for the amazing experience in BASF Science Competition. I also thank my roommates and all good friends for their support in the past four years, in which I had a wonderful, colorful and unforgettable life.

Most of all, I would like to express my never ending love to my parents and my family for their unconditional support and care.

Table of Contents

Chapter 1

Introduction

1.1 The Background of Explosives Detection

An explosive, which contains a great amount of potential energy, is a reactive material that can be initiated to undergo very rapid and self-propagating decomposition leading to the formation of more stable material, production of light, heat, sound and pressure.[1,2] Based on the chemical structures, the explosive has been classified into six broad classes as shown in Table 1.1.[3-5] Typically, nitroaromatics (NACs), such as 2,4,6-trinitrotoluene (TNT) and 2,4-dinitrotoluene (2,4-DNT), are the primary military explosives and also the principal components in the unexploded landmines worldwide. Nitramines and nitrate esters (e.g., 3,5-trinitroperhydro-1,3,5-triazine (RDX) and pentaerythritol tetranitrate (PETN)), are main components of highly energetic plastic explosives, such as C-4 (91% RDX) and Semtex (40-76% PETN). Ammonium salts (such as AN and AP) are commonly used in the industrial applications, typically in mining and solid rocket propellants. Peroxide-based explosives like TATP and HMTD are easily synthesized from commercially available and inexpensive materials, thus they have grown rapidly and widely in improvised explosive devices. Most high explosives are nitro-substituted (nitrated) compounds, and have the priority to be detected.

The reliable and accurate detection of explosives has received much attention due to homeland security, military issues and environmental pollution during the past few years.[6-8] The recent rise in global terrorism has stimulated the necessity of standoff/remote, sensitive and low-cost detection of explosives. In addition, given the widespread use of explosive formulations, the

analysis of explosives has been of importance in forensic research, landmine detection, and environmental problems associated with explosive residues. Health risks associated with the release of explosives into the environment from military sites and previous ammunition plants is one increasing concern, since explosive presents harmful effects to all life forms. An example of this is the fact that overexposure to TNT can cause anemia due to the compound's property of being able to penetrate the skin and enter into the bloodstream directly, liver problems and even cataracts and it is suspected to be a pollutant at concentrations above 2 ppb. Therefore, rapid, sensitive and selective explosive detection could provide rapid warning in case of terrorism attacks, help in tracking and locating explosive materials as well as reducing the continued fatalities of civilians from landmines, and offer appropriate feed-back during the characterization and remediation of contaminated sites.

However, the detection of explosive compounds is a highly difficult task.[3] Nitrated explosives are extremely sensitive to mechanical shock, friction and heat, therefore, detection methods that permit contact-free analysis are desirable. Moreover, the demands of detecting hidden explosives in transportation hubs and buried explosives in warzones also have led to an intense interest in ultrasensitive detection of nitrated explosives in vapor phase. Since the explosives have extremely low vapor pressures (e.g., TNT, RDX, Tetryl and PETN) as shown in Table 1.1, their detection can be more challenging. In addition, explosives are usually concealed and packed in the plastic materials, which can further reduce the effective vapor pressure by a factor of 1000. Furthermore, because physical properties of each class of nitro-explosives vary significantly from others, no single sensor is capable of measuring the entire range of common explosives using a single material. Finally, daily chemical interferences such as musk fragrance are likely to be interferences and may lead to false alarms.

Table 1.1 Six principal chemical categories explosives, examples and vapor pressure data[5]

Class	Name	Acronym	Structure	$P_{vap,}$ 25°C /Torr
Nitroalkane	2,3-Dimethyl-2,3-dinitrobutane	DMNB		1.88×10^{-3}
	Nitromethane	NM	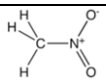	36.5
Nitroaromatic	2-Nitrotoluene; 3-Nitrotoluene; 4-Nitrotoluene	NT		4.89×10^{-2}
	2,4-Dinitrotoluene; 2,6-Dinitrotoluene	DNT	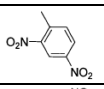	2.63×10^{-4}
	2,4,6-Trinitrotoluene	TNT	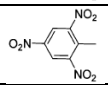	5.50×10^{-6}
	2,4,6-Trinitrophenol (Picric acid)	TNP, PA	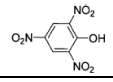	5.8×10^{-9}
	Nitrobenzene; *o*-, *m*-, *p*-dinitrobenzene; 1,3,5-trinitrobenzene	p-DNB	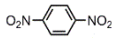	9.00×10^{-4}
Nitramines	1,3,5-Trinitro-1,3,5-triazacyclohexane	RDX	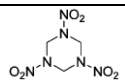	3.30×10^{-9}
	Octahydro-1,3,5,7-tetranitro-1,3,5,7-tetrazocine	HMX	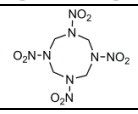	3.01×10^{-15}
	2,4,6-Trinitrophenylmethylnitramine	Tetryl	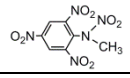	6.51×10^{-9}
Nitrate ester	Nitroglycerin	NG	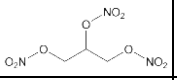	4.81×10^{-4}
	Pentaerythritol tetranitrate	PETN	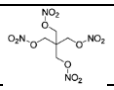	1.16×10^{-8}
Acid salts	Ammonium nitrate	AN	NH_4NO_3	9.77×10^{-6}
	Ammonium phosphate	AP	$(NH_4)_3PO_4$	2.97×10^{-11}
Peroxides	Hydrogen peroxide	HP	H_2O_2	[a] 2.05×10^{-1}
	Triacetone triperoxide	TATP		4.65×10^{-2}
	Hexamethylene triperoxide diamine	HMTD		[b]

[a] the HP vapor pressure is that for 32% HP; [b] No vapor pressure data for HMTD was reported, instead decomposition products.

In other occasions, the sensing applications are required to be performed in aqueous matrix.[9,10] Sensing of explosives in groundwater is of paramount importance due to the extension of terrorism activities from land to marine environments, location of underwater mine and characterization of soil and groundwater contaminations. Although the solubility in aqueous phase is not as low as their ultralow volatility, saturated concentrations are hardly achieved. This makes the explosive detection in aqueous samples by 'tasting' them out very challenging.

Nearly every analytical tool has been investigated for its ability to solve this highly significant task such as trained canine teams, metal detectors, ion mobility spectroscopy (IMS), X-ray-imaging, gas chromatography coupled with mass spectroscopy, thermal neutron analysis, electrochemical procedures, surface plasmon resonances, etc.[7,11] While all the above-mentioned methods offer advantages, none is ideal due to certain disadvantages such as poor sensitivity and selectivity, lack of portability, susceptibility to false positive or negative readings. Trained dogs remain the golden standard and are reliable for the detection of explosives due to their powerful olfactory system. Well-trained canines have been widely used in the field test and the transportation sites to identify and discriminate between target molecules. However, dogs require extensive and costly training, qualified handlers, and only work for limited periods of time in certain geographical areas. Metal detectors are indirect techniques and very efficient for landmine and weapons detection packaged in metals, however, this technique is not sensitive for explosives' chemical finger-print property thus cannot be applied for transportation sites screening. IMS is one used explosive detection system in airports, and has sensitivity down to nanogram even pictogram for common explosives, but this technique lacks enough sensitivity for explosives, such as PETN and RDX, which limits its overall utility. In addition, this method endures disadvantages such as the need for sophisticated protocols with time-consuming

calibration, poor portability and high cost, making it not suitable for broader use. Other laboratory explosive detection systems also endure similar limitations. There thus remains an urgent need for innovative detection strategies that are not only low-cost and user-friendly, but also highly sensitive and selective.

One particularly attractive and promising approach would involve the use of optical methods, which offer many benefits over other common detection techniques, such as low-cost, good portability, high sensitivity and selectivity. Consequently absorbance (colorimetric) and fluorescence responses are the main focus of vast recently developed optical sensors developed for explosive detection.[1] Typically, fluorescence-based detection especially fluorescence quenching is one to three orders of magnitude more sensitive and has wider linear ranges compared to absorbance-based methods. Moreover, the source and detector of fluorescence quenching could be easily incorporated into a handheld device for field detection of explosives. Thus, fluorescence-based method has the great promise to be applied in the rapid, sensitive and selective detection of explosives, and thus becomes the focus in this thesis.

1.2 Methods and Mechanisms for Fluorescence Based Explosives Detection

Due to the non-fluorescent properties of explosives, the fluorescence based explosive detection is an indirect method to utilize fluorophore species (fluorescent sensory materials) that undergo fluorescence changes upon interactions with explosives. Theoretically, any phenomenon that results in a change of fluorescence intensity (quenching or enhancement), wavelength, anisotropy, or lifetime related to the concentration and exposure time of explosives has the potential to be used to sense explosives.

1.2.1 Interactions Caused Fluorescence Detection

During all the published fluorescence based explosives sensors, fluorescence quenching methods still dominate. There are several mechanisms responsible for fluorescence quenching such as photo-induced electron transfer, resonance energy transfer, electron exchange, etc.[12]

1.2.1.1 Photo-induced electron transfer (PET)

Many explosives are highly nitrated organic compounds. This property renders them electro-deficient, which could bind to electron-rich fluorophore through donor-acceptor (D-A) interactions.[13] In the photo-induced electron transfer, the excited-state of fluorophore (D) is likely to donate an electron to the ground-state of explosive compounds (A) as shown in Figure 1.1A.[12] In PET, a complex is formed between the electron donor and the electron acceptor. This charge transfer complex can return to the ground state without emission of a photon, but in some cases exciplex emission is observed. Finally, the extra electron on the acceptor is returned to the electron donor. The energy gap between the LUMO of donor fluorophore and that of the acceptor explosive is approximately the thermodynamic driving force for this oxidative electron transfer process. PET plays a major role in the fluorescence quenching process, and provides useful insights into the development of explosive fluorescence sensors.

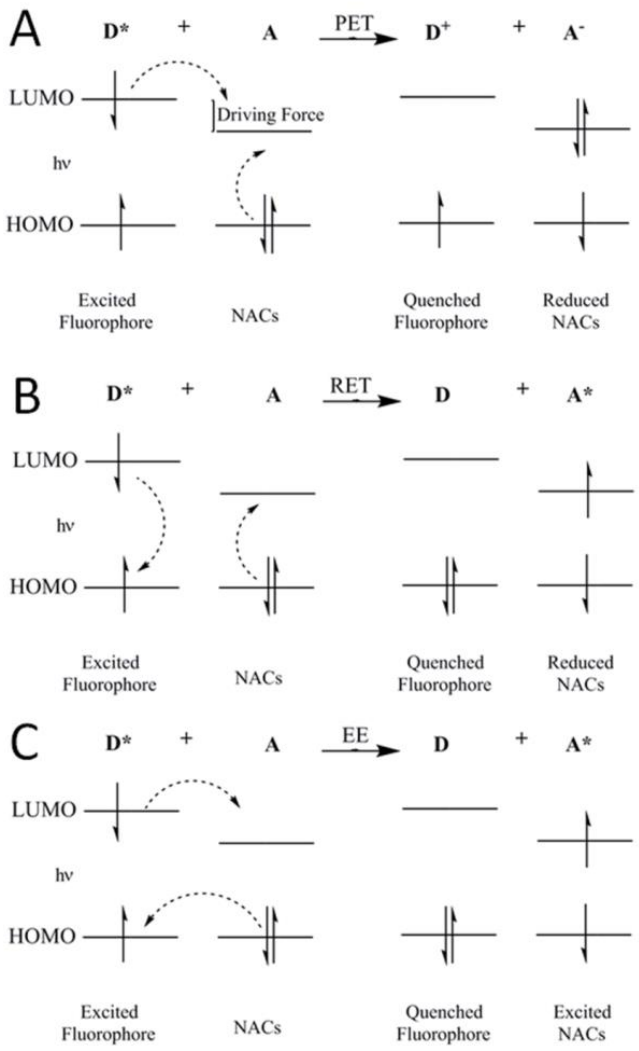

Figure 1.1 Molecular orbital schematic illustration for different interactions. (A) photoinduced electron transfer (PET), (B) resonance energy transfer (RET), and (C) Energy exchange (EE).

Obviously, the quenching efficiency is directly proportional to the electron transfer. For conjugated polymers, electron transfer is based on π-π stacking in a D-A system. The semiclassical limit of Marcus theory has been developed to analyze the PET process, the electron transfer rate (K_{et}) is expressed as[14,15]

$$K_{et} = A\exp\left(-\frac{\Delta G^{*}}{kT}\right) = \frac{2\pi^{\frac{3}{2}}}{h\sqrt{\lambda kT}}V^{2}\exp\left[-\frac{(\Delta G^{0}+\lambda)^{2}}{4\lambda kT}\right] \quad (1.1)$$

where h, k, T, are the physics parameters such as Planck constant, Boltzmann constant, and temperature in Kelvin. ΔG^0 means the standard Gibbs free energy difference of the electron transfer reaction, V is the electron coupling between the initial state (D*A) and final state (D^+A^-), and λ is the reorganization energy which is a relax energy of adjusting molecular structure for producing new stabilized state and includes two contributions: (i) the internal part λ_e related to the geometry changes of the D and the A and (ii) the external part λ_e related to the changes of the surroundings. Under the one-electron approximation, the ΔG^0 can be obtained by the energy gap between the LUMO of the A and that of the D, which can be readily calculated by using a quantum-chemical calculation method. Electron coupling (V) can be considered as direct LUMOs coupling between the D and the A, which is strongly dependent upon the distance between them and also on the relative orientation of them. Simply, ΔG^0 is considered as the thermodynamic driving force for the PET process.

Photo-induced electron transfer contributed to the fluorescence quenching by nitro-explosives, which accounted for the most of the fluorescence-based explosives detection. PET mechanism also led to fluorescence enhancement and was used for explosives detection in recent years. It was believed that sensing by enhancement of fluorescence was superior to quenching due to several reasons.[16] Firstly, the appearance of a bright signal on a completely dark ground was qualitatively easier to detect than the dimming of an already bright signal and was little affected by the fluorescence background thus leading to higher sensitivity. Second, turn-on signals were resulted from a stoichiometric binding event, rather than from a collisional encounter. For example, through introducing appropriate substituents onto the boron-dipyrromethene (BODIPY) framework, a specific

fluorescence turn-on chemodosimeter for picric acid was achieved.[16] Without the addition of picric acid, the BODIPY was weakly fluorescent, due to the PET that occurred from the acetal oxygen to the BODIPY. The addition of picric acid broke the PET process because of the interaction of the picric acid and acetal oxygen of the BODIPY core and formation of corresponding aldehyde.

In PET the excited fluorophore can be either electron donor or acceptor.[12] The direction of electron transfer is determined by the oxidation and reduction potentials and molecular orbitals of the ground and excited states. This unique theory has been utilized for differentiation between electron-deficient explosives and electron rich compounds, leading to fluorescence-off and fluorescence-on phenomena, respectively.[17,18] Since the LUMO levels of electron rich arenes were higher than that of fluorophore, electron transferred from electron rich compound to fluorophore, and resulting in fluorescence enhancement (Figure 1.2). Due to the exciplex formation between arenes and fluorophores, emission spectra shift could also be observed. Therefore, combining the fluorescence intensity changes with spectra shift, the 2D map provided a new route to sensitive and selective detection of explosives and explosive-similar compounds.[19]

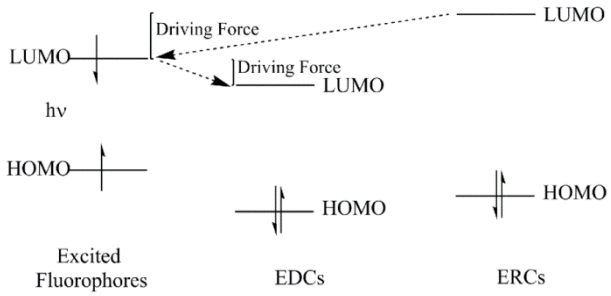

Figure 1.2 Schematic drawings of the electronic structure of the fluorescence quenching process by electron deficient compounds (EDCs) and the fluorescence enhancement process by electron rich compounds (ERCs).

1.2.1.2 Resonance energy transfer (RET)

Energy transfer mechanism has also been used to develop a number of explosive sensors, and can dramatically enhance the fluorescence-quenching efficiency and improve sensitivity. In Förster resonance energy transfer (FRET), an initially excited molecule (donor) returns to the ground state orbital, while simultaneously the transferred energy provides an electron on the acceptor to the excited state as depicted in Figure 1.1B.[12]

RET is due to long-range dipolar interactions through D* and A. RET is not sensitive to steric factors or electrostatic interactions. According to FRET theory[6,20], the rate of energy transfer depends on 1) the relative orientation of the donor and acceptor dipoles, 2) the extent of overlap of fluorescence emission spectrum of the donor (the fluorophore) and absorption spectrum of the acceptor (the analyte), and 3) the distance between the donor and the acceptor. The probability of resonance energy transfer depends upon the extent of overlap between these molecules. The efficiency (E) of energy transfer between the donor and the acceptor could be calculated by the following equation[12]:

$$E = 1 - \frac{F}{F_0} = \frac{R_0^6}{R_0^6 + r_0^6} \tag{1.2}$$

where, F and F_0 are the relative fluorescence intensities of the donor in the presence and absence of acceptor, respectively; r_0 represents the distance between the donor and the acceptor, and R_0 is the critical distance at which energy transfer efficiency equals to 50%. The value of R_0 is calculated using the equation:

$$R_0^6 = 8.79 \times 10^{-5} K^2 n^{-4} \emptyset J \tag{1.3}$$

Where K^2 is the orientation factor related to the geometry of the donor-acceptor dipole, n is the refractive index of the medium, ∅ is the fluorescence quantum yield of the donor,

and J expresses the degree of spectral overlap between the donor emission and the acceptor absorption, J is given by:

$$J = \frac{\int_0^\infty F(\lambda)\varepsilon(\lambda)\lambda^4 d\lambda}{\int_0^\infty F(\lambda)d\lambda} \quad (1.4)$$

where $F(\lambda)$ is the corrected fluorescence intensity of the donor in the wavelength λ to $\lambda+\Delta\lambda$, and $\varepsilon(\lambda)$ is the extinction coefficient of the acceptor at λ.

In recent years, FRET mechanism has been widely utilized for explosive detection to improve the sensitivity and selectivity by various research groups. Almost all the work applied this mechanism through fluorescence quenching phenomena to detect explosives, which could fall into two broad categories. One was the direct utilization of the unique spectrum of explosives. Through rationally designed fluorophore materials, the emission spectrum of the fluorophore efficiently overlapped with absorption of explosives.[21] For example, picric acid had a different absorption spectrum from other nitro explosives. Harnessing this difference, researchers developed highly sensitive and selective fluorescence sensors to detect picric acid.[21,22] The second method utilized electron deficient properties of nitro-explosives and formation of Meisenheimer complex, the absorption of which overlapped with the emission of fluorescent materials.[23,24] For example, electron-rich primary amines have been exploited as promising binding sites to TNT, through a donor-acceptor interaction to form Meisenheimer complexes.[25] Through this mechanism, the nitro-based electron-deficient explosives could be detected sensitively and selectively.

Besides the dominant use of explosive-induced fluorescence-quenching phenomena resulted from FRET mechanism, fluorescence-enhancement has also been reported for the

detection of explosives.[26] Xia and co-workers found that addition of TNT molecules broke the pre-formed assembly between quantum dots (QDs) and gold nanorod (AuNR) and switched off the FRET from QDs to AuNR and then the fluorescence enhancement was achieved. This explosive sensor possessed a LOD of 0.1 nM which was one of the best results among fluorescent based explosive sensors. Such ultra-high sensitivity is attributed to the combination of a number of features including fluorescence turn-on effect, FRET switching-off and the unique design of fluorophore material.

1.2.1.3 Electron exchange or Dexter interactions

Electron exchange (Dexter interactions) occurs between a donor and an acceptor, where the excited donor has an electron in LUMO (Figure 1.1C).[12,27] This electron is transferred to the acceptor, and the acceptor then transfers to an electron back to the donor. The electron comes from the HOMO of the acceptor, so the acceptor is left in an excited state. Dexter interaction is a short-range phenomenon that falls off exponentially with distance and depends on spatial overlap of donor and quencher molecular orbitals. RET association occurs over long distances, so if there is spectral overlap, the transfer occurs by RET is more important than the Dexter mechanism. Electron exchange can be observed and predominant over RET if the spectra overlap is small. Additionally, high concentrations are necessary for significant electron exchange, whereas RET occurs at much lower concentrations. With both RET and electron exchange processes, the shapes of the absorption and fluorescence spectra of the dyes are unchanged. Furthermore, the electron exchange process is a quantum mechanical effect that does not have an analogy in classical electrodynamics. Swager and co-workers reported on the selective detection of cyclic ketones via energy transfer, that was dominated by an electron-exchange

mechanism to an upper excited state of the fluorophore followed by relaxation and emission to account for the efficient energy transfer in the absence of appreciable spectral overlap.[27] They proposed that the exquisite selectivity was due to a subtle balance of receptor specificity and the ability of analytes into the polymer matrix.

1.2.2 Fluorescence Quenching Theory

Fluorescence quenching requires molecular contact between the fluorophore and quencher. This contact is resulted from diffusive encounters, which is dynamic quenching, or resulted from complex formation, which is static quenching.[12]

The aforementioned two quenching processes have very different natures, which could be distinguished by time-resolved measurements of the fluorescence decays of the sensing materials. For static quenching, the fluorescence decay lifetime of a material will remain unchanged as the concentration of quencher is increased. Formation of a non-fluorescent fluorophore-quencher complex is the origin of the quenching, and any molecule not bound to an analyte decays with their native natural lifetime. For dynamic quenching (collisional quenching), collision of the quencher molecules to the excited fluorophores is a necessity, and thereby dynamic quenching is a diffusion-controlled process. The fluorophore and quencher are unbound and quenching occurs when a photoexcited material interacts briefly with a colliding analyte molecule. Thus it leads to a decrease in the average fluorescence lifetime. The measurement of fluorescence lifetime change in the absence and presence of explosive quenchers represents the most prevalent way to examine whether the quenching is a static or dynamic process. Generally, the ratios of lifetime τ_0/τ are plotted versus the quencher concentration. For static quenching, $\tau_0/\tau=1$; in contrast, fluorescence intensity $F_0/F=\tau_0/\tau$ for dynamic quenching.

Collisional quenching of fluorescence is described by the Stern-Volmer equation and the correlation of lifetime with quencher concentration can be expressed as:

$$\frac{F_0}{F} = 1 + k_q \tau_0 [Q] = 1 + K_D [Q] \quad (1.5)$$

$$\frac{F_0}{F} = \frac{\tau_0}{\tau} \quad (1.6)$$

where, F_0 and F are the fluorescence intensities in the absence and presence of quencher, respectively; τ_0 and τ are the lifetimes of the fluorophore in the absence and presence of quencher, respectively; k_q and K_D are the bimolecular quenching constant and Stern-Volmer quenching constant, respectively, and [Q] is the quencher concentration.

For static quenching, the dependence of the fluorescence intensity upon quencher concentration is easily derived by consideration of the association constant for complex formation, and the equation is shown as follows:

$$\frac{F_0}{F} = 1 + K_S [Q] = 1 + K_D [Q] \quad (1.7)$$

in which, K_S is the Stern-Volmer constant for static quenching process.

For combined dynamic and static quenching process, the change in fluorescence is expected to be given by

$$\frac{F_0}{F} = (1 + K_D [Q])(1 + K_S [Q]) = 1 + (K_D + K_S)[Q] + K_D K_S [Q]^2 \quad (1.8)$$

When the analyte concentration is very low, the contribution of the $[Q]^2$ is less prominent and Equation (1.8) would yield to a linear plot. However, at higher concentrations, the plot deviates from linearity and bends upwardly. This equation greatly explains an upward bending curvature at high quencher concentrations or an exponential fitting of the Stern-Volmer plot in some circumstances.

While both pathways can be operative, static quenching prevails in explosives detection due to its larger K_{SV} for explosives binding to many polymeric indicators and a higher sensitivity in general. Although the fluorescent sensors of dynamic quenching have the potential to lead faster and more reversible detection, they possess much smaller K_{SV} and demonstrate a lower sensitivity.[28]

Static and dynamic quenching can also be differentiated by their differing dependence on temperature and viscosity.[12] Higher temperatures result in faster diffusion and hence larger amounts of collisional quenching. While for static quenching, higher temperatures will typically promote the dissociation of weakly bound complexes, and hence lead to lower amounts of non-fluorescent fluorophore-quencher complexes. One additional method to distinguish static and dynamic quenching is by careful examination of the absorption spectra of the fluorophore. Collisional quenching only affects the excited states of the fluorophores, and thus no changes in the absorption spectra are expected. In contrast, ground-state complex formation will frequently lead to perturbation of the absorption spectrum of the fluorophore. Furthermore, the bimodular quenching constant k_q is calculated using the ratio of Stern-Volmer quenching constant (K_{SV}) to unquenched fluorescence lifetime (τ_0), which is also used to distinguish between static and dynamic quenching. For dynamic quenching, diffusion-controlled quenching typically results in values of k_q near 10^{10} M^{-1} sec^{-1}; while for static quenching, the k_q value is generally several orders larger than 10^{10} M^{-1} sec^{-1}.

1.3 Sensory Materials for Fluorescence Based Explosives Detection

Various fluorescent materials have been developed and shown high efficiency to explosives detection such as conjugated polymers, small molecule fluorophores, supramolecular systems,

bio-inspired materials and aggregation induced emission – active materials, etc. Due to the volume of this dissertation, only a brief introduction of these materials is shown.

1.3.1 Fluorescent Conjugated Polymers

Fluorescent conjugated polymers (CPs) have recently been used successfully in nitrated explosives detection.[29-31] Compared with small molecule fluorophores, they have extended exciton migration pathway and efficient electronic communication between quenchers along the polymer backbone. CPs are excellent electron donors, and their donor ability is enhanced by the delocalized π^* excited state, which facilitates exciton migration and hence increases the electrostatic interaction between the polymer and electron-deficient nitroaromatic analytes. For CP fluorescent sensors, Swager et al. proposed that binding one receptor site resulted in an efficient quenching of all emitting units in an entire conjugated polymeric molecule relative to single molecule systems. This amplification is known as the "molecular wire" effect, or "one point contact, multi-point response" effect. In general, fluorescent polymers can be divided into organic and inorganic categories considering their basic backbone structures.

Swager's group developed a series of poly(p-phenyl-eneethynylene)s (PPEs) that introduced rigid iptycene moieties into a conjugated polymer backbone.[30,32] Their work represents the pioneering study in conjugated polymers for fluorescence explosive sensing. These designs synthesized the materials that demonstrated high fluorescence quantum yields and stability in thin films by preventing quenching interactions. The structures also made free volume in the films that favored diffusion of small molecules into the film. Thin films of pentiptycene-derived PPE were highly emissive but underwent a dramatic reduction in emission intensity when exposed to NAC molecules. The fluorescence intensity quenched about 50% and 70% upon

exposure to TNT vapor for 30 s and 60 s respectively. In addition to PPEs, numerous classes of conjugated polymers have been investigated for explosives sensing, such as poly(p-phenelene)vinylenes, polyfluorenes, polycarbazoles, polyacetylenes, polythiophenes, etc.[6,8,31]

Polymers incorporating silicon-based units (inorganic polymers) have been well developed for explosive sensing by Trogler's group. For example, they synthesized three different polymers.[4] The band gap of polymers could be enlarged through incorporating silafluorene units in the polymer backbone, which allowed for detection of a broader range of explosives, while the other polymers was quenched only by NACs or by both RDX and NACs due to their various structures. In addition, Tang's group discovered a new system of aggregation induced emission (AIE) effect.[33] In the system, the luminogen aggregation played a constructive role in light-emitting process: a series of silole molecules such as tetraphenylethene (TPE) and triphenylbenzene (TPB) were virtually nonfluorescent when dissolved in their good solvents, but emitted intensely when aggregated in their poor solvents or fabricated into thin films and worked as picric acid sensors.[34] The AIE effect endowed the silole polymer the ability to explosive detection highly sensitively.

1.3.2 Small Molecule Fluorophores

Small molecule fluorophores are the main focus in the early development of fluorescence-based explosive sensors because of their simple synthesis, varied pathways of fluorescence quenching and ability to detect a wide range of explosives.[7] The main difference between polymeric systems above and small molecule-based detection lies in the mechanism of fluorophore quenching and the absence of exciton migration in the small molecules. Polymer-based sensors frequently detect explosives through static quenching; in contrast, well-resolved small molecules typically work through collisional

quenching. Besides simple small molecules, functional small molecule fluorophores have been appearing and attracting great attention in recent years, and presumably show greater potential in explosive sensing by the form of oligofluorophores[35,36], self-assembling small fluorophores[37] or doping of these molecules into a matrix[38], because they can enhance binding and/or introduce exciton migration.

Polycyclic aromatic hydrocarbons (PAHs) are structurally similar organic molecules characterized by the presence of fused aromatic rings such as pyrene, anthrancene, perylene, naphthalene, etc. Most PAHs have high fluorescence quantum yields with remarkable electron donor nature, which allows the formation of non-fluorescent charge transfer complexes with electron deficient molecules. Considering they also facilitate π-π interactions with aromatic compounds, PAHs constitute an important class of small fluorophores for nitrated explosives. Among PAHs, pyrene and its derivatives were widely explored.[7]

Porous silicon as inorganic small molecules could exhibit a visible photoluminescence compared with bulk Si. Work from Sailor and Trogler demonstrated several optical sensing transduction modes from porous silicon for NAC vapors by the electron-transfer mechanism.[39] Upon exposure to the explosive vapors, the photoluminescence of porous Si film was quenched, and the detection limits were 500, 2 and 1 ppb for NB, DNT and TNT, respectively. Siloles and Si nanocrystals have been investigated for the detection of explosives as well. Quantum dots[40], quantum clusters[41] and carbon dots[42] were some of the newly developed materials and provided great potentials in explosives detection.

In order to control the film thickness, to prevent leaking of fluorophores and to decrease the diffusion issues, self-assembled small fluorophore molecules for explosive detection has been

extensively investigated by Fang's group.[43-45] They found that length and structures of the spacer connecting the sensing element and the substrate played an important role in mediating the sensing performance of such film sensors in detecting analytes.

Recently, our group reported small fluorophore such as pyrene doped in polymer as explosive sensing materials.[38] The high binding affinity between the electron-deficient nitro explosives and the sensing films resulted in a rapid dramatic quenching in the fluorescence emission. A wide spectra of nitro-explosives could be visually detected at their sub-equilibrium vapour concentrations. The potential π-π stacking between pyrene and/or phenyl pendants of polystyrene in the highly porous structure and large surface areas of nanofibers were possibly responsible for the excellent sensing performance. Furthermore, the polymer matrix possibly stabilized the pyrene and prevented the leaking of pyrene into the aqueous solution. Similar research was also reported by Bayindir and co-workers, they observed fast and sensitive detection of explosives through pyrene doped polyethersulfone thin films.[46]

1.3.3 Supramolecular Systems

Supramolecular systems have been developed and popularly utilized in explosives detection, and they consist of a broad range of materials such as macrocycles[47-49], dendrimers[50], supramolecular polymers[51] and metal organic frameworks (MOFs)[52]. Regarding to the number of published work, supramolecular systems (especially MOFs) are possibly the most popular and fastest growing fluorescent materials for explosives detection in recent years.

MOFs are constructed via self-assembly of single metal cations (primary building unit or PBU) or metal clusters (secondary building unit or SBU) with organic ligands having multiple binding sites, thus forming one, two, or three dimensionally extended coordination networks. The pioneering work of Li et al. demonstrated the potential of luminescent MOFs in explosives

detection with a quenching efficiency of 84% upon 10s exposure to DMNB vapour.[53] The same group later demonstrated the unique selectivity of nitro explosives and other arenes through fluorescence quenching, enhancement and spectra shift.[17] For the development of MOF materials in explosives detection, there are several powerful approaches in general. One is to enhance the electron density of the MOFs and to facilitate the exciton migration through using conjugated ligands or backbones with metal ions which possess a non-detrimental nature of fluorescence, or using fluorescence tag in the backbone of the ligands which possess benzene, naphthalene, pyrene, etc.[54] Secondly, the introduction of secondary functional groups which endows preferred binding of the chosen analyte resulting in better selectivity to the specific analytes.[55] Furthermore, decreasing MOF size particles favors the increase of surface area and porosity and promotes the diffusion of analytes into the MOFs.

1.3.4 Bio-inspired Fluorescent Materials

Recently, biomaterials such as peptide, protein and DNA have been introduced into fluorophores for explosive detection. The biomaterials can act as the support or functional layer for the fluorophores. Bovine serum albumin (BSA) functionalized and protected quantum crystals were capable of selective and sensitive detection of TNT, which can be explained through the formation of a Meisenheimer complex by the chemical interaction between TNT and the free amino groups in BSA.[41] In addition, the fluorescence properties of biomaterials such as fluorescent proteins were exploited. In Hick's study, the fluorescent properties of proteins were applied for explosive quenching taking advantage of the fact that tryptophan excitation can be quenched by numerous agents.[56] The work provides great potentials for production of genetically-modified fluorescent

protein sensor arrays for rapid, simultaneous, sensitive and selective detection of a broad range of explosive agents.

1.4 Nanomaterials for Fluorescence Based Explosives Detection

The utilization of nanomaterials with unique fluorescent properties has opened up new horizons for trace explosives detection.[57] A lot of fluorescent materials were synthesized at nano-scale such as quantum dots, quantum clusters, carbon dots, metal-organic frameworks, etc. These fluorescent nanomaterials can work as excellent sensors for explosives detection not only because of their electronic structures, but also large surface areas. Generally, sensory material with smaller size and higher porosity favors the diffusion of analytes and reduces the response time. Take MOF as an example, MOF nanotube[58], MOF nanofiber[59], surfactant-assisted nanorods[60], magnetic nanospheres[61], and microwave-assisted nanoparticles[62] were reported in order to improve the sensitivity and response time. Parkin's recent work reiterated the key importance of MOF porosity in sensing applications and highlighted the value of uniform microcrystals to sensitivity for explosives detection.[63] They proposed that the flatter and more uniform crystals gave greater access to the material on the sensing substrate and improved response. In addition, Qiu et al. used a self-sacrificing template to synthesize MOF nanotubes.[58] The resultant fluorescent MOF nanotubes showed fast, highly sensitive, selective, and reversible detection for trace-level of nitroaromatic explosives, indicating that the tubular MOF nanostructures were great materials for the detection of explosives.

Considering that materials with large surface area favor for sensing applications, non-fluorescent nanomaterials could function as supports to improve the sensing performance. Fluorophores functionalized on nanoparticles (NPs) and nanofibers have been investigated. For example, the high surface-to-volume ratio of nanoparticles has been

used to obtain a high local concentration of pyrene units on their periphery, making the formation of both pyrene emissive species possible by using amazingly low pyrene concentrations.[64] The encapsulation capacity of the NPs may result in an increased sensitivity to the analyte. Substituted pyrene compounds were coated on the conjugated polymer nanofibers, too.[65] 14-fold of sensitivity enhancement in detection of H_2O_2 was achieved due to high area-to-volume ratio, excellent gas permeability, and more importantly, the evanescent-wave effect. Due to the slow photon effect of photonic crystal and large surface areas of the inverse opal structure, optimized photonic crystal method was used to prepare fluorescent sensory materials through the conjugated polymer.[66] TNT sensors were prepared by spin-coating 5-chloroform solutions with different concentrations onto inverse opal SiO_2 photonic crystal films and glass substrates. The fluorescence enhancement (up to 60.6-fold) for TNT detection was achieved when compared to the control sample. Such amplification of fluorescent signal provides a facile method for improving sensitivity and resolution of explosives detection.

Nanomaterials can be prepared by various methods, which generally fall into two broad categories: top-down and bottom-up ones.[67] In top-down method, the nanoparticles are formed by breaking down large pieces of materials into small desired nanostructures through arc discharge, laser ablation, chemical and electrochemical oxidation etc. In bottom-up approach, the nanomaterials are obtained from assembling molecular precursors through different reaction conditions including solvent-thermal condition, supported synthetic, or microwave methods.

1.5 Motivation, Objectives and Organization

Nitro-explosives detection plays an important role in anti-terrorism efforts and environmental pollution controls. Fluorescence-based sensing technology represents one

of the most promising approaches for trace explosives detection due to the combination of a number of advantages: short response time, excellent sensitivity, and instrumental simplicity. However, several issues still exist in current fluorescent materials for explosives detection. Firstly, the popular conjugated polymers are often hampered by their time-consuming, low-yield and multi-step synthesis.[7,51,68] In addition, leaking of fluorophores in solution sensing and self-quenching of CPs are two unavoidable problems. Furthermore, the hydrophobic nature and limited water stability of the current fluorescent materials in aqueous solution detection is another impediment that limits the real application.[10,21,45] Some other fluorescent materials are toxic to the environment and their leaking has increased much concerns. For example, the associated toxicity and safety hazards of pyrene and related compounds discourage their routine use, therefore, pyrene-based explosive detection systems require good fixation/immobilization of pyrene, thus preventing its leakage; heavy metals such as Cadmium which have been widely used in quantum dots and metal-organic frameworks are also toxic to the environment.[21,40,69]

Therefore, the major effort of this research focuses on the design and development of novel fluorescent nanomaterials for nitro-explosives detection. The conducted research covers explosives detection in vapour phase, aqueous phase as well as buried explosives.

In this dissertation, there are six research chapters (Chapter 2-7).

Chapter 2: Pyrene-polystyrene fluorescent nanoporous films have been prepared through a simple dip-coating process, and used for explosives vapour detection with ultra-sensitivity and selectivity. Morphology investigations revealed that the fluorescent polymer films consisted of a high-surface, three-dimensional nanoporous array of holes and the possible molecular origins of

fluorescence quenching was investigated through structural XRD studies and the electronic structure of the polymer film.

Chapter 3: Super-hydrophobic, fluorescent sand was prepared using a simple coating method, and used for buried explosives detection. All buried explosives could be successfully observed by the naked eyes using a handheld UV lamp.

Chapter 4: In order to detect nitro-explosives in aqueous phase, Pyrene-polyethersulfone electrospun nanofibers were prepared through electrospinning using mixed solvents. The effect of mixed solvents, polymer/pyrene cocentrations on film morphology and sensing performance were systematically investigated and optimized. The current sensor showed excellent sensitivity, selectivity, and reusability to nitro-explosives detection. Mechanisms for fluorescence quenching by nitro-explosives were also investigated.

Chapter 5: In order to develop low-toxic fluorescent materials, nitrogen-doped carbon nanoparticles (CNPs) have been developed from a single precursor through an ultrafast, facile and microwave-assisted method. The obtained CNPs showed strong blue fluorescence, which could be quenched by picric acid sensitively and selectively.

Chapter 6: The fluorescent carbon dots (CDs) were synthesized using nitrogen and phosphorous co-doped carbon sources through one simple and fast microwave-assisted method. The as-synthesized carbon dots demonstrated dual (blue and green) fluorescence emission under different excitation and high quantum yields. Due to the unique emission properties, the CDs were applied as ratiometric sensors for explosives (PA and TNT) detection.

Chapter 7: A fully biodegradable and environmental-friendly biopolymer (protein) showed sensitive, selective and rapid detection of picric acid, and its excellent sensing performance was

attributed to the synergistic effect of the low molecular orbital, presence of fluorescent resonance energy transfer as well as acid-base interactions.

Finally, Chapter 8 gives a general conclusion of the conducted research and some challenges and future opportunities.

Chapter 2

A Fluorescent Polymer Film with Three-Dimensionally Ordered Nanopores for Explosives Vapor Detection

The quenching efficiency of most fluorescent sensory materials is greatly dependent on the film thickness that controls the diffusion of analyte vapors into the fluorescent film. For instance, Swager and co-workers[30] observed that for a fluorescent conjugated pentiptycene polymer the best fluorescence quenching was obtained with a film thickness of only 2.5 nm; the quenching efficiency was sharply decreased with the increase of the sensory film thickness. However, such thin films are not always readily realized. Moreover, a sufficiently thick fluorescent film is required to produce a reliable signal intensity and to minimize the interference of photo-bleaching effects.[48]

To consolidate these seemingly diametrically opposed requirements, nanoporous materials with high surface-to-volume ratios have been introduced.[38] For instance, our group previously reported the use of polystyrene–pyrene–NBu_4PF_6–based electrospun nanofibers that are capable of detecting a range of nitro-aromatics with ultra-sensitivity. Their excellent sensing performance was attributed not only to an efficient long-range energy migration in the nanofibers, but also to the large surface area to volume ratio of the nanofibrous membrane with high porosity. However, the fluorescence quenching mechanism in the pyrene–polystyrene material by nitroaromatics was not fully understood.[70]

Abstract

The sensitive and rapid detection of nitroaromatic explosives typically requires sophisticated sensory materials. We demonstrate here how a simple dip-coating process of a mixture of polystyrene and the fluorophore pyrene onto a glass slide generates a self-assembled fluorescent nanostructured film expressing regular breath-figure nanopores. Morphology investigations reveal that the fluorescent polymer films consist of a high-surface, three-dimensional nanoporous array of holes, enabling that the fluorescence of this material is rapidly and selectively quenched by nitroaromatic vapors. The morphology of the polymer was controlled by variation of the dip-coating parameters and the ratio of polystyrene to pyrene. This ratio also controls the fluorescence quenching efficiency of the material. We demonstrate the possible molecular origins of this through structural XRD studies as well as investigations of the electronic structure (optical properties, band gap and conduction band determinations) of the polymer film. Our results identify a novel high performance form of an otherwise known explosives sensing material. Most importantly, the findings point toward a general method for the facile realization of well-defined three-dimensional high surface sensory materials with optimized electronic properties.

2.1 Experimental

2.1.1 Materials

Polystyrene (PS, Mw = 350,000), tetrahydrofuran (THF, ≥ 99.0%), tetrabutylammonium hexafluorophosphate (NBu_4PF_6, 98%) and acetonitrile (anhydrous, 99.8%) were purchased from Sigma-Aldrich. Pyrene (Py, 98%) was bought from Acros Organics. 2,4-

dinitrotoluene (DNT, 97%), 1,3-dinitrobenzene (DNB), 4-nitrotoluene (4-NT), 3,5-dinitroaniline (DNA), urea, ammonium nitrate (AN), sodium nitrite (SN), chloranil (CA) were purchased from Sigma-Aldrich or Acros Organics. Perfume (Adidas, pure lightness; the main ingredients include alkanes, alcohols, parfum/fragrance and BHT) was bought from a local market. All the chemicals were used as received.

2.1.2 Preparation of Py-PS Films

Py-doped PS films on glass slides were prepared by dip-coating. Briefly, polymer solutions with different Py concentrations (0.05 M, 0.1 M, and 0.2 M) and PS concentrations (from 0.5-wt % to 6-wt %) were first prepared with THF as the solvent. Next, glass slides (1.25 cm × 2.5 cm) were dipped into the fluorescence polymer solutions for 1 min, and then dried at room temperature in the chemical fume hood to generate fluorescent Py-PS sensing film consisting of 3D ordered nanoporous array of holes.

2.1.3 Fluorescence Quenching Experiments

The fluorescence quenching experiments were conducted in a similar method reported elsewhere.[38,71] In brief, saturated DNT explosive vapors were generated in a sealed methacrylate cuvette containing a small amount of DNT powder, which was covered by a small piece of cotton wool. The glass slide with Py-PS film was then quickly inserted in the cuvette at a 45^{o} angle, such that it was exposed to DNT vapor without making direct contact with the DNT powder. The fluorescence changes of Py-PS films were recorded continuously after the Py-PS films were inserted into the cuvette at time intervals of 30 s. Fluorescence emission spectra were measured in the range of 360-600 nm using a Varian Cary Eclipse fluorescence spectrometer (Agilent Technologies); $\lambda_{excitation}$ = 340 nm. The

quenching efficiency was defined as $(I_0\text{-}I)/I_0$, where (I_0) is the first recorded fluorescent intensity of pyrene excimer peak right after the insertion of Py-PS film into cuvette and (I) is the corresponding fluorescent intensity at different exposure time. The quenching experiments upon the exposure of Py-PS film towards equilibrium vapors of other nitroaromatic compounds (DNB, NT, DNA) and common interferents (Urea, AN, SN, CA, perfume) were also performed in a similar way.

2.1.4 Characterization of Py-PS Films

The morphology of as-prepared fluorescence Py-PS films were obtained using JEOL 6335F Field Emission scanning electron microscope (SEM) at an acceleration voltage of 10 kV, while surface topology images of the sensing films were examined by atomic force microscope (AFM, Asylum Research MFP-3d) in tapping mode with tip radius of 9 nm. Fluorescence microscopy images of Py-PS films were taken on a Nikon A1R confocal laser scanning microscope with attached photomultiplier tube (PMT) camera with an excitation of 405 nm. The thickness of the Py-PS films was measured by a Veeco Dektek 150 surface profiler. The X-ray diffraction (XRD) patterns were obtained on a Bruker D2 Phaser X-ray diffractometer using Cu Kα radiation at a rate of $0.01° \ 2\theta \ s^{-1}$ and operated at 15 kV and 10 mA. The absorption spectra of Py-PS films were performed on a Cary 50 UV-vis spectrophotometer (Agilent Technologies). As the UV-vis spectra of original Py-PS films were out of the detection range of spectrophotometer, all the absorption results were obtained from dip-coated films prepared in a similar way as described above except that 10-fold THF-diluted polymer solutions were used. Fluorescence emission spectra were measured using a Varian Cary Eclipse fluorescence spectrometer (Agilent Technologies). Electrochemical cyclic voltammetry (CV) were

carried out with a CHI 601C electrochemical analyzer at a potential scan rate of 50 mV/s in acetonitrile consisting of 0.1 mol/L NBu_4PF_6. Py-PS thin films dip-coated on the glassy carbon electrode were used as the working electrode, while Pt wire and Ag/AgCl electrode served as the counter and reference electrodes, respectively. Prior to each CV measurement, the solutions were deoxygenated with nitrogen.

2.2 Results and Discussion

2.2.1 Preparation and Morphology of Py-PS Fluorescent Films

In a typical preparation of our pyrene-polystyrene (Py-PS) films, a solution of 0.1 M Py and 4-wt% PS of average Mw 350,000 in THF was dip-coated on a standard microscopy glass slide. During the drying step of the dip-coating process, the relative humidity was controlled to ~60% at an airflow velocity of about 35 m/min. Figure 2.1 shows the morphology of a typical polymer film thus prepared. Closely spaced 3D nanoporous array of holes are observed (Figure 2.1A), with the spacing between pores in the range of hundreds nanometers, providing a high porosity and surface area to the as-prepared film. A confocal fluorescence microscopy image of the film (Figure 2.1B) indicates that the film is fluorescent, with the holes appearing to be darker and less fluorescing. Figure 2.1C shows a 3D-AFM image of the film, revealing a pore size of ~400 nm.

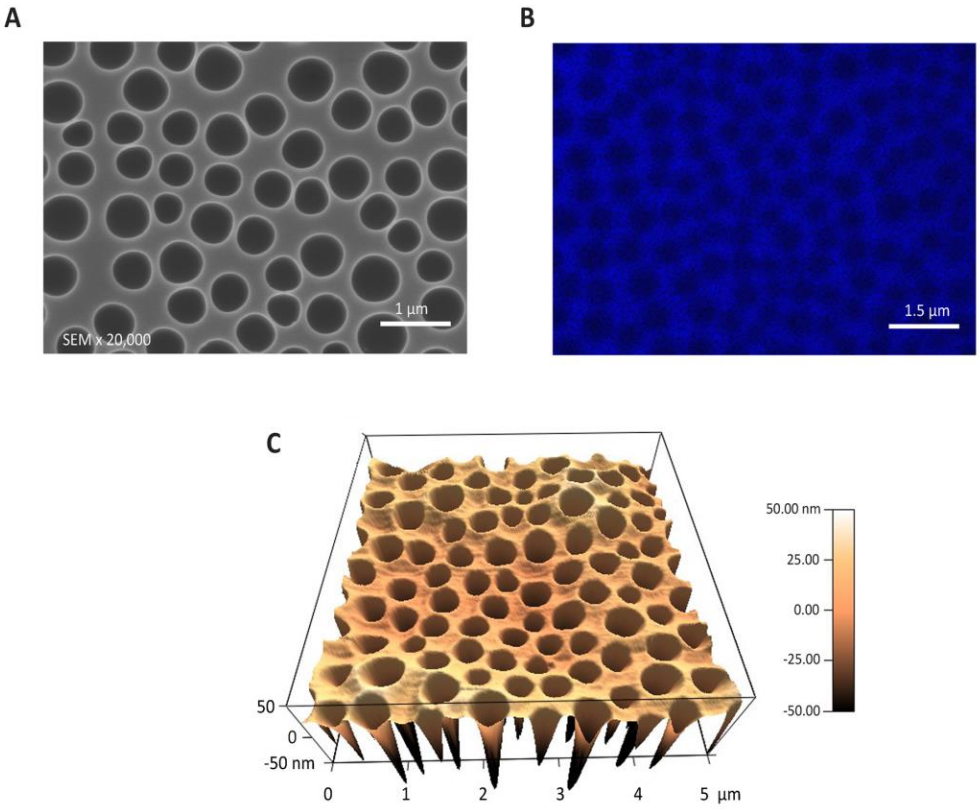

Figure 2.1 Morphology of Py-PS fluorescent film with three-dimensionally ordered nanoporous array. (A) SEM image of nanoporous Py-PS film with an average pore size of 400 nm. (B) Confocal fluorescence microscope image of nanoporous fluorescent film. (C) 3D-AFM image of nanoporous array film collected in tapping mode for 5 × 5 µm section.

This formation of 3D ordered array of nanopores in membranes was achieved applying the "breath figures" principles.[72-75] Breath figures are proposed to form through the condensation of water vapor on the surface of a polymer/organic solvent solution. As the water droplets are uniformly packed in the film by capillary force, it leads to the formation of 3D ordered array of nanoholes in polymer film after the solvent and water evaporates. Generally, the solvents used in preparing this kind of nanoporous film are highly volatile and water-immiscible.[76,77] However, the groups of Kim and Raczkowska[78,79] have recently shown that breath figures can also be obtained using water-miscible solvents such as THF used here. The selection of the appropriate

molecular weight of linear polystyrenes is also an important factor in the formation of regular holes in polymer film, as recently observed by Han et al..[80] Interestingly, when pyrene was added to the polystyrene solution, it might work as an additive that promoted the formation of ordered breath fingers as observed in other reports.[77] A film prepared from a solution of 4-wt% PS and 0.1 M Py shows the well-ordered expression of the breath figures, while in the absence or reduction of the pyrene, the orderliness of nanoporous array in polymer film is poor. The SEM images and pore density of a series of nanoporous fluorescent film are shown as Figure 2.2 and Table 2.1. Furthermore, pore size and dimensions of the nanopores were also greatly dependent on the humidity and velocity of airflow across the surface.[73] It was previously reported that the size and number of pores, spacing between pores and film thickness can be tuned by factors such as polymer concentration, additive, solvent, temperature, humidity, preparation methods, etc. [73,76,81] Therefore, it is expected that through careful control of composition and evaporation conditions, especially the doping of the polymer with various fluorophores, a broad range of 3D ordered nanoporous fluorescent films can be prepared for a variety of sensing applications.

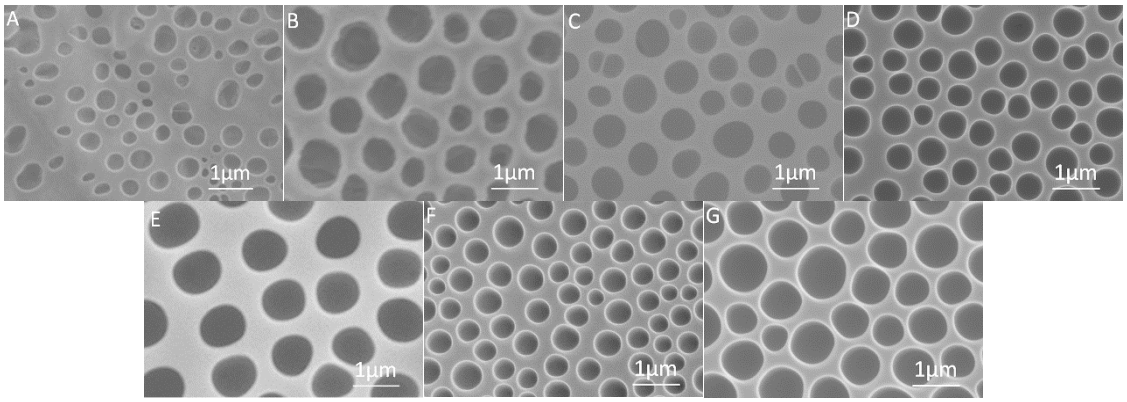

Figure 2.2 SEM images of a series of $PS_xPY_{0.1}$ and PS_4PY_x fluorescent films. (A) $PS_{0.5}PY_{0.1}$, (B) $PS_1PY_{0.1}$, (C) $PS_2PY_{0.1}$, (D) $PS_4PY_{0.1}$, (E) $PS_6PY_{0.1}$, (F) $PS_4PY_{0.05}$, (G) $PS_4PY_{0.2}$.

Table 2.1 Pore density (ratio of pore area in the whole film) of a series of $PS_xPY_{0.1}$ and PS_4PY_x fluorescent films.

Py-PS Films	Pore density (%)
$PS_{0.5}PY_{0.1}$	20.8±5.4
$PS_1PY_{0.1}$	41.1±2.0
$PS_2PY_{0.1}$	42.1±1.1
$PS_4PY_{0.1}$	43.4±2.0
$PS_6PY_{0.1}$	38.1±2.5
$PS_4PY_{0.05}$	30.8±1.3
$PS_6PY_{0.2}$	55.4±2.6

For solid-state sensing films, thickness plays a pivotal role, mainly due to the diffusion resistance of analyte vapors into the film.[30] The thickness of the dip-coated fluorescent polymer film in our study was about 2 μm, as measured by Dektek surface profiler. The overall film thickness is much higher than those of other reported fluorescent sensing films[46], but owing to its nanoporous surface structure, it possesses a comparable, if not better, sensing performance than much thinner films.

2.2.2 Sensing Performance of Py-PS Fluorescent Films

Figure 2.3A shows the time-dependent fluorescence spectra of a Py-PS film, prepared as described above. The emission peak at ~470 nm is assigned to originate from the pyrene excimer. Upon exposure of the film to saturated DNT vapor at ambient temperature, the fluorescence of the excimer is quenched by 35% within 2 min, by ~60% within 6 min, and after 30 min by about 90%. As a comparison, a smooth film of the same composition but prepared using evaporation conditions that did not allow the formation of the breath-figures, shows a slower response and overall ~20% lower quenching efficiency upon exposure to saturated DNT vapor.

The fluorescence quenching mechanism relies primarily on the photo-induced electron transfer (PET) from the excited pyrene excimers within the Py-PS films to the electron-

deficient nitroaromatics.[38,46] This is also supported by the relative positions of the computed frontier orbitals of the molecules involved (see below, Table 2.2).

Table 2.2 Saturated vapor concentrations, HOMO and LUMO energies of representative analytes and interferences[21]

Compound	Vapor concentration, ppb	HOMO, eV	LUMO, eV
Pyrene[46]	/	-5.33	-1.48
4-NT	6×10^4	-7.10	-3.19
1,3-DNT [5,82]	59.9	-7.9855	-3.4311
2,4-DNT	144	-7.7645	-3.2174
Chloranil[38]	1.001×10^4	/	-5.617

Previous studies have revealed that the efficiency of the fluorescence quenching of the solid film would depend on analyte's electronic structure, vapor pressure, diffusion of analytes in the films and the adsorptive affinity of the film to explosive molecules.[4,83,84] Table 2.2 summarizes the calculated orbital energies (at B3LYP/6-31G* level) as well as saturated vapor concentration of representative analytes investigated in this study. For nitro explosives, the low LUMO energies can accept the electron from the excited state of pyrene, and thus the nanoporous Py-PS film could be effectively quenched. Nitroaromatic explosives have π-electrons to facilitate their intercalative bindings with pyrene-PS film and also possess relative higher volatility. DNB has a slightly lower LUMO level compared to that of DNT (-3.4311 eV vs. -3.2174 eV), but it displays a lower quenching efficiency than that of DNT, which may be ascribed to its much lower vapor concentration compared to that of DNT (59.9 ppb vs. 144 ppb). 4-NT shows the highest fluorescence quenching efficiency in the study, possibly attributed to its highest vapor concentration (60 ppm) among the investigated nitroaromatic explosives. In contrast, it is surprising to note that, although chloranil has substantially lower LUMO energies and higher vapor concentrations than nitroaromatic explosives, much lower quenching efficiency was observed, which might be attributed to their weaker electrostatic interactions with sensing materials and a lower surface binding constant compared with that of nitro explosives. Not

surprisingly, electron-rich compounds (aniline) or the mixture of organic compounds in perfume fail to provide quenching response since they are not favorable for PET process.

The lack of spectral overlap between the DNT absorbance and Py-PS film emission excludes the probability of energy transfer from the excited film to DNT.[48] The presence of excimer emissions from Py-PS film shows that the loading of pyrene is high enough to form π-stacked Py dimers. The shape-persistent geometry of the PS scaffold presumably enables effective co-facial π-π stacking, allowing pyrene monomer and/or excimer units possible to be inserted in and between the phenyl groups of PS, thus contributing to the formation of extended conjugation of π electrons and efficient long-range energy migration in the Py-PS films.[38,46]

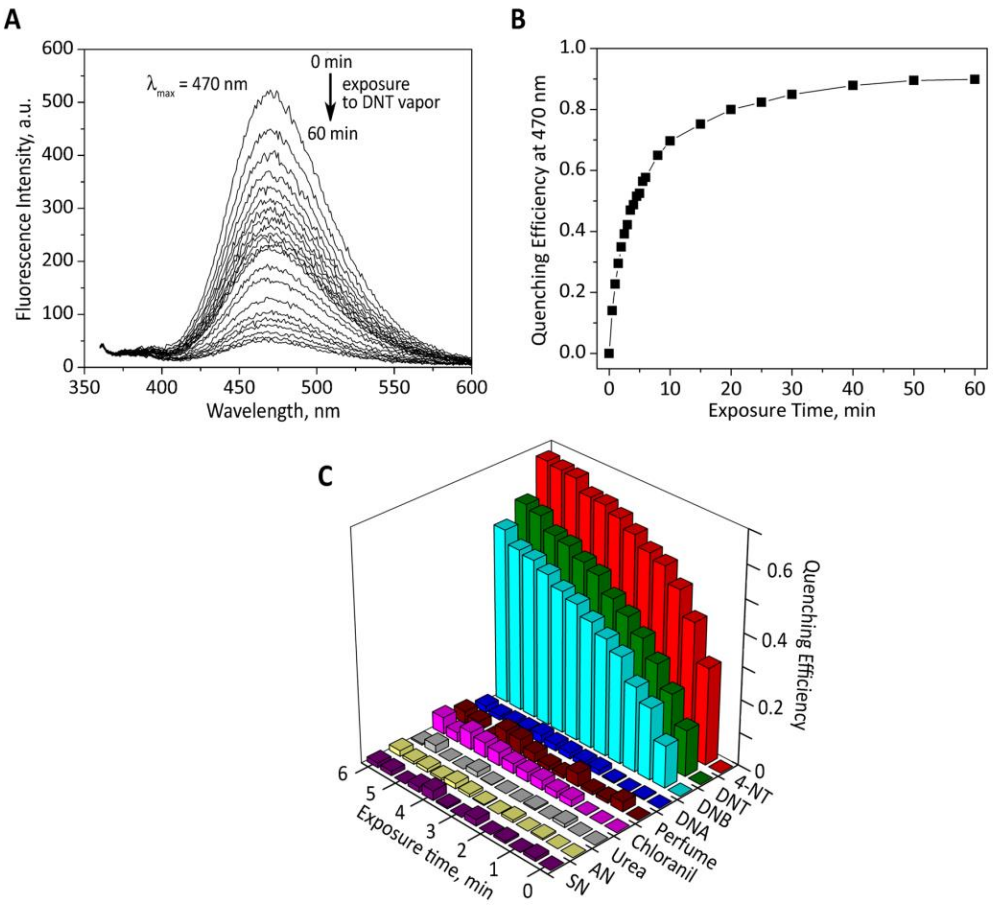

Figure 2.3 Fluorescence quenching profiles of 3D nanoporous Py-PS fluorescent film (0.1 M Py and 4-wt % PS). (A) The time-dependent fluorescence intensity upon exposure to equilibrium DNT vapor (the exposure time from top to bottom is 0, 0.5, 1, 1.5, 2, 2.5, 3, 3.5, 4, 4.5, 5, 5.5, 6, 8, 10, 15, 20, 25, 30, 40, 50, 60 min, respectively). (B) The time-dependent fluorescence quenching efficiency of 3D nanoporous Py-PS film at 470 nm exposed to saturated DNT vapor; (C) The time-dependent fluorescence quenching efficiency at Py excimer peak upon exposure of 3D nanoporous Py-PS film to saturated vapors of different analytes.

Selectivity is one crucial criterion in sensing (Figure 2.3C). Remarkable quenching efficiency was observed for the sensing film when exposed to nitroaromatic vapors such as 4-NT (68%), DNT (60%) and DNB (53%; values reported for the quenching of the pyrene excimer band after 6 min exposure to air saturated with nitroaromatic vapors at ambient temperature). The differences in the relative quenching efficiencies can be rationalized based on a combination of the electron acceptance ability and vapor pressure

of the nitroaromatics tested (see Table 2.2). Exposure to more electron-rich aromatic compounds such as 3,5-dinitroaniline (DNA) and commercial perfume did not lead to a significant fluorescence quenching. The absence of any significant quenching of the nanoporous Py-PS film upon exposure to strong electron-acceptors such as chloranil indicated that the fluorescent films were inert to this strong oxidant. Commonly used nitrogen fertilizers such as urea, ammonium nitrate (AN) and sodium nitrite (SN) induce only negligible quenching. The results show that Py-PS films exhibit selectivity towards the identification of nitroaromatic explosive compounds.

2.2.3 The Role of Pyrene Doping on the Sensing Ability of Py-PS Films

To investigate the role of Py-doping on the quenching efficiency of the sensing film upon exposure to DNT, we performed studies on films prepared of solutions of varying polystyrene and pyrene concentrations. Figure 2.4 presents the results, demonstrating that both the PS and Py concentrations in the solutions (the films were prepared from by dip-coating) have a significant impact on quenching efficiency. In one series (Figure 2.4A), the pyrene concentration was fixed at 0.1 M and films from PS solutions of varying concentrations (from 0-wt% to 6-wt%) were prepared. As the PS concentration increases (from 0-wt% to 4-wt%), the quenching efficiency (after 6 min) increases to a maximum of 60%. Further increase of PS concentration to 6% reduces the quenching efficiency to 42%. Consequently, 4-wt% of PS was selected for subsequent study of the effect of Py concentration.

At a fixed PS concentration of 4-wt%, the quenching efficiencies for Py-PS films prepared with pyrene concentration varying from 0.05 to 0.2 M, were 33%, 60%, and 36% after a 6 min exposure to saturated DNT vapor (Figure 2.4B), indicating that the

combination of 4-wt% PS and 0.1 M pyrene generated the best DNT sensing film. The possible molecular origin of the performance differences will be discussed below.

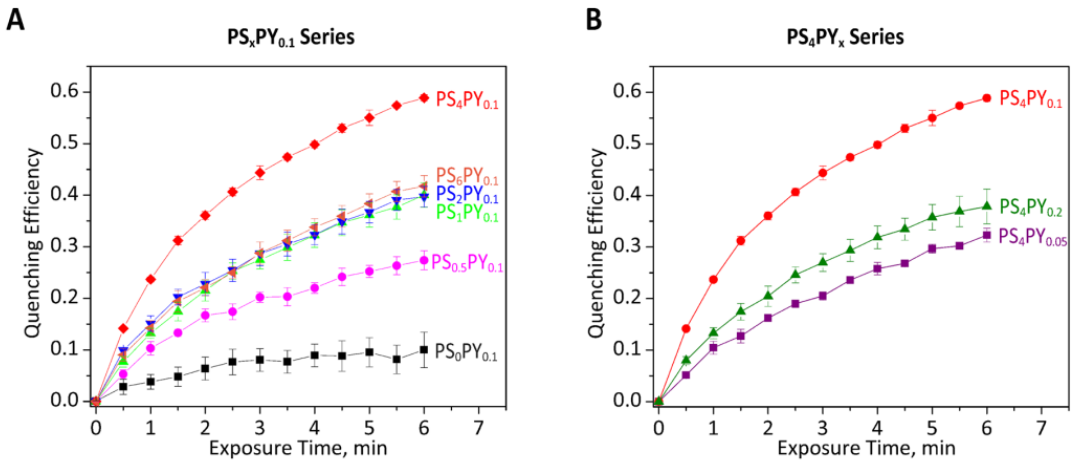

Figure 2.4 Effect of composition of dipping coating solution on fluorescent quenching efficiencies. (A) The effect of PS concentration (with 0.1 M Py fixed) on time-dependent fluorescence quenching efficiency upon exposure of film to saturated DNT vapor at Py excimer peak; (B) The effect of Py concentration (with 4-wt% PS fixed) on time-dependent fluorescence quenching efficiency upon exposure of film to saturated DNT vapor at Py excimer peak. Different Py-PS fluorescent films were prepared using different Py and PS concentrations. The subscript of PS in PS_xPY_z indicates the wt% of PS while the subscript of PY in PS_xPY_z indicates the molar concentration of pyrene (e.g., the $PS_4PY_{0.1}$ film was prepared using 4-wt% PS and 0.1 M pyrene in THF).

2.2.4 XRD Patterns of Py-PS Fluorescent Films

XRD patterns provide a direct signature of regular order, and any observed layer d-spacing can be compared to the molecular dimensions for the determination of likely molecular arrangements.[85] Thus, the degree of crystallinity of pyrene in polystyrene can be studied by analysis of the XRD patterns. Any spatial restriction of pyrene is known to influence excimer formation.[86] The XRD patterns obtained for the films (Figure 2.5) indicate the existence of pyrene crystallites in the Py-PS composites films (the peaks observed can be assigned to the (001), (110) and (220) peaks of pyrene; ICDD No. 00-024-1855), while amorphous polystyrene served as a hydrophobic matrix for pyrene

crystal growth. The d spacing derived here from the 110 and 220 peaks is 7.59 and 3.80 Å, respectively. The d-spacing of 3.80 Å is in good agreement with the reported face-to-face pyrene stack distance value of ~ 3.18- 3.49 Å.[86,87] The ratios of peak intensity assigned to pyrene crystallites do not increase monotonically with the variation of the PS to Py ratio used to form the films (see Table 2.3 for a listing of the I(110)/I(001) and I(220)/I(001) ratios).

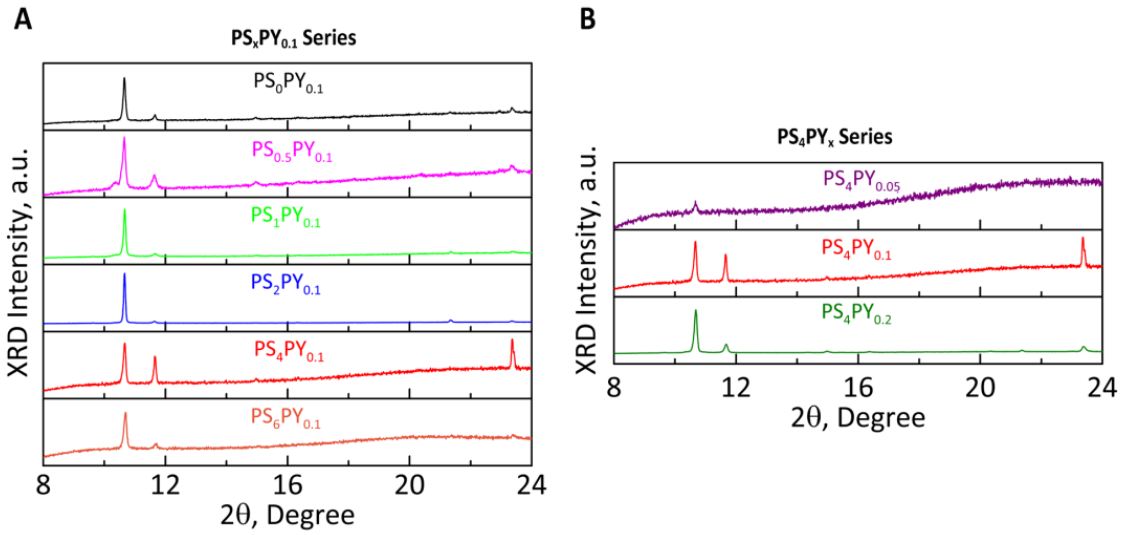

Figure 2.5 *θ-2θ* X-ray diffraction (XRD) spectra of a series of (A) $PS_xPY_{0.1}$ and (B) PS_4PY_x fluorescent films. The signals at ~10.70°, ~11.65° and ~23.35° can be assigned to the (001), (110) and (220) peaks of pyrene crystals.

However, it is likely of relevance to note that the system of best sensing performance, the $PS_4PY_{0.1}$ film, is also the film with the apparent highest degree of pyrene crystallinity. Evidently, the approximate 1:4 molar pyrene ring : styrene ratio of this film is conducive of forming pyrene crystallites and presumably also supports the organization of the pyrene into functional excimers. Wang et al.[38] reported that the shape-persistent geometry of the PS scaffold could potentially enable effective co-facial π-π stacking, allowing pyrene monomer and excimer units possible to be inserted in and between the phenyl

groups of the PS chains. Swager and co-workers proposed and demonstrated that one-dimensional π-π stacking is highly favorable for exciton transportation via co-facial intermolecular electronic coupling ("molecular wire" amplification).[29] In this study, one-dimensional pyrene and excimers doped into polystyrene similar to that of pyrene salt might be formed[87,88], and thus results in a facilitated long-range exciton migration and achieves amplified fluorescence quenching similar to "molecular wire".

Table 2.3 Summary of structural, optical, electrochemical, and frontier orbital properties of Py-PS fluorescent films of varying composition

Py-PS Films	$I_{(110)}/I_{(001)}$	$I_{(220)}/I_{(001)}$	I_{ex}/I_{mon} [a]	E_g^{opt}(eV) [b]	E_{ox}'(V) [c]	E_{HOMO} (eV)	E_{LUMO} (eV) [d]
$PS_0PY_{0.1}$	0.12	0.11	2.75				
$PS_{0.5}PY_{0.1}$	0.26	0.13	4.33	3.27	0.99	-5.39	-2.12
$PS_1PY_{0.1}$	0.05	0.02	6.02	3.49	1.04	-5.44	-1.95
$PS_2PY_{0.1}$	0.03	0.02	8.77	3.52	1.07	-5.47	-1.95
$PS_4PY_{0.1}$	0.68	0.74	14.32	3.56	1.08	-5.48	-1.92
$PS_6PY_{0.1}$	0.15	0.09	6.60	3.57	1.22	-5.62	-2.05
$PS_4PY_{0.05}$	-	-	3.69	3.57	1.30	-5.70	-2.13
$PS_4PY_{0.2}$	0.19	0.12	7.06	3.54	1.19	-5.59	-2.05

[a] I_{ex} was obtained using excimer peak intensity at ~470 nm while I_{mon} was the peak intensity at ~395 nm. [b] Optical band gap is estimated from the low-energy band edge of the UV-vis spectrum (see Figure 2.6). The absorption results were obtained using dip-coating films of original solutions diluted by a factor of 10 because the UV-vis spectra of original Py-PS films are out of the detection range of the spectrophotometer used. The experiments were conducted at least three times and the fits were performed three times, and average value was reported, error was less than 0.005 eV, linear fitting R square was larger than 0.98. [c] Estimated onset potential of oxidation from the cyclic voltammetry results. [d] LUMO values calculated from the band gap and HOMO values.

2.2.5 Optical Properties of Py-PS Fluorescent Films

The absorption and fluorescence spectra of thin films of different composition are shown in Figure 2.6, and the corresponding data are also summarized in Table 2.3. The absorption spectra of Py-PS films showed the characteristic three bands at about 311, 325 and 342 nm, corresponding to the vibrational bands of the $S_0 \rightarrow S_2$ transition of pyrene ring.[38] Furthermore, two small peaks can also be observed at 355 nm and 373 nm, which

correspond to the vibronic bands of $S_0 \rightarrow S_1$ transition of pyrene rings.[89] At constant Py concentration (from $PS_0PY_{0.1}$ to $PS_6PY_{0.1}$), a shift of the absorption peaks was observed, indicating a changing degree of interaction between the pyrene units in the polymer.[86,90]

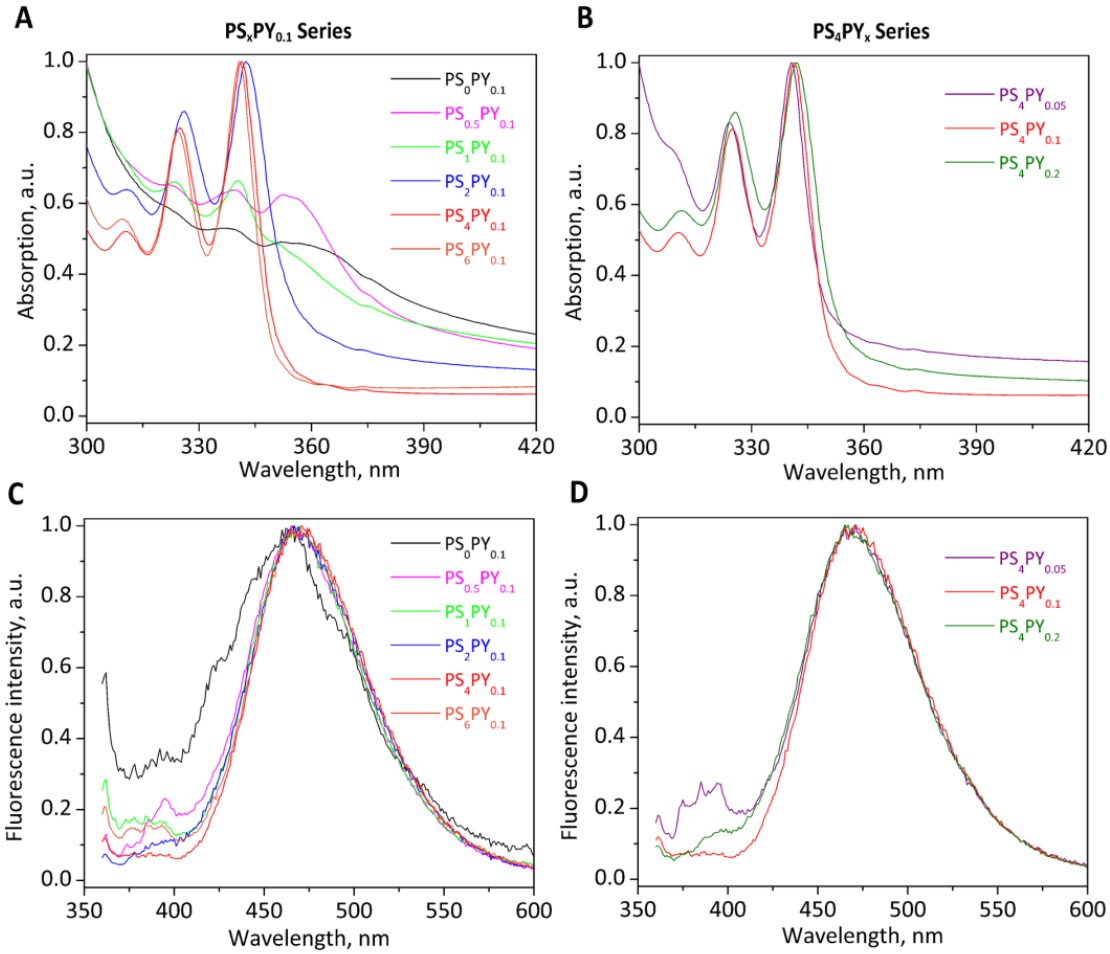

Figure 2.6 Absorption and emission spectra of a series of $PS_xPY_{0.1}$ and PS_4PY_x fluorescent films. (A) and (B) Normalized absorption spectra of a series of $PS_xPY_{0.1}$ and PS_4PY_x fluorescent films, respectively (prepared with 10 × dilution solution because the UV-vis spectra of original Py-PS films are out of the detection range of spectrophotometer). (C) and (D) Normalized emission spectra of a series of $PS_xPY_{0.1}$ and PS_4PY_x fluorescent films, respectively.

The UV-vis spectra also allow the estimation of the optical absorption band gap.[48, 4991,92] The optical band gap of the polymer can be calculated using Eq. 2.1, with A being the absorbance and E_g is the band gap corresponding to a particular absorption of photon

energy hν.[93] The values of the direct optical band gap are determined by the extrapolation of the linear region to zero absorption (Ahν = 0).

$$Ah\nu = (h\nu - E_g)^{1/2} \tag{2.1}$$

The extrapolating graphs are shown in Figure 2.7 and the data derived are summarized in Table 2.3. Thus, the optical band gap changed with PS and Py concentrations. These band gap changes are further confirmed by nonsymmetric increases in the highest occupied molecular orbital (HOMO) and lowest unoccupied molecular orbital (LUMO) energies discussed below, similar to the finding reported by Facchetti and co-workers.[94]

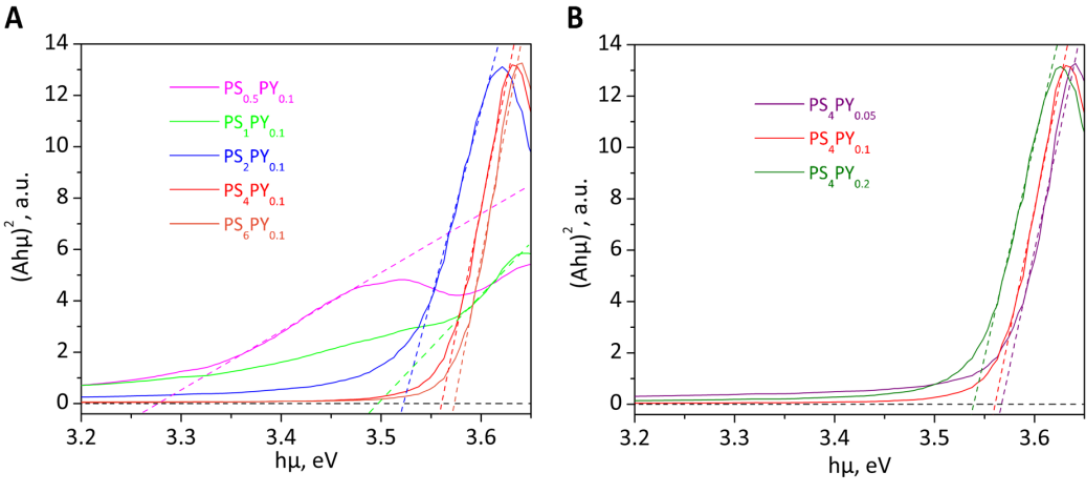

Figure 2.7 $(Ah\nu)^2$ versus the photon energy hν. The extrapolation of the linear region to zero absorption allows us to determine gap energy of Py-PS fluorescent films (the data from Figure 2.6 A, B).

The dependence of the pyrene concentration in the polymer on the excimer formation[70] was determined by examining the fluorescence ratio of the pyrene excimer (I_{ex}, at 470 nm) to pyrene monomer emission (I_{mon}, at 395 nm) (I_{ex}/I_{mon}). The data are presented in Table 2.3. Higher I_{ex}/I_{mon} ratios suggest that the pyrene molecules are located more closely to one another[90], which benefits the fluorescence quenching of pyrene, increasing

the sensitivity of explosives detection[70]. This ratio is 14.3 for the film made of 0.1 M Py and 4 wt % PS. A reduction or increase of the pyrene-styrene ratios leads to a degradation of the I_{ex}/I_{mon} ratios ranging from 2.75 to 8.77 (Table 2.3), again indicating that the efficiency of the excimer formation in $PS_4PY_{0.1}$ film is much higher than in other films. The result here corroborates the XRD data and confirms that $PS_4PY_{0.1}$ film possesses the highest degree π-π stacking of pyrene in PS.

2.2.6 Electrochemical Characterization of Py-PS Fluorescent Films

Cyclic Voltammetry is a dynamic electrochemical method to determine the redox behaviour as well as to estimate the HOMO and LUMO energy levels of the materials under investigation.[95] The oxidation process corresponds to the removal of electron from the HOMO energy level, while the reduction potential corresponds to the LUMO energy level of the materials. To provide a better insight about the relative energies of the orbitals of Py-PS composite polymers, and thus the feasibility of the energy transfer, we carried out cyclic voltammetry studies with dip-coated film on glassy carbon electrodes to obtain the oxidation potentials (E_{ox}') (Figure 2.8). According to the empirical relationship proposed by Bredas et al. based on a detailed comparison between valence effective Hamiltonian calculations and experimental electrochemical measurements[96], the solid state HOMO level correlates to E_{ox}' (vs. SCE), the onset potentials of oxidation process of the polymer (Eq. 2.2). The onset potentials are determined from the intersection of the two tangents drawn at the rising current and baseline charging current of the CV traces.[97] The relation can be expressed as

$$HOMO = -(E_{ox}' + 4.4)eV \quad (2.2)$$

The onset oxidation potentials and valence band of Py-PS films were obtained using the CVs shown in Figure 2.8. We observed that the valence band can be tuned through doping Py into polymers. For the Py-PS films prepared with fixed Py concentration, the valence band decreases with the increase of PS concentrations, while the band gap increases (as determined optically, see above). Both the change of band gap and the change of valence band follow an asymmetric trend, and thus the conduction band of fluorescent films demonstrates a different trend. If the distinction between optical and electronic band gap is ignored, the conduction band can be obtained by adding the valence band and the optical band gap.[98-100] The conduction band of $PS_4PY_{0.1}$ film is highest, with a value of -1.92 eV, which explains its best quenching efficiency upon exposure to DNT. The LUMO of DNT is -3.22 eV. The driving force of PET process for DNT quenching on $PS_4PY_{0.1}$ film thus is ~1.30 eV. The conduction bands of the various fluorescent films studied are ranged from -1.92 eV to -2.13 eV. The LUMO level of the nitroaromatics studied in this research is lower than the estimated LUMO of fluorescent films, validating that a PET processes is the molecular origin of the fluorescence quenching.

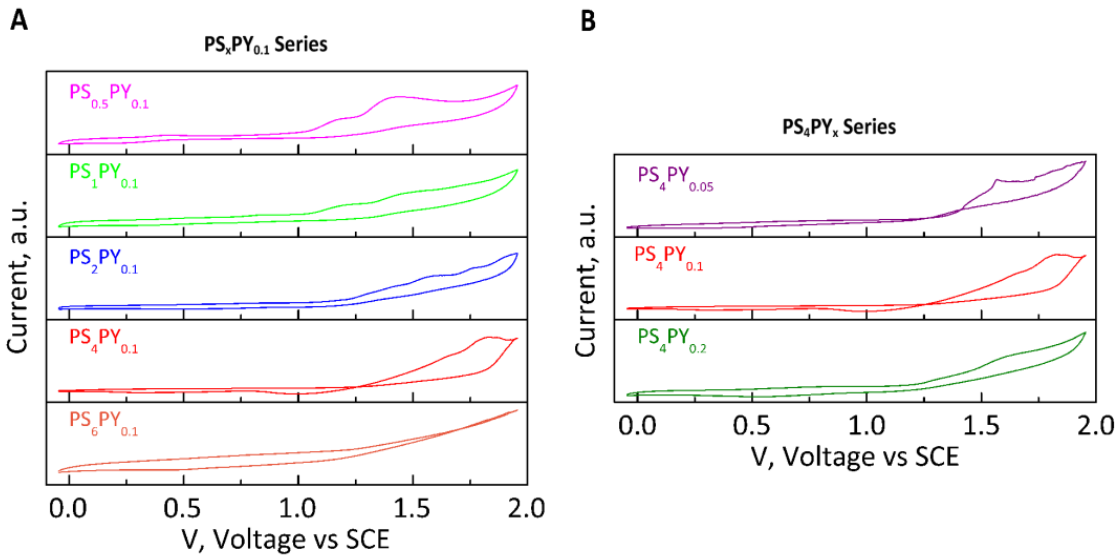

Figure 2.8 Cyclic voltammograms of a series of (A) $PS_xPY_{0.1}$ and (B) PS_4PY_x fluorescent films in acetonitrile with 0.1mol/L NBu_4PF_6 at a scan rate of 50 mV/s.

2.3 Conclusions

In this study, a novel 3D nanoporous fluorescent film was prepared via simple dip-coating of PS and Py solutions, and then its application for the sensitive and selective detection of explosive vapor was investigated, whereby we optimized the sensing film with respect to morphology and electronic properties by varying the pyrene : styrene molar ratios. Upon exposure of the best sensing film ($PS_4PY_{0.1}$) to saturated DNT vapor, the fluorescence quenching of excimer peak at 470 nm was observed to be 60% within 6 min and to reach a plateau of 90% after 30 min. The sensing Py-PS films possess an excellent selectivity against common interferents.

This study is, to the best of our knowledge, the first report of a novel self-assembled 3D nanoporous array fluorescent film via a simple dip-coating preparation method that is utilized for sensitive and selective detection of nitro explosives. The presence of three-dimensional nanoporous array of holes in fluorescent film enables a high porosity and fast

quenching efficiency upon exposure to explosive vapor. In addition, characterization of the as-prepared films using XRD, UV-vis and fluorescence spectroscope, and cyclic voltammetry indicates that the crystal structure of pyrene in Py-PS film, electronic structure, band gap and conduction band of fluorescent polymer film can be tuned via the pyrene-doping degree. This, in turn, results in the variation of the fluorescence quenching efficiency of the sensor. This study may provide insights into the design of novel nanostructured sensing polymer doped with small fluorophore molecules and the present findings offer a new research direction for the design of three-dimensionally organized nanoporous fluorescent sensing films.

Chapter 3

Super-hydrophobic Fluorescent Sand for Buried Explosive Detection

There are about 110 million unexploded landmines buried on 20th century battlefields around the world.[101] On average they kill or maim more than 100,000 people each year, 30-40% of that are children. In addition, they prevent the use of large areas of arable land.[102] Even though billions of dollars are spent each year on the demining effort, it would take around 450 years using current methods to neutralize all hidden landmines (assuming no newly laid landmine). Current landmine clearance rate is about 10-20 times slower than current landmine laying rate[103], which makes completely demining around the world an impossible mission based on current techniques.

We have synthesized fluorescent polymer films for explosives vapor detection in the previous work, but it is not convenient to apply this kind of film for buried explosives detection. Therefore, in this work, we prepared fluorescent sand (called as "smart sand") through a simple coating method, and then applied the sand for buried explosives detection.

Abstract

Explosive-sensitive fluorescent sand ("smart" sand) was prepared through the simple coating of polystyrene/pyrene/NBu_4PF_6 composite on normal sand. The as-prepared "smart" sand was characterized using SEM, EDS, XRD, FT-IR, Raman, and UV-vis. Further analysis of contact angle and fluorescence emission spectra confirm that the explosive-sensitive fluorescent composite film coats on the surface of the sand, endowing "smart" sand both strong fluorescence and super-hydrophobicity, which provides an excellent sensing material for buried nitroaromatic

explosive sensing, presumably due to its strong affinity with nitroaromatic explosive vapor. The detection of buried explosives in soil was achieved and validated through quenched spots on a thin layer of "smart" sand paved on the top of soil. The quenched area and decreased intensity vary with the amounts and depths of 2,4-DNT buried in soils. Such detection can be performed using a handheld UV lamp and observed by naked eyes, thus providing great potential and advantage for large-scale landmine detection and mapping.

3.1 Experimental

3.1.1 Materials

Tetrabutylammonium hexafluorophosphate (NBu_4PF_6, 98%), polystyrene (PS, M_w=350,000) and tetrahydrofuran (THF) were purchased from Sigma-Aldrich. Pyrene (Py, 98%) was bought from Acros Organics. 2,4-dinitrotoluene (2,4-DNT, 97%) was purchased from Sigma-Aldrich. All the chemicals were used as received. Normal sand was collected from beach in Connecticut. The main composition of sand was Si, Al, and O with small amount of Na, Mg and Fe.

3.1.2 Preparation of "Smart" Sand

The fluorescent polymer composite solution was prepared following the same protocol reported in the previous report.[38] Briefly, NBu_4PF_6, polystyrene and pyrene (mass ratio: 2.467/1.976/1) were dissolved in THF to yield a solution with a total concentration of 0.1101 g/mL and then stirred for 1 hr to obtain a homogeneous solution. After that, 10 g of sand was added into 10 mL of fluorescent polymer composite solution. After well-mixing, the sand/solution mixture were maintained at room temperature for 30 min for sufficient interaction between sand and sensing materials in solution. Finally, the supernatant was poured into a storage bottle and sand was

transferred to a glass container in a chemical hood for solvent evaporation at room temperature, resulting in fluorescent polymer composite film coated sand ("smart" sand).

3.1.3 Characterization

The morphologies of normal sand and "smart" sand were obtained using a JEOL 6330F Field Emission scanning electron microscope (SEM) at an acceleration voltage of 15 kV. Elemental analysis of both normal sand and "smart" sand was accomplished with an energy dispersive X-ray spectroscopy (EDS) analysis system. The X-ray diffraction patterns were obtained on a Bruker D2 Phaser X-ray diffractometer using Cu Kα radiation at a rate of 0.01^{o} 2θ s^{-1} and operated at 15 kV and 10 mA. Fourier transform infrared (FT-IR) spectra were collected on Nicolet 560 Fourier spectrometer using KBr pellets. Raman spectra were collected using a Renishaw 2000 Ramascope Micro-Raman coupled with a 514 nm argon-ion laser, a Leica microscope and a charge-coupled device detector. Diffuse-reflectance UV-Vis spectra were collected using a Shimadzu UV-2450 UV-Vis spectrophotometer in the range of 300-700 nm. For each test, 0.2 g sand was diluted by 2.0 g $BaSO_4$. To study the fluorescence spectra of "smart" sand and normal sand, the sand was fixed on the glass slides by sealant. Fluorescence emission spectra were measured through a Varian Cary Eclipse fluorescence spectrometer (Agilent Technologies), and the spectra were recorded in the range of 360-600 nm with an excitation wavelength of 340 nm. Hydrophobicity of sand was investigated with a Pendant Drop Tensiometer OCA 20 (Future Digital Scientific Corp).

3.1.4 Explosive Detection

Different amounts of 2,4-DNT were buried in soil at various depths in Petri dishes. The soil with buried explosive was stored at room temperature for 5 days in order to let explosive vapor reach the surface layer of soil. Afterwards "smart" sand was manually "sprayed" on the soil surface to

form a thin layer, a handheld UV lamp (Spectroline, Spectronics Coop, λ_{ex}=254nm) was used to observe the quenched spots by the naked eye. The optical images were taken to show the quenched spots which indicate the position of buried explosives. Scheme 3.1 shows the illustration for the detection of buried explosives using "smart" sand under UV light by the naked eyes.

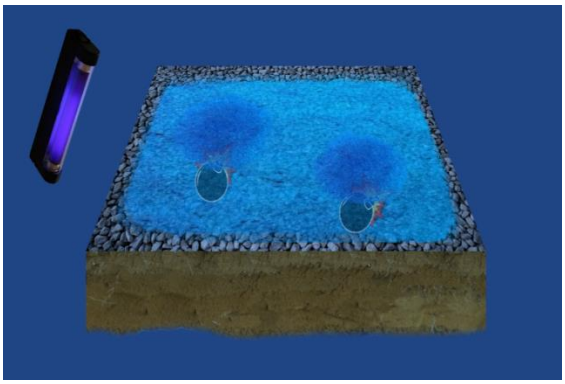

Scheme 3.1 Schematic illustration for the detection of buried explosives under UV light using "smart" sand.

3.2 Results and Discussion

3.2.1 Characterization of "Smart" Sand

Figure 3.1 shows the typical SEM images of the sand before and after modification of polymer sensing composites. The images show similar morphology implying that the coating of fluorescent polymer composite does not change the structure of the sand. Overall speaking, the size of the sand ranges from 50 to 200 μm, with a majority about 100 μm. The EDS spectra (Figure 3.1 C, D) were employed to investigate the composition difference of the sand before and after functionalization. Compared with the normal sand, the carbon ratio in EDS spectra of the "smart" sand increases greatly, indicating that polymer sensing composite was successfully coated on the surface of the sand. In addition, the appearance of fluoride (F) and phosphorus (P)

in EDS spectra with a F to P molar ratio of 6.5, approximately equal to the stoichiometric ratio in NBu_4PF_6, confirms the existence of NBu_4PF_6 in the "smart" sand.

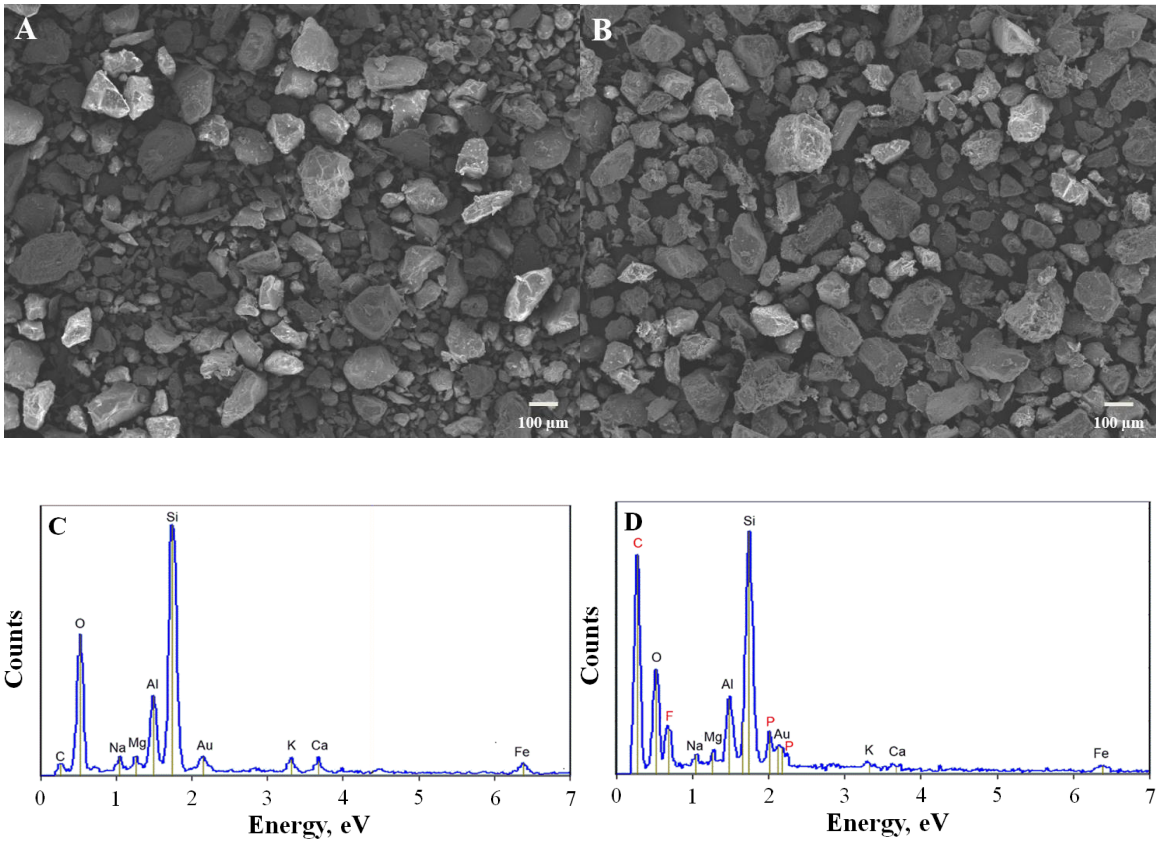

Figure 3.1 Typical SEM images of normal sand (A) and "smart" sand (B); EDS spectra of normal sand (C) and "smart" sand (D).

XRD was carried out to further characterize the compositions and crystal structures of both "smart" and normal sand, as shown in Figure 3.2. As reported previously, pyrene and NBu_4PF_6 can form crystals and show complicated XRD patterns.[70] Compared with the spectrum of the normal sand, the *2θ* diffraction peaks of the "smart" sand at 8.5°, 8.9°, 10.4°, 10.8° and 13.6° can be assigned to pyrene or NBu_4PF_6, indicative of the presence of pyrene and NBu_4PF_6.

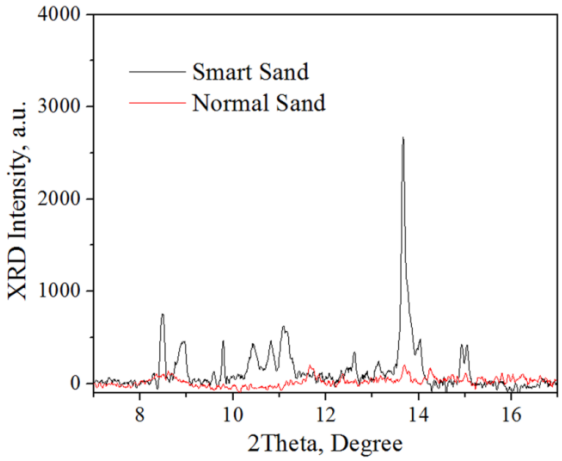

Figure 3.2 XRD spectra of normal sand and "smart" sand after baseline subtraction.

As shown in the FT-IR spectra of Figure 3.3, compared with the result of the normal sand, several new peaks corresponding to PS/Py/NBu_4PF_6 are observed in that of the "smart sand". The new peaks in the ranges of 3000-3100 cm^{-1}, 2800-3000 cm^{-1} and 1430-1490 cm^{-1}, and at 840 cm^{-1} and 559 cm^{-1} are presumably attributed to the benzene derivatives from PS and pyrene, the saturated stretch of C-H in alkanes from PS and NBu_4PF_6, the aromatic C=C, the PS and NBu_4PF_6[104,105], the C-H wagging vibration of pyrene (or the vibration of C-N in R_3N group from NBu_4PF_6)[105,106] and the P-F of NBu_4PF_6[107], respectively. It should be noted that the absence of the peak in the range of 1100-1300 cm^{-1} (corresponding to C-O stretch of THF) indicates THF solvent completely evaporates and does not exist in the "smart" sand.

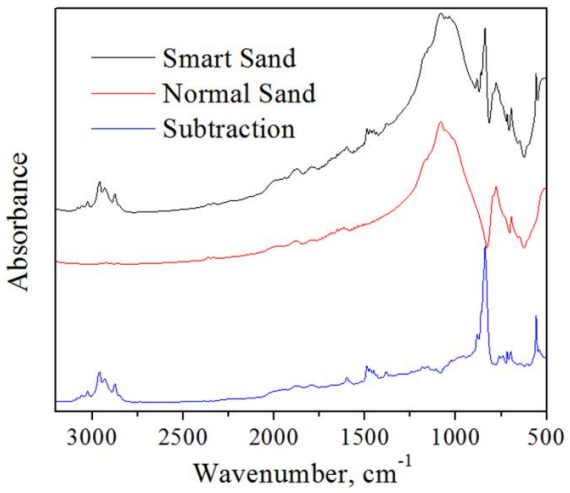

Figure 3.3 FT-IR spectra of normal sand and "smart" sand (blue line was obtained by subtraction of the spectrum of normal sand from that of "smart" sand).

Raman is a sensitive technique which can detect compositional changes on the surface of materials. Comparing Raman spectra of both samples (Figure 3.4), several new peaks at 1243 cm^{-1}, 1408 cm^{-1}, 1598 cm^{-1} and 1630 cm^{-1} observed after chemical modification of the normal sand can be presumably ascribed to pyrene, in good agreement with literature reports.[108,109] The peak at 1598 cm^{-1} may also be contributed by polystyrene.

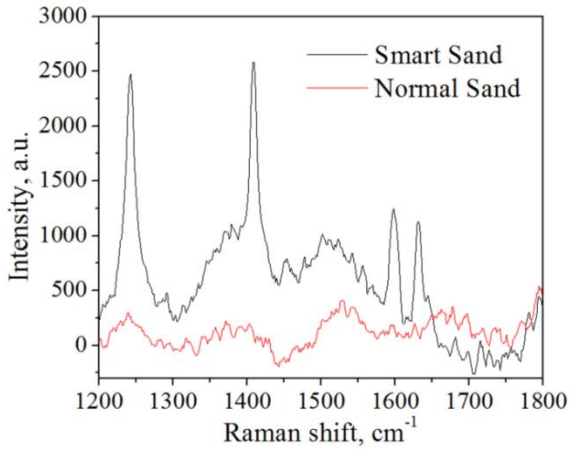

Figure 3.4 Raman spectra of "smart" sand and normal sand after baseline subtraction.

The difference in UV-Vis spectra of the two samples (Figure 3.5) is two strong absorption bands at 338 nm and 323 nm, possibly corresponding to the vibrational bands of the $S_0 \rightarrow S_2$ transition of pyrene rings.[23,38]

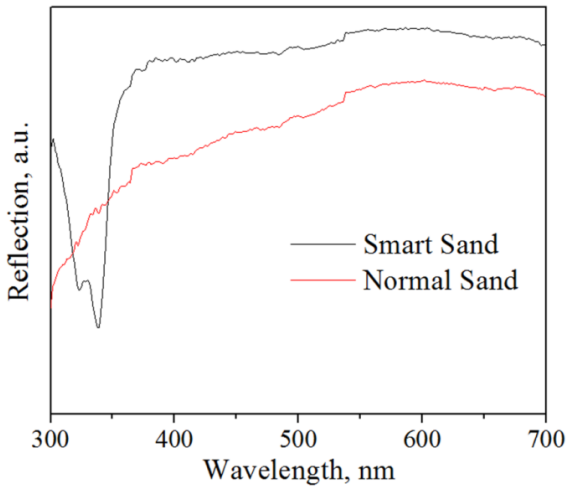

Figure 3.5 UV-vis reflection spectra of normal sand and "smart" sand.

In regards to the fluorescence, the normal sand has practically no fluorescence, while the "smart" sand exhibits strong characteristic fluorescence intensity from polymer composite. This can be observed by the color difference (dark and shiny, respectively) under the UV light (data not shown). Figure 3.6 shows that the fluorescence emission spectrum of the "smart" sand contains three obvious peaks (374 nm, 384 nm, 394 nm), which are consistent with those of the monomeric pyrene from singlet excited state in the range of 370-400 nm.[64] It should be noted that the emission peak of pyrene excimer at 470 nm is not observed in this study because the formation of pyrene excimer of this mixture may require high solvent vapor pressure as reported previously.[70]

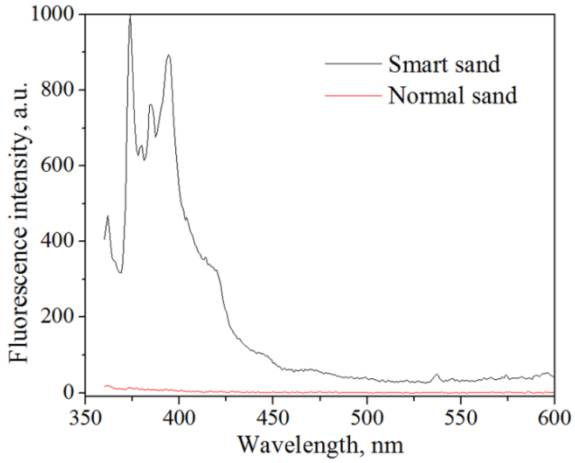

Figure 3.6 Fluorescence emission spectra of normal sand and "smart" sand.

To examine the hydrophobicity of the sand, 10 µL of water was added on both samples, respectively. As expected, the water droplet was absorbed by the normal sand indicative of the hydrophilic surface. In the case of the "smart" sand, instead of being absorbed by the sand the water droplet rolls on the surface, resulting in a coating of the sand. As the coated water droplet was transferred to a glass slide, a "contact angle" of ~150^{o} was obtained through Pendant Drop Tensiometer OCA 20 (Figure 3.7A). Furthermore, the coated water droplet can roll freely around the surface of tissue paper (KIMTECH Kimwipes) as shown in Figure 3.7B, indicating high hydrophobicity of the "smart" sand. Furthermore, as both sands were added into water, the normal sand precipitated in water, while "smart sand" floated on top of the water surface due to its super hydrophobicity. The super hydrophobicity endows the "smart" sand excellent property for the detection of aromatic explosive vapors due to the strong affinity between them.

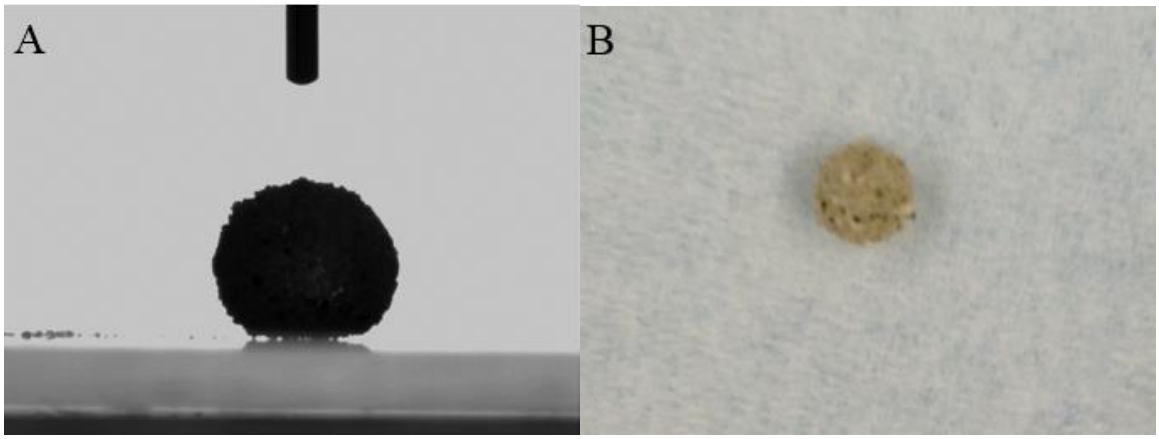

Figure 3.7 (A) Contact angle image of 10 μL water droplet "wrapped" by "smart" sand on glass surface; (B) A picture of 10 μL water droplet "wrapped" by "smart" sand on Kimwipes paper.

The hydrophobicity of samples with different coating compositions was also investigated. Sand coated with only pyrene is less hydrophobic than that coated with PS/Py or NBu_4PF_6/Py. While sand coated with PS/Py/ NBu_4PF_6 possesses the highest hydrophobicity. It is well-known that PS is a hydrophobic polymer and that the fluorinated material such as NBu_4PF_6 also promotes hydrophobicity of the surface via reducing the surface tension.[110] Therefore, the synergistic effect between PS and NBu_4PF_6 contributes to the super-hydrophobicity of the "smart" sand.

3.2.2 Buried Explosive Detection

The applicability of the "smart" sand for detecting buried explosives is examined under the conditions of different amounts of 2,4-DNT, which was buried under soil at different depths. As shown in Figure 3.8, 0.5 g of 2,4-DNT was buried under soil at a depth of 1 cm. The quenched spots of the "smart" sand sprayed on the soil surface indicate the position of buried explosives underneath the soil at the center of the Petri dish, while other parts remain fluorescent. This provides a convenient detection method to identify the buried explosives by naked eyes using a

handheld UV lamp in 30 min. The quenching became more significant with increasing time until it was gradually saturated after 5 hrs.

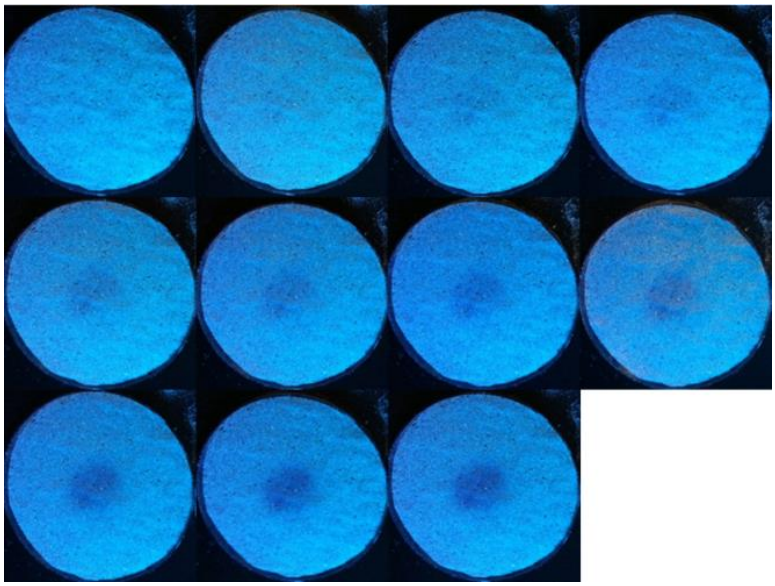

Figure 3.8 UV (λ_{ex}=254nm) excited image of "smart" sand for buried explosive detection (0.5 g 2,4-DNT at a depth of 1 cm) at different contact time (0, 15 min, 30 min, 1 hr, 1.5 hrs, 2 hrs, 5 hrs, 8 hrs, 10 hrs, 12 hrs, and 21 hrs) after "smart" sand is delivered to the soil surface.

Such detection of 2,4-DNT vapor generated from the solid 2,4-DNT underneath the soil involves the photo-induced electron transfer from the sensing polymer composite film (PS/Py/NBu_4PF_6) to the lowest unoccupied molecular orbital of 2,4-DNT molecules.[38,45] The saturated 2,4-DNT vapor concentration at 25 ^oC is 193 ppb. Sufficient time (5 days) is given for 2,4-DNT vapor to diffuse to the soil surface and react with the sensing polymer composite film.[111] The efficiency of the fluorescence quenching is anticipated to depend on both diffusion of the analytes in the films and the adsorptive affinity of the film to the explosive molecules.[83,84] As both nitroaromatic compounds and organic fluorescent film are hydrophobic, they can easily interact with each other through van der Waals or dipole-dipole forces. It is also possible that the π-π interactions and hydrophobic interactions between hydrophobic nitro-aromatic moieties and the super-

hydrophobic PS/Py/NBu_4PF_6 sensing materials can further enhance the adsorption of 2,4-DNT vapor, and thus achieve more efficient photo-induced electron transfer between the analytes and sensing composite.

In general, both area and fluorescence intensity of quenched spots are greatly dependent on the quantity and depth of the buried explosive.[111] The effects of the two parameters on the fluorescence quenching were investigated (5 hrs) after the "smart" sand was transferred to the soil surface. Figure 3.9 shows that in spite of successful detection of buried explosives in all cases, the quenched area increases with increased quantity and decreased distance from the soil surface of the buried explosive. These results demonstrate that under the fixed detection time, the fluorescence intensity and the area of the quenched spots can be used as an index of the amount or depth of buried explosives. However, it should be noted that soil type can also affect the diffusion of the explosive vapor, resulting in different quenching performance.[111] This is not investigated in this study.

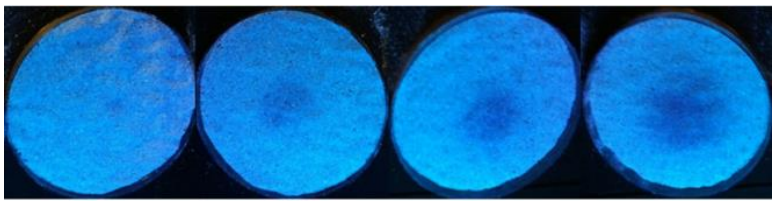

Figure 3.9 UV (λ_{ex}=254nm) excited image of "smart" sand for buried explosive detection after 5 hrs contact time under various buried conditions (from left to right): 0.2 g 2,4-DNT at 1 cm, 0.5 g 2,4-DNT at 1 cm, 0.2 g 2,4-DNT at 0.75 cm, and 0.5 g 2,4-DNT at 0.75 cm.

After explosive detection experiments, the "smart" sand inside and outside of the quenched spots were collected individually and their fluorescence spectra were examined as shown in Figure 3.10. Fluorescence peak intensity at 394 nm of the quenched sand was found to be 42.9% of that of the unquenched one. Moreover, the fluorescence intensity of sample from unquenched region

after detection was practically the same as that of the fresh "smart" sand (Figure 3.6 and Figure 3.10), implying that the unquenched polymer film remains almost unchanged after detection. Therefore, the observed fluorescence quenching is solely attributed to its interaction with explosive molecules. Furthermore, other components in soil do not have noticeable quenching/interference effect on the fluorescence. In conjunction with the easy procedure to manufacture the "smart" sand, these results suggest that the developed explosive sensing platform has great potential and advantage for large-scale landmine detection and mapping.

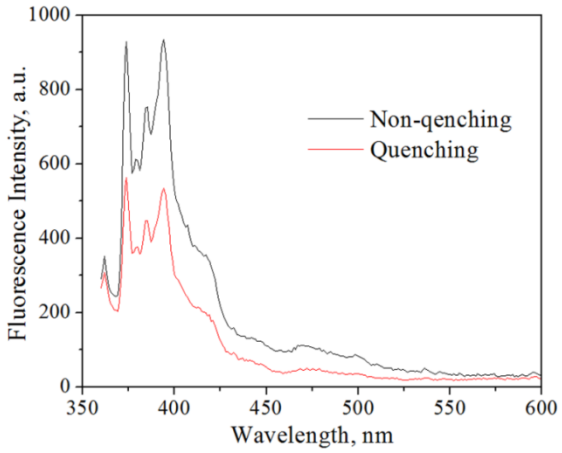

Figure 3.10 Emission spectra of the sand collected from the quenched spot and non-quenched part after the detection of buried explosives (0.5 g 2,4-DNT in depth of 0.75 cm; 5 hrs contact time between "smart" sand and soil surface).

3.3 Conclusions

Super-hydrophobic explosive-sensitive fluorescent "smart" sand was successfully prepared by a simple coating method. SEM results suggest that the functionalization process does not change the surface morphology of sand. EDS, XRD, FT-IR, Raman, UV-Vis, fluorescence spectra and contact angle analysis confirm the successful coating of fluorescent explosive-sensing composite on the surface of sand, yielding strong fluorescence and super hydrophobicity. The as-prepared "smart" sand was then applied for buried explosive detection. All buried explosives were

successfully observed by the naked eyes using a handheld UV lamp. The area and fluorescence of the quenched spots depend on the quantity and depth of the buried explosive. The emission spectra of "smart" sand inside and outside of the quenched spot also confirm both the stability of the explosive-sensitive fluorescent polymer composite and the efficiency of the detection. The as-prepared "smart" sand has shown great potential for large-scale buried explosives (e.g., landmine) detection and mapping.

Chapter 4

Electrospun Pyrene-Polyethersulfone Nanofibers Using Mixed Solvents for Sensitive and Selective Explosives Detection in Aqueous Solution

Previously we reported the use of small fluorophore such as pyrene doped in polymer as explosive sensing materials.[38,112,113] Similar research was also reported by Bayindir and co-workers, where they observed fast and sensitive detection of explosive vapors through pyrene doped polyethersulfone thin films.[46] The pyrene doped polymer films demonstrated fast and sensitive fluorescence quenching to NACs vapors. However, its application for explosive detection in aqueous solution has not been explored much. Furthermore, the quenching mechanism, whether it is static/dynamic or both, has not been fully investigated in these studies either.

Electrospinning is a well-known versatile method for generating nanofibers with a diameter in the range of 10−1000 nm.[114,115] This technique has proven to be a unique and cost-effective approach to generate nanofibrous films with high porosity and large surface area approximately 1−2 orders of magnitude more than that of the continuous thin film, [116,117] which favors the development of chemical sensors with high sensitivity and fast response.

Abstract

Fluorescent pyrene−polyethersulfone (Py−PES) nanofibers were prepared through electrospinning technique using mixed solvents. The effects of mixed solvent ratio and polymer/fluorophore concentrations on electrospun nanofiber's morphology and its

sensing performance were systematically investigated and optimized. The Py−PES nanofibers prepared under optimized conditions were further applied for highly sensitive detection of explosives, such as picric acid (PA), 2,4,6-trinitrotoluene (TNT), 2,4-dinitrotoluene (DNT), and 1,3,5-trinitroperhydro-1,3,5-triazine (RDX) in aqueous phase with limits of detection (S/N = 3) of 23, 160, 400, and 980 nM, respectively. The Stern−Volmer (S−V) plot for Py excimer fluorescence quenching by PA shows two linear regions at low (0−1 μM) and high concentration range (>1 μM) with a quenching constant of 1.263×10^6 M^{-1} and 5.08×10^4 M^{-1}, respectively. On the contrary, S−V plots for Py excimer fluorescence quenching by TNT, DNT, and RDX display an overall linearity in the entire tested concentration range. The fluorescence quenching by PA can be attributed to the fact that both photoinduced electron transfer and energy transfer are involved in the quenching process. In addition, pyrene monomer fluorescence is also quenched and exhibits different trends for different explosives. Fluorescence lifetime studies have revealed a dominant static quenching mechanism of the current fluorescent sensors for explosives in aqueous solution. Selectivity study demonstrates that common interferents have an insignificant effect on the emission intensity of the fluorescent nanofibers in aqueous phase, while reusability study indicates that the fluorescent nanofibers can be regenerated. Spiked real river water sample was also tested, and negligible matrix effect on explosives detection was observed. This research provides new insights into the development of fluorescent explosive sensor with high performance.

4.1 Experimental

4.1.1 Materials

The polymer polyethersulfone (PES, Radel, H-3000, Mw = 780 000 g/mol) was provided by Solvay Advanced Polymers. Tetrahydrofuran (THF, ≥99.0%), N,N-dimethylformamide (DMF, anhydrous, 99.8%), tetrabutylammonium hexafluorophosphate (NBu_4PF_6, 98%), 2,4-dinitrotoluene (DNT, 97%), and picric acid (PA) were purchased from Sigma-Aldrich. Pyrene (98%) was bought from Acros Organics. 2,4,6-Trinitrotoluene (TNT) was purchased from Ultra Scientific, while 1,3,5-trinitroperhydro-1,3,5-triazine (RDX) was obtained from Chem Service. All chemicals used in the experiments were of analytical reagent grade. The real water sample was obtained from a river in Willimantic, CT, USA.

4.1.2 Solution Preparation

Appropriate amounts of PES were dissolved in DMF followed by the addition of THF in order to obtain the desired concentrations in mixed DMF/THF solvents with different volume ratios (DMF/THF = 10/0, 7/3, 6/4, 5/5, 4/6, 3/7, respectively). All prepared solutions also contain 0.1 M pyrene and 2 wt % of NBu_4PF_6, endowing the fluorescence and increasing the conductivity of polymer solution, respectively, as used in our previous study.[38,113]

4.1.3 Electrospinning

The nanofibers were generated by electrospinning with a flow rate of 0.3 mL/h at an applied voltage of 25 kV over a collection distance of 10 cm. All the experiments were performed at 25 °C. The electrospun nanofibers are denoted as Py−PES nanofibers. During electrospinning process, mixed solvent (THF/DMF) evaporates, thus leaving dry Py−PES nanofibers on the collector.

4.1.4 Characterization

The viscosity of polymer solutions was measured by an AR G2 rheometer. The morphology of the fluorescent films was obtained using JEOL 6335F field emission scanning electron microscope (SEM) at an acceleration voltage of 10 kV, and the average diameter of electrospun nanofibers was measured from 50 randomly selected nanofibers in the SEM images using ImageJ software. The absorption spectra of Py−PES films were obtained using a Cary 50 UV−vis spectrophotometer (Agilent Technologies).

4.1.5 Fluorescence Quenching Experiment

The fluorescence quenching experiments were performed similar to the literature reports.[44,84] Briefly, for explosive detection in aqueous phase, the nanofibrous film on the glass slide was inserted into the cuvette with 3 mL of distilled water, and then the solution of nitro explosives or interferents were injected and allowed to reach equilibrium before recording the fluorescence signal.[35,84] In order to study the matrix effects of real water on the current film sensor performance, fluorescence quenching experiments were also conducted in a similar way except using 3 ml of real water instead of DI water. Fluorescence emission spectra were measured through a Varian Cary Eclipse fluorescence spectrometer (Agilent Technologies), and the spectra were recorded in the range of 360−600 nm with an excitation wavelength of 344 nm. The quenching efficiency is defined as $(I_0-I)/I_0$, where I_0 and I are the fluorescent intensity of the pyrene excimer peak (or monomer peak) in the absence and presence of explosives in the aqueous medium.

4.1.6 Fluorescence Lifetime Experiment

For fluorescence lifetime measurements, the nanofibrous film with different concentrations of explosives was excited with a pulse diode laser (PicoQuant) at 405 nm with a repetition rate of 2.5 MHz and a pulse width of ∼40 ps. The emission of the

samples was collected with an avalanche photodiode detector (PicoQuant) using a 450 nm long-pass spectral filter in order to study the pyrene excimer photoluminescence decay. The fluorescence decay was recorded using a time-correlated single photon counting module (Picoharp 300, PicoQuant). The measurements were conducted on at least three spots for each sample.

4.2 Results and Discussion

4.2.1 Optimization of Py−PES Nanofiber Fabrication

In this study, PES was used as the polymer matrix because of its better hydrophilicity compared with other polymers such as polystyrene used in our previous report.[38,113] For fluorescence sensing application, porous nanofibers that allow fast diffusion of analytes are highly desired. In order to prepare electrospun nanofibers, a solution with an appropriate polymer concentration or viscosity is required to obtain uniform ejection of the charged jet during electrospinning process, since extensive molecular entanglements are prerequisites for the formation of a stable and continuous charged jet. If the concentration of the solution is too low, a continuous stream of the charged jet cannot be formed, as the charged jet experiences instability leading to the formation of droplets (electrospraying). PES in pure solvent such as DMF can only be electrospun at relatively high concentration. Hsial et al. found that when PES concentration was lower than 20 wt%, its electrospinnability decreased and beads began to form.[118] In parallel, Fong et al. observed similar phenomenon and attributed the formation of beads to the low viscosity and high surface tension of the solutions.[119]

We found that electrospinning of Py−PES solution with PES concentration lower than 10% using DMF as sole solvent only resulted in the formation of Py−PES beads and

particles instead of nanofibers, possibly because of the low viscosity of the polymer solution. With the increase of PES concentration to 20%, Py−PES nanofibers with large diameter (180.5 ± 63.4 nm) formed (see Figure 4.1). However, nanofibers with large diameter are not favorable for the analyte diffusion, resulting in low sensitivity in general.

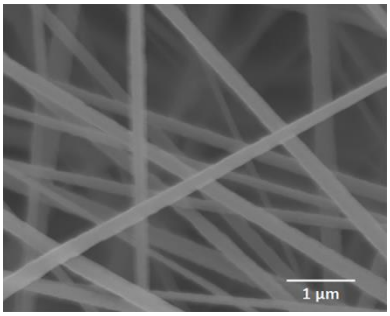

Figure 4.1 A typical SEM image of Py-PES nanofibrous film prepared through electrospinning using 20% of PES in DMF solvent.

Solvent can significantly affect the electrospinnability of a polymer solution; therefore, the selection of suitable solvents is a crucial step in a successful electrospinning process. [120,121] Mixed solvents have often been applied in the electrospinning process[122], because the introduction of non-solvent to good solvent of polymers as mixed solvents is able to control the morphology of electrospun nanofibers, at varying mixed solvent ratios.[123,124] In our case, PES can be dissolved in DMF, while it cannot be dissolved in THF. With an increase of the ratios of THF to DMF in Py−PES solution, the nanofibers can be electrospun with low probability of bead formation. Specifically, when THF was added to the Py−PES/DMF solution, the viscosity of the solution was increased. Viscosity of the polymer solution varied with the position of solvent in the given polymer solubility region because the quality of solvent−polymer interactions affects the chain geometry of the polymer. [125] Supaphol et al. observed that the addition of a cosolvent helped suppress the bead formation likely because of the increase in the viscosity and/or the conductivity of

the resulting solutions.[126] In this study, the viscosities of the as-prepared Py−PES solutions with different THF to DMF ratios were measured. To our delight, we found that viscosity indeed increased with increasing ratio of THF in solvents (see Table 4.1), which favors the electrospinning of nanofibers. In addition, it has been reported that increasing evaporation rate also promotes the formation of nanofibers during the electrospinning process. [127,128] As THF has a lower boiling point and a higher evaporation rate than that of DMF, the increase of its ratio in mixed solvents can speed up the evaporation rate during electrospinning process and thus promote the formation of nanofibrous mats.

Table 4.1 Viscosity of Py-PES solutions (6% (w/v) PES + 0.1 M Py) with different solvent ratios (DMF/THF) for electrospinning.

DMF/THF	6/4	5/5	4/6	3/7
Viscosity (Pa.s)[a]	0.038	0.053	0.069	--[b]

[a] The viscosity values were obtained at shear rate of 2.0 s^{-1}; [b] The viscosity for the solution was out of range (too high).

To obtain nanofiber sensing films with the desired morphology, the effects of different ratios of DMF/THF (10/0, 7/3, 6/4, 5/5, 4/6, 3/7) on nanofiber morphology and quenching efficiency were investigated first by fixing PES concentration and pyrene concentration at 6 w/v % and 0.1 M, respectively. With increase of THF ratio, Py−PES nanofibers were formed gradually. The SEM images of the as-prepared Py−PES nanofibers using mixed solvents (DMF/THF = 6/4, 5/5, 4/6, 3/7) are shown in Figure 4.2. The "bead-on-string" morphology can be observed for the nanofibers electrospun from mixed solvent of 60% DMF and 40% of THF (DMF/THF = 6/4). When the THF ratio is further increased, better electrospinnability can be achieved and beadless nanofibers are formed (Figure 4.2b−d). The nanofibers become more uniform with increasing THF ratio.

When DMF only or DMF/THF at a ratio of 7/3 or a higher value was used to electrospin the Py−PES solution, no nanofiber can be formed (data not shown).

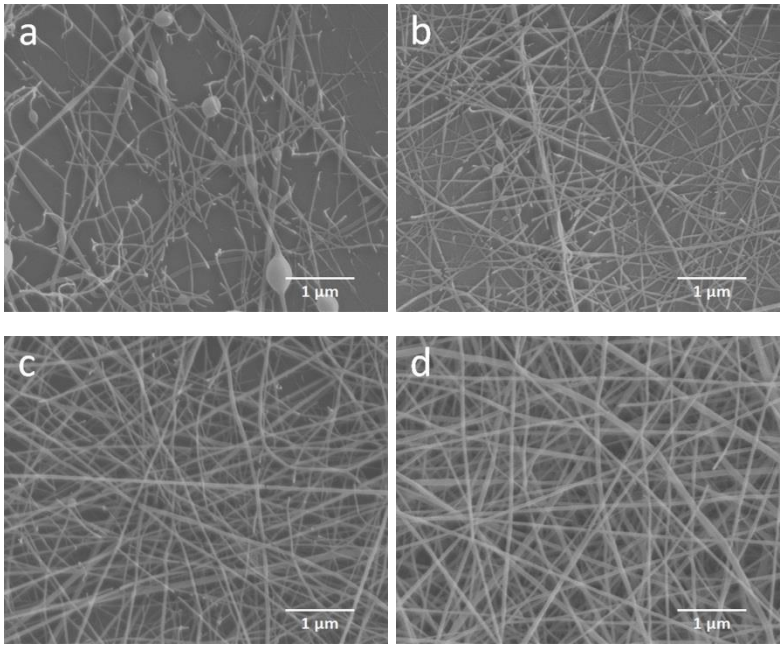

Figure 4.2 SEM images of nanofibrous film using 6% (w/v) PES + 0.1 M Py with different solvent ratios (DMF/THF): a) 6/4, b) 5/5, c) 4/6, and d) 3/7.

To investigate the effect of the mixed solvent ratio on the quenching efficiency of the sensing film upon exposure to 80 µM TNT solution, time-dependent fluorescence quenching studies were conducted on the four films prepared in Figure 4.2. The corresponding results are presented in Figure 4.3. Upon exposure to TNT solution, all the film sensors respond rapidly, which can be ascribed to the porous structure of nanofibrous film. After 6 min, the quenching efficiencies almost reach equilibrium, regardless of the ratios of DMF/THF. This result indicates that electronic structure determined by polymer/ fluorophore ratio might play a more important role in explosive-induced fluorescence quenching. Therefore, DMF/THF ratio of 4/6 was selected for subsequent experiments, as it results in the formation of nanofibers with the best morphology.

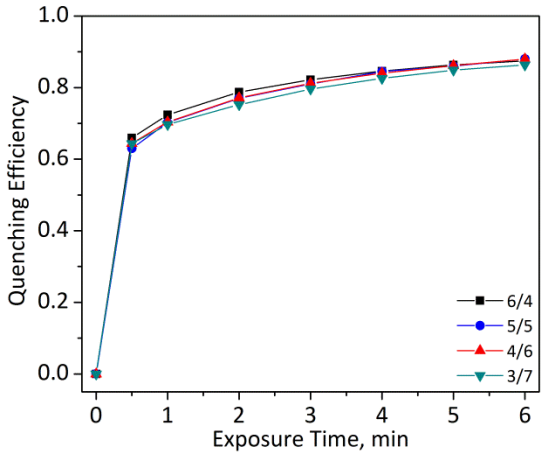

Figure 4.3 Time-dependent fluorescence quenching profiles were obtained for Py-PES nanofiber films electrospun from 6 % PES + 0.1 M Py in mixed solvents with different ratios (DMF/THF = 6/4, 5/5, 4/6, 3/7) upon exposure to 80 μM TNT solution.

In order to study the effect of PES concentration on the nanofiber morphology as well as its quenching efficiency, experiments were carried out at a fixed Py concentration of 0.1 M and DMF/THF ratio of 4/6. Figure 4.4 shows the morphology of the as-prepared Py−PES nanofibers using different PES concentrations (4, 6, and 8 w/v %). When using 2% PES, only Py−PES beads/particles were observed (data not shown), which may be due to the low viscosity of the solution. With the increase of PES concentration, the diameter of Py−PES nanofibers increases as expected. The calculated average diameters for Py−PES nanofibers using 4%, 6%, and 8% PES are 37.2 ± 12.3, 44.2 ± 15.9, and 55.5 ± 21.2 nm, respectively.

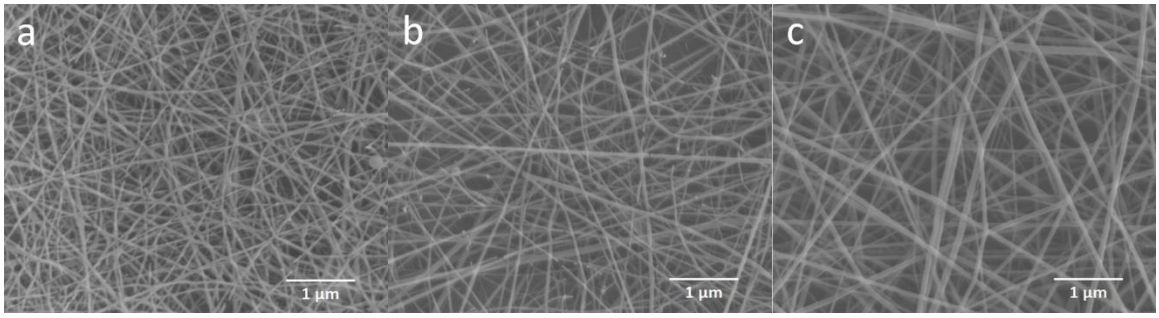

Figure 4.4 SEM images of nanofibrous films prepared using various PES concentrations at a fixed Py concentration of 0.1 M and DMF/THF ratio of 4/6: a) 4%, b) 6%, and c) 8%.

The as-prepared nanofibrous films in Figure 4.4 were also investigated for their quenching efficiency upon exposure to 80 μM TNT solution. The response of the film sensor to TNT analyte is almost instantaneous, and it takes about 6 min to reach equilibrium (Figure 4.5). One can see that the quenching efficiencies for Py−PES nanofiber films prepared with PES concentration varying from 4%, 6%, and 8% were 95%, 81%, and 38%, respectively, after a 3 min exposure to 80 μM TNT solution, showing that the 4% PES generated the best sensing film. Furthermore, pyrene concentrations also affect the quenching efficiencies to explosive detection as well as nanofiber morphology, and the results are shown in Figures 4.6 and 4.7. It was observed that at a fixed 4% PES and DMF/THF of 4/6, the nanofibrous film prepared using 0.1 M Py had the best quenching efficiency upon exposure to 80 μM TNT solution.

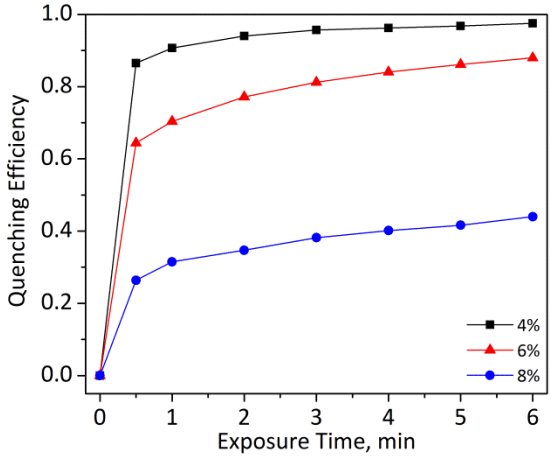

Figure 4.5 Time-dependent fluorescence quenching profiles were obtained for Py-PES nanofiber films electrospun from 0.1 M Py with different concentrations of PES dissolved in mixed solvents (DMF/THF = 4/6) upon exposure to 80 μM TNT solution.

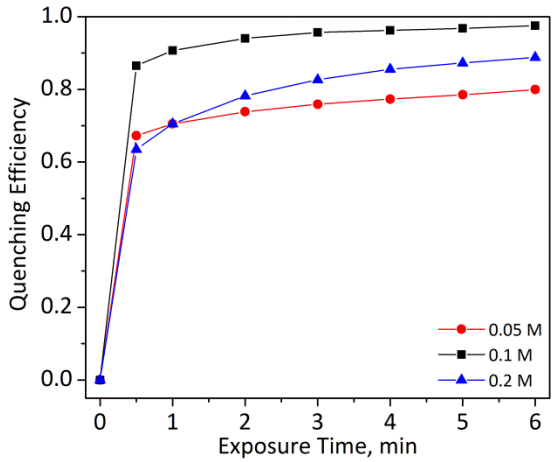

Figure 4.6 The effect of pyrene concentrations on time-dependent fluorescence quenching efficiency of Py-PES nanofibrous films prepared through electrospinning (with 4% PES in mixed solvents with DMF/THF ratio of 4/6) upon exposure to 80 μM TNT solution.

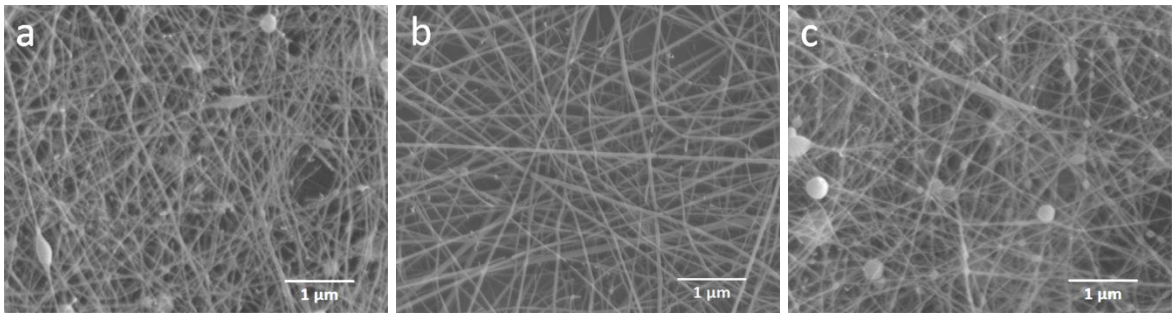

Figure 4.7 SEM images of nanofibrous films prepared using various pyrene concentrations at a fixed PES concentration of 4% and DMF/THF ratio of 4/6: a) 0.05 M, b) 0.1 M, and c) 0.2 M.

The concentrations of both polymer and the doped fluorophore impact fluorescence quenching to explosives, which may be attributed to the different electronic structures resulting from different ratios of polymer to pyrene.[112] Beyazkilic et al. have shown that the polymer acts as a geometrical barrier against the dissociation of pyrene dimers and thus greatly influences the formation of pyrene excimers.[129] It is presumably believed that a sandwich-like conformation is formed between Py and PES.[46] This conformation results from the insertion of pyrene units into and between the phenyl groups, thus forming extended conjugation of π electrons and efficient long-range energy migration. This conformation also enables effective cofacial π–π stacking and affects the formation of pyrene excimers,[112] which is corroborated by various ratios of pyrene excimer to monomer emission peak value of fluorescent film with various PES concentrations (as shown in Figure 4.8). From the above experiments, we found a solution consisting of 4% PES, and 0.1 M Py dissolved in DMF/THF mixed solvent (40% DMF and 60% THF) yielded the electrospun film with the best fluorescence quenching performance. Then it was used to prepare electrospun nanofibrous film for subsequent experiments. The absorption spectrum of the Py–PES nanofiber film was also obtained and shown in Figure 4.9. The absorption spectrum of Py–PES films shows the characteristic bands at about 327 and 343 nm, corresponding to the vibrational bands of the $S_0 \rightarrow S_2$ transition of pyrene ring, which is consistent with our previous report.[112]

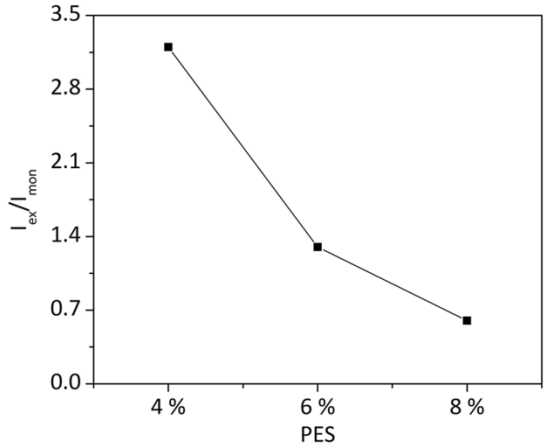

Figure 4.8 The effect of PES concentrations on pyrene excimer formation (The fluorescence ratio of the pyrene excimer (I_{ex}, at ~470 nm) to pyrene monomer emission (I_{mon}, at ~393 nm) (I_{ex}/I_{mon})) at a fixed Py concentration of 0.1 M and DMF/THF ratio of 4/6.

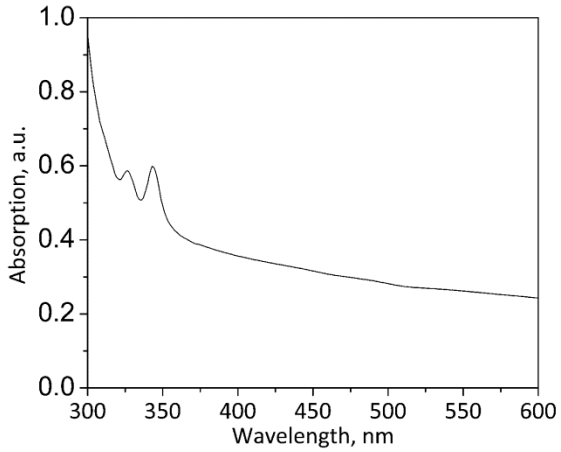

Figure 4.9 UV-vis absorption spectrum of the Py-PES fluorescent nanofibrous film using 4% PES + 0.1 M Py + 2% NBu_4PF_6 in mixed solvents with DMF/THF ratio of 4/6.

4.2.2 Nitro-explosives Detection in Aqueous Phase

Compared with most of the reported explosive sensors in aqueous applications, fluorescent film sensors are organic-solvent-free, reusable, and convenient to use, thus providing an environment- and user-friendly detection method.[35] However, fluorophore leakage could be a potential issue in the detection of explosives in solution.[129]

Therefore, the stability of pyrene entrapped in fluorescent film was investigated. In order to investigate the stability of Py-PES fluorescent film, the nanofibrous film on the glass slide was inserted into the cuvette with 3 mL of distilled water. Fluorescence emission detection was conducted for a definite period (0-48 hr), and the spectra were recorded in the range of 360-600 nm with an excitation wavelength of 344 nm. The fluorescence spectra and normalized peak intensities at ~470 nm with elapsed time are presented as Figure 4.10. Compared the peak intensities during this period, the variations are less than 8%. In addition, the spectra of the DI water before and after the fluorescent film was kept in the cuvette for 48 hrs were recorded and illustrated as Figure 4.11, suggesting that no detectable pyrene could be observed under the current condition. The results here infer that that doped pyrene is stable in PES and the potential leakage issue is negligible for the current Py−PES nanofiber-based sensors.

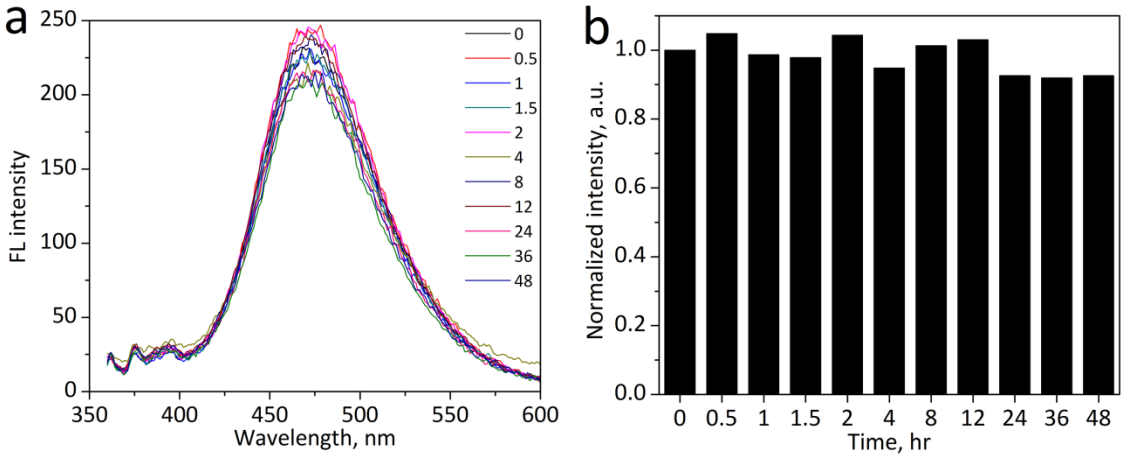

Figure 4.10 a) The fluorescent spectra of nanofibrous film in DI water with elapsed time (0-48 hr). b) The normalized intensities for pyrene excimer peak (~470 nm) with elapsed time (0-48 hr).

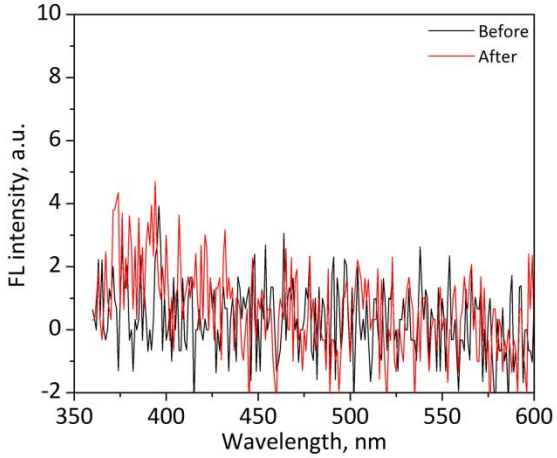

Figure 4.11 Fluorescence spectra of DI water in cuvette before and after inserting and keeping the fluorescent film in the cuvette for 48 hrs.

To explore the ability of the as-prepared fluorescent nanofibrous film in sensing trace amounts of nitro explosives, fluorescence quenching titrations were first performed with an incremental addition of TNT to the aqueous solution. Figure 4.12a shows the emission spectra of Py−PES film with incremental increasing of TNT concentrations. The fluorescence intensity progressively decreases with an increase of TNT concentrations. No new emission band was observed, even at very high TNT concentrations, indicating that no new fluorescent compound was formed during the quenching experiment. Figure 4.12b illustrates the optical images of fluorescent nanofibrous film under 254 nm UV lamp in various concentrations of TNT aqueous solutions. Under UV light, the visible blue emission of fluorescent nanofibrous film, which was inserted in a cuvette filled with water, can be observed. With increase of TNT concentrations (from left to right), the blue emission becomes significantly dimmer. The obvious fluorescence change indicates that the sensor can potentially function as a naked-eye-based portable explosive sensor for aqueous samples.

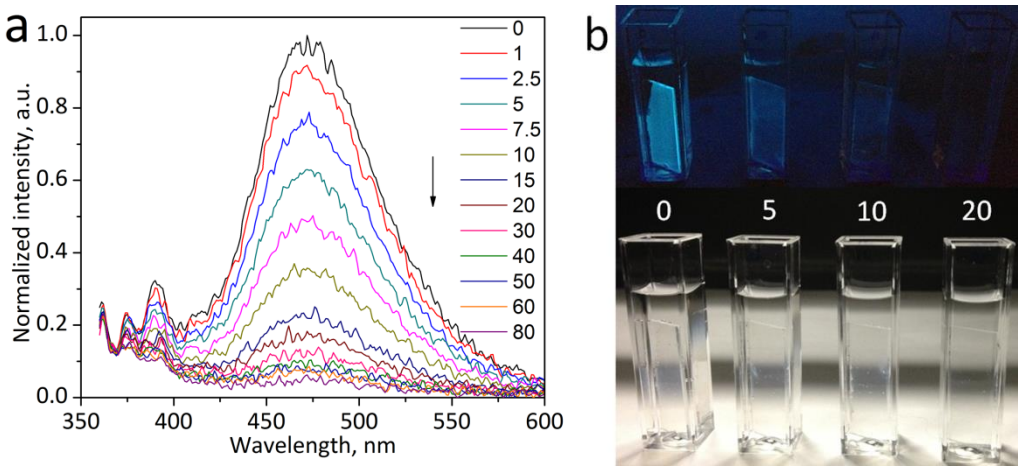

Figure 4.12 a) Concentration-dependent fluorescence quenching of Py-PES nanofiber film upon the addition of different concentrations (μM) of TNT in DI water. b) Photographs of Py-PES fluorescent nanofiber films in cuvette under UV light (254 nm, upper panel) and visible light (bottom panel) in the presence of various TNT concentrations (0, 5, 10 and 20 μM).

The fluorescence quenching titrations with other explosive analytes (e.g., PA, DNT, and RDX) were also investigated. For these nitro explosives, strong fluorescence quenching has also been observed. The quenching behavior is characterized by the normalized fluorescence intensity (I_0/I) and quenching constant (K_{SV}) using the Stern−Volmer (S−V) equation:[6]

$$I_0/I = K_{SV}[A]+1 \quad (4.1)$$

Where I_0 is the initial fluorescence intensity in the absence of analytes, I is the fluorescence intensity in the presence of explosive analytes, [A] is the molar concentration of the analytes, and K_{SV} is the quenching constant (M^{-1}). Figure 4.13 shows the plots of I_0/I for pyrene excimer peak at ~470 nm versus the concentration of various explosives (PA, TNT, DNT, and RDX).

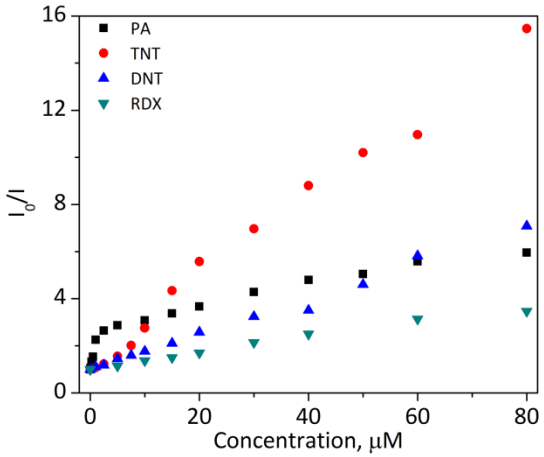

Figure 4.13 Stern-Volmer Plots (at pyrene excimer peaks of ~470 nm) for Py-PES nanofiber film sensor upon exposure to various explosives solutions.

For the four tested explosives, their Stern−Volmer plots and the calculated quenching constants are different. The Stern−Volmer plot for PA shows two linear regions at low (0−1 μM) and high concentration (>1 μM) ranges, respectively. The observed nonlinearity over the whole PA concentration range can be potentially attributed to energy transfer and/or self-absorption processes discussed in a later section.[21,130] Specifically the quenching constant for PA in the low concentration range is 1.263×10^6 M^{-1}, which is one of the highest values among the reported fluorescent PA aqueous sensors.[14,21,44,131] S−V plots for TNT, DNT, and RDX show almost linearity through the entire tested concentration range (see Table 4.2). The quenching constants are calculated to be 1.80×10^5 M^{-1}, 7.52×10^4 M^{-1}, and 3.26×10^4 M^{-1} for TNT, DNT, and RDX, respectively. These large K_{SV} values indicate that the as-prepared fluorescent nanofibrous film is sensitive to nitro explosives in aqueous solutions and the limits of detection (LOD, calculated by using signal-to-noise ratio of 3) for PA, TNT, DNT, and RDX in aqueous solution are determined to be 23, 160, 400, and 980 nM, respectively.

Table 4.2 The calculated S-V constants and fitting parameters using the quenching data at pyrene excimer peak (~470 nm) for various explosives.

Analytes	K_{SV} (M^{-1})	R^2
PA (0-1 μM)	1.263×10^6	0.991
PA (>1 μM)	5.08×10^4	0.990
TNT	1.80×10^5	0.987
DNT	7.52×10^4	0.991
RDX	3.26×10^4	0.982

Table 4.3 The LUMO and HOMO energies calculated for PES, pyrene and investigated explosive analytes.[1-3]

Compounds	LUMO (eV)	HOMO (eV)	Band gap (eV)
PES	-1.81	-4.68	2.87
Pyrene	-1.48	-5.33	3.85
PA	-3.89	-8.22	4.33
TNT	-3.48	-8.44	4.96
DNT	-2.97	-8.11	5.14
RDX	-2.53	-8.25	5.71

Pyrene monomer emission (~393 nm) was also quenched in the presence of different explosives (Figure 4.14) but with much less sensitivity. Similar observations have been reported previously.[44,64,132] The calculated quenching constants in low concentration range for the monomer peak are descending in the order of PA > DNT > TNT > RDX. The order of observed quenching efficiency is not fully consistent with the LUMO energies of these compounds and the corresponding driving forces (see Table 4.3). This indicates that photoinduced electron transfer (PET) is not the sole mechanism for the observed fluorescence quenching at monomer emission.

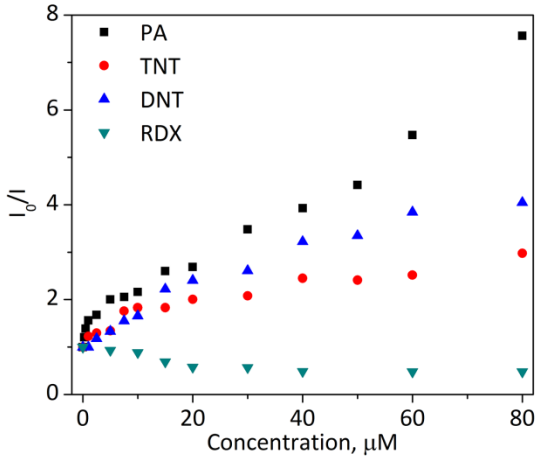

Figure 4.14 Stern-Volmer Plots (at pyrene monomer peak of ~ 393 nm) for Py-PES fluorescent nanofibers film sensor with the various nitro-based explosives.

4.2.3 Sensing Mechanism for Explosives Detection

PET plays a key role in explosive quenching process due to the electron-deficient property of explosives. When excited pyrene is exposed to nitro explosives, the excited electron is transferred from the fluorophore to the explosives. The main driving force for PET process is the difference between the conduction band of the fluorescent film and the LUMO values of explosives. The LUMO orbital energy typically indicates how easily an electron can be transferred from excited fluorophore to the electron-deficient analytes. As the LUMO orbital energies of PA, TNT, DNT, and RDX calculated by density functional theory at the B3LYP/6-31G* level are in ascending energy order (see Table 4.3), the order of the pyrene excimer quenching constant and sensitivity through pyrene excimer quenching is in accordance with the driving force for PET process.

Energy transfer may also occur between fluorophore and analyte, if the fluorophore and the analyte are close to each other and the analyte absorption band effectively overlaps with the fluorophore emission band, known as Förster resonance energy transfer (FRET). To examine whether FRET process occurs in our system and is responsible for the

different quenching efficiencies of excimer and monomer emission for various explosives, the absorption spectra of various explosives and the emission spectrum of Py−PES nanofibrous film are recorded and presented in Figure 4.15.

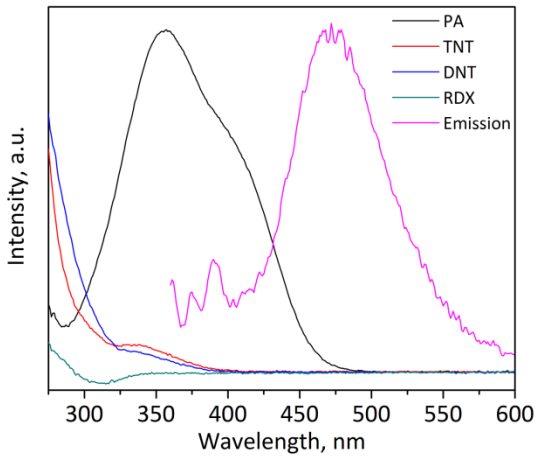

Figure 4.15 Absorption spectra of various explosive analytes and the emission spectrum of Py-PES nanofibrous film in DI water.

As shown in Figure 4.15, the Py excimer peak at ~470 nm has a small overlap with absorption of PA, but there is almost no overlap with the absorption spectra of TNT, DNT, and RDX. Therefore, both energy transfer and electron transfer mechanisms contribute to the excimer peak quenching for PA, while only electron transfer mechanism contributes to the observed quenching for other explosives. S−V plot for pyrene excimer quenching by PA shows two linear regions and bends downward at higher concentrations, which is consistent with other reports about the presence of energy transfer in fluorescence detection.[130] The observed bending downward of S−V plot might be attributed to the fact that some of the fluorophores are less accessible than others.[12] However, in the monomer peak region, there is an overlap between absorption spectrum of PA, DNT, or TNT and the emission spectrum of Py−PES nanofibers film; thus, for all these three explosive analytes, the nonlinearity of S−V plots (Figure 4.14) can be

observed and attributed to the presence of energy transfer. The overlap of analyte absorption and pyrene monomer emission was much larger for PA than for other explosives (e.g., DNT and TNT) in the range of 370−400 nm. The larger is the spectral overlap between the absorbance spectrum of the analyte and the emission spectrum of fluorescent film, the higher is the energy transfer efficiency and hence the stronger is the fluorescence quenching. This result is consistent with the observed good quenching performance for PA at both excimer and monomer peaks of pyrene. However, all tested explosives display a certain amount of absorption in the region of 300−370 nm; therefore, the effect of self-absorption on fluorescence quenching cannot be ruled out.

In order to further elucidate the detection mechanism of the present fluorescent sensors, the fluorescence lifetime of Py−PES nanofibrous film was measured. Normalized time-dependent fluorescence decay data with various concentrations of TNT are shown in Figure 4.16. The fluorescence lifetimes were calculated by fitting the time-dependent fluorescence decay data to a single-exponential decay using the equation,

$$I_{(t)} = I_{(0)} \exp\left(-\frac{t}{\tau}\right) + C \qquad (4.2)$$

where, $I_{(t)}$ is the fluorescence intensity at time (t), $I_{(0)}$ is the initial fluorescence intensity, and τ is the fluorescence lifetime. The TNT explosive concentrations only show negligible variation in fluorescence decays of the Py−PES nanofiber films (Figure 4.16), although the fluorescence intensity/yield is greatly decreased by TNT solution (Figure 4.13). The insignificant variation in the lifetimes upon addition of explosives reveals that a static quenching mechanism might be dominant where a nonfluorescent complex forms between pyrene and explosives in the ground state Py excimer. The findings herein are consistent with that of conjugated polymer sensors and assembled monolayers of small

fluorophores.[14,28,35,68] Additionally, using the S−V equation,[12,133,134] $I_0/I = k_q\tau_0[A] + 1 = K_{SV}[A] + 1$, where k_q is the bimolecular quenching constant and τ_0 is the fluorophore lifetime in the absence of quencher. k_q was calculated to be 1.03×10^{14} $M^{-1}s^{-1}$, which is much larger than the value of 10^{10} $M^{-1}s^{-1}$ for a conventional diffusion quenching process. This result further supports the claim that the static quenching process might be dominant in the Py−PES sensors.

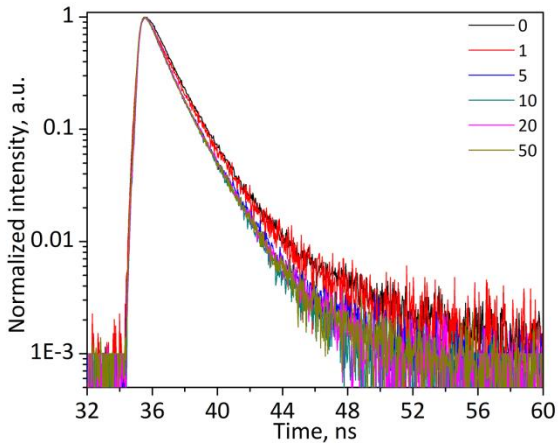

Figure 4.16 Normalized time-dependent fluorescence decay data of Py-PES film upon addition of TNT solutions in DI water at the following concentrations: 0, 1, 5, 10, 20, and 50 μM.

4.2.4 Selectivity and Reusability of the Sensor

Good selectivity and reusability are two crucial criteria for the practical use of any sensing material. To test the selectivity of the Py−PES sensor, the fluorescence intensity of electrospun Py−PES nanofibrous film exposed to various analytes at 10 μM was monitored, and the corresponding quenching efficiencies (Py excimer) are presented in Figure 4.17a. One can see that commonly used chemicals including inorganic salts, acid, alkali, metal ions, organic solvents, such as ethanol (EtOH), acetonitrile (MeCN), benzonitrile (BCN), chlorobenzene (BCl), and toluene (Tol), show insignificant effect on the measured fluorescent intensity. These results suggest that the fluorescent Py−PES

nanofibrous film is highly selective for explosives detection. Furthermore, we examined the regeneration of fluorescence signal (pyrene excimer peak) of a Py−PES film after it was quenched in 10 μM TNT aqueous solution (Figure 4.17b). In order to recover the fluorescence signal, the film was simply immersed in water and then dried in air. The rinsed film was reused to detect 10 μM TNT, and the whole process was repeated multiple times. Although the fluorescence of the sensing film cannot be fully regenerated to its original state because of incomplete removal of TNT from pyrene (caused by their strong interaction), the normalized fluorescence change is similar except for the first cycle, indicating that Py−PES film is reusable for explosive detection.

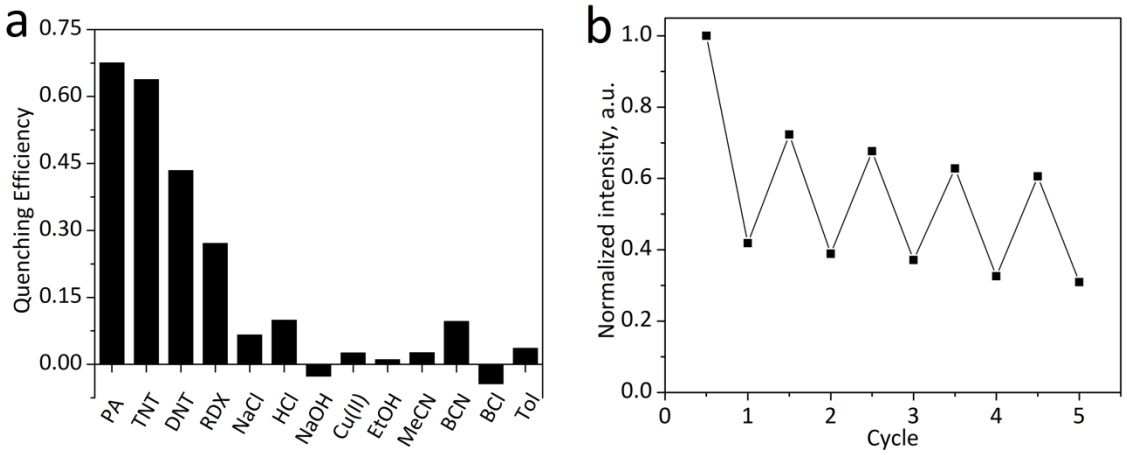

Figure 4.17 a) Quenching efficiencies (λ_{em}= ~470 nm) of Py-PES films for 10 μM of nitro-explosives and various interferents (such as ethanol (EtOH), acetonitrile (MeCN), benzonitrile (BCN), chlorobenzene (BCl) and toluene (Tol)) in DI water at room temperature; b) Reusability study for the Py-PES film, where the fluorescence intensity of the Py-PES film in DI water and TNT solution (10 μM) was recorded alternatively (λ_{em}= ~470 nm).

4.2.5 Detection of Nitro-explosives in Real Water Sample

Figure 4.18 depicts the comparison of the quenching efficiencies of various nitro explosives at 10 μM to the fluorescence emission of Py−PES nanofibrous film in DI water and in spiked real river water sample (Willimantic, CT). As expected, the quenching

efficiencies of nitro explosives in DI water and real water are nearly overlapped, and the differences are less than 7% for all the nitro explosives. One can see that the matrix effect of real river water is negligible. This result indicates that the as-prepared explosive sensing film is a good candidate for real application.

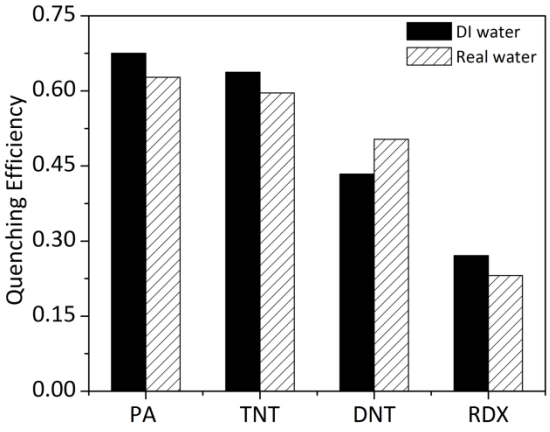

Figure 4.18 Quenching efficiencies (λ_{em}= ~470 nm) of Py-PES films for various nitro-explosives (10 μM) in DI water and real water samples.

4.3 Conclusions

Py−PES nanofibers have been electrospun using mixed solvents. Effects of the mixed solvent ratio and polymer/fluorophore concentrations on the morphology and the sensitivity of fluorescent films upon exposure to TNT solution were investigated. The Py−PES nanofibrous film, prepared under the optimum conditions and measured at pyrene excimer peak, shows good sensitivity to nitro-based explosives in aqueous phase, especially for PA with a LOD as low as 23 nM. The calculated K_{SV} values are 1.263×10^6 M^{-1} for PA (0−1μM), 1.80×10^5 M^{-1} for TNT, 7.52×10^4 M^{-1} for DNT, 3.26×10^4 M^{-1} for RDX. In addition, pyrene monomer peak was also quenched by explosives. The observed nonlinearity of the Stern−Volmer plots indicates that both energy transfer and electron transfer mechanisms are responsible for the observed fluorescence quenching.

Fluorescence lifetime measurements further reveal that the static quenching is dominant for the Py−PES nanofibrous film through formation of non-fluorescent complex between the fluorophore and electron-deficient explosives. Furthermore, common interferents have insignificant effect on the emission of the Py−PES nanofibrous film in aqueous phase, and the sensing film can be reused by simply washing with water. These features indicate that pyrene doped PES fluorescent sensors hold great promise in aqueous explosives detection due to its high sensitivity, good selectivity, cost effectiveness, and reusability.

Chapter 5

Microwave-assisted Ultrafast and Facile Synthesis of Fluorescent Carbon Nanoparticles from Single Precursor for the Detection of Picric Acid

We already investigated pyrene-doped polymer systems for nitro-explosives detection in vapor and aqueous phase as well as of buried explosives.[112,113,135] The stability and leaching issues of pyrene in Py-PES nanofiber were studied, however, the use of pyrene as a fluorophore, still potentially invokes numerous health and waste disposal hazards.[13] Therefore, in the later studies, fluorescent materials with low-toxicity were trying to develop and applied in the detection of explosives.

Recently, carbon nanoparticles (CNPs) or carbon dots (CDs) have become popular owing to their low toxicity, facile synthesis, great aqueous solubility and excellent optical properties.[136,137] A broad series of methods such as laser ablation, pyrolysis, wet oxidation, hydrothermal synthesis and electrochemical etching for obtaining carbon nanoparticles have been developed, but efficient, ultrafast and facile synthesis on a large scale with high quantum yield is still a challenge in this field.[67,138] Microwave-assisted approach offers an appealing alternative due to the low associated costs, rapid reaction rate and one-step synthesis.[139,140] Nitrogen is by far the most prominent doping candidate into carbon to obtain fluorescent CNPs. Generally, the carbon source and nitrogen source are used together in the microwave methods.[138,140,141] Although it is elegant to easily tune the nitrogen and carbon sources in the synthesis of fluorescent N-doped carbon dots (or nanoparticles), the quality control and the doping efficiency of CNPs preparation

is inevitably sacrificed due to the use of multiple components in the reaction mixture. Up to date, very few reports have been focused on the synthesis of fluorescent CNPs using a single molecule precursor through microwave conditions.

Abstract

An ultrafast and facile method for the preparation of fluorescent nitrogen-doped carbon nanoparticles (CNPs) has been developed from a single precursor (ammonium citrate dibasic serving as both carbon and nitrogen sources) under microwave conditions. The obtained CNPs showed strong blue fluorescence with a quantum yield of ~20% and displayed excitation-independent fluorescence behavior. The effects of preparation conditions on fluorescence behavior of CNPs were systematically investigated, while the as-prepared CNPs were thoroughly characterized using various advanced techniques. The mechanism of nanoparticle formation was also discussed and proposed. Furthermore, it was interestingly found that explosive picric acid (PA) could quench the fluorescence signal of CNPs significantly, while other nitroaromatic explosives have insignificant effect on the fluorescence intensity. The excellent sensing performance to picric acid could be attributed to the synergistic effect of its low molecular orbitals, the presence of fluorescence resonance energy transfer as well as acid-base interactions between picric acid and fluorescent CNPs. These findings here suggest a simple way to prepare highly fluorescent CNPs, which also holds great promise in the development of sensitive and selective sensors for PA detection.

5.1 Experimental

5.1.1 Reagents and Chemicals

Ammonium citrate dibasic (ACD, 98%), citric acid (anhydrous, 99.5%), ammonium carbonate (for analysis) were obtained from Acros Organics. Nitro based explosives such as picric acid (PA, ≥99%), 2,4-dinitrotoluene (DNT, 97%), 1,3-dinitrobenzene (DNB, ≥99%), 2,4-dinitrophenol (DNP, ≥98%), and 4-nitrophenol (4-NP, 99%) were purchased from Sigma Aldrich. 2,4,6-trinitrotoluene (TNT, 1000 μg/ml in acetonitrile) was obtained from Ultra Scientific. 2-Nitrotoluene (2-NT, ≥99.0%) was purchased from Fluka.1,3,5-trinitroperhydro-1,3,5-triazine (RDX) (1000 μg/ml in acetonitrile) was bought from Chem Service, while nitromethane (NM, >99%) was obtained from Acros Organics. Tetrabutylammonium hexafluorophosphate ($(Bu)_4NPF_6$, 98%) was purchased from Sigma Aldrich. All the other chemicals were of analytical grade. Buffer solutions with different pH were prepared using chemicals (such as citric acid, sodium phosphate dibasic, sodium phosphate monobasic, sodium carbonate and sodium bicarbonate) dissolved in DI water.

5.1.2 Synthesis of Fluorescent Carbon Nanoparticles

1.0 g of ACD was dissolved in 3.3 ml deionized water to form a homogeneous and transparent solution. The solution was then heated in a domestic 800 W oven for 40s. After that, 3 ml deionized water was added to the resultant vial in order to dissolve the solid. An aqueous solution of the CNPs was purified in a centrifuge (10,000 r/min, 20 min) to remove large or agglomerated particles.

5.1.3 Characterization

The Electrospray Ionization Mass spectrometry (ESI-MS) spectra were recorded on an AB sciex Qstar Elite spectrometer, and the carbon NPs solution was dissolved in a water/methanol (50:50 V:V) mixture (infusion rate 10 μl/min). The high resolution transmission microscope (HRTEM, JEOL JEM-2010 FasTEM) at an operating voltage of

200 kV was used to observe the morphology and microstructures of CNPs. The X-ray diffraction patterns were obtained on a Rigaku Ultima IV instrument with Cu Kα radiation operating at 40 kV and 44 mA. Fourier transform infrared (FTIR) spectra were collected on Nicolet 560 Fourier spectrometer with Diamond ATR accessory. A PHI model 590 spectrometer equipped with multiprobes (Φ Physical Electronics Industries Inc.), using a monochromatic Al Kα X-ray source (hν=1486.6 eV) was employed to collect the X-ray photoelectron spectra (XPS) of the samples. The absorption spectra were performed on a Cary 50 UV-vis spectrophotometer (Agilent Technologies). Fluorescence emission spectra and excitation spectra were measured using a Varian Cary Eclipse fluorescence spectrometer (Agilent Technologies). Electrochemical cyclic voltammetry was carried out with a CHI 601C electrochemical analyzer by using a standard three-electrode system, which consisted of platinum as the working electrode, a platinum wire as the counter electrode, and Ag/AgCl electrode as the reference electrode. CV at a potential scan rate of 50 mV/s was obtained in DMF containing 0.1 mol/l $(Bu)_4NPF_6$ with and without CNPs.

5.1.4 Quantum Yield Measurements

Quantum yield (QY) of fluorescent NPs was calculated using reference fluorophore quinine sulfate (dissolved in 0.1 mol/l H_2SO_4, QY=0.58) according to the following equation:[12]

$$QY_C=QY_R(I_C/I_R)(OD_R/OD_C)(n_C^2/n_R^2) \quad (5.1)$$

where the subscripts C and R refer to the carbon nanoparticle samples and the reference fluorophore, respectively; QY is the quantum yield; I is the integrated intensity, OD is the

optical density of the samples at the excitation wavelength, and n is refractive index of the solutions.

5.1.5 Detection of Nitro-explosives in Aqueous Phase

The sensing experiments were carried out by monitoring the fluorescence quenching behavior of carbon nanoparticles solution upon the addition of target explosives at room temperature through a fluorescence spectrometer, with the excitation and emission slit widths of 5 nm. Briefly, 3 ml of CNPs diluted solution in Na_2HPO_4-NaH_2PO_4 buffer solution (0.01 mol/l, pH=7.5) was placed in a disposal cuvette and then the target solution was added successively. Each titration was repeated at least three times and consistent results are reported.

The fluorescence emission experiments were excited at 340 nm, and the emission data were collected in the wavelength range of 345-600 nm. The quenching efficiency (QE) was calculated using the equation as follows:

$$QE = (1-I/I_0) \quad (5.2)$$

where I_0 is the initial fluorescence intensity in the absence of analyte, I is the fluorescence intensity in the presence of corresponding analyte.

5.2 Results and Discussion

5.2.1 Morphology and Composition of CNPs

The synthetic process for CNPs based on ACD occurs via hydrothermal reaction under microwave conditions for 40s. ACD is condensed and intermolecularly dehydrated to form oligomers when the reaction temperature is relatively low. Further increasing the temperature produces a burst of high concentration of nucleation, which grows uniformly and is further carbonized to form CNPs. The molecular weights of CNPs were obtained

through mass spectrometry as shown in Figure 5.1. The results suggest that a low-molecular-weight oligomer-like compound is formed because of polymerization of ACD through microwave conditions.

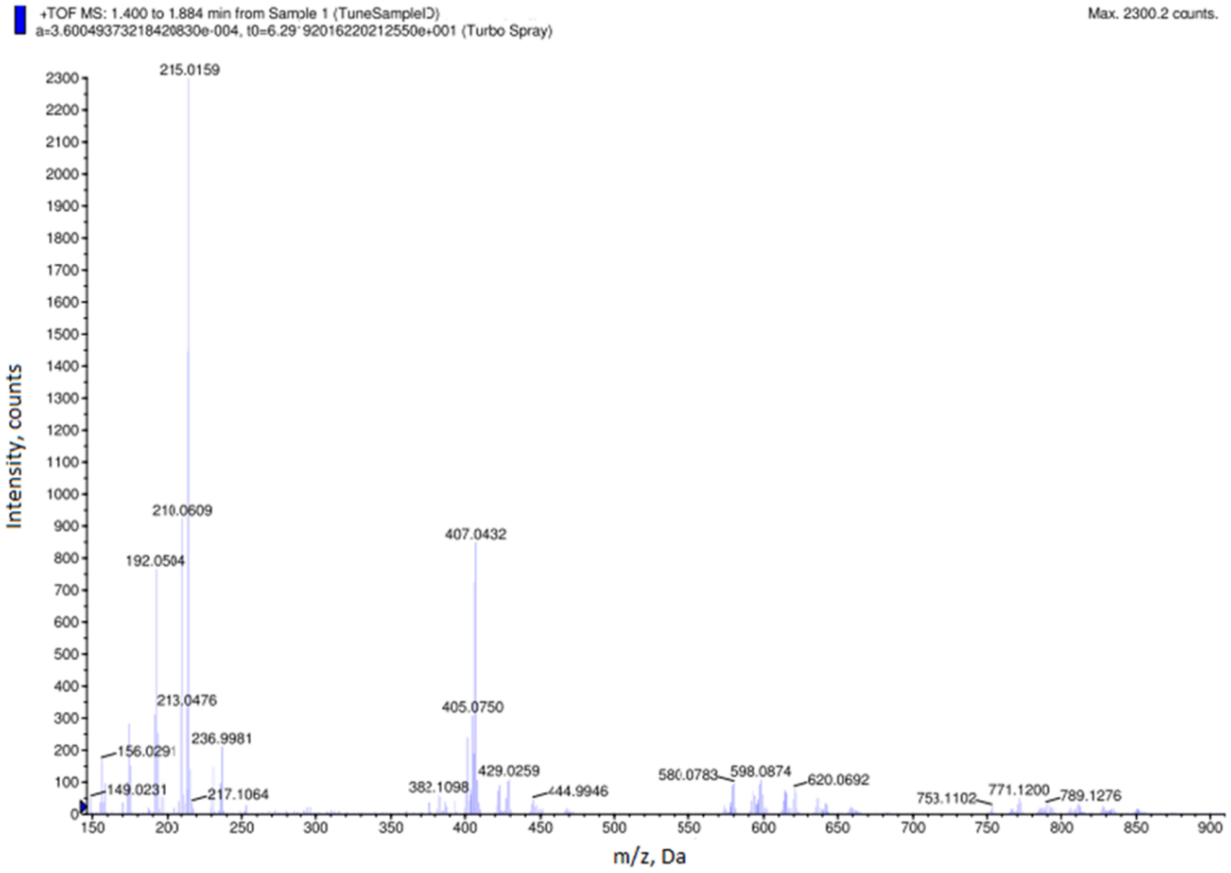

Figure 5.1 ESI-MS spectrum of CNPs.

The TEM results illustrate that these CNPs were well-dispersed (Figure 5.2A), with diameter in the range of 5.5±1.5 nm. The size distribution of nanoparticles is shown in Figure 5.2B. From the HRTEM image, some nanoparticles were observed to be amorphous[137], while a few particles possessed well-resolved lattice fringes (inset of Figure 5.2A), with the lattice spacing of 0.25 nm and 0.36 nm, which correspond to highly disordered of carbon atoms[142,143]. The diffractogram of the nanoparticles (in Figure

5.2C) shows two peaks at around 17.3^{o} and 34.2^{o}, which are assigned to 5.12 Å and 2.62 Å. The similar XRD patterns have also been reported by other researchers[142-144], suggesting that the as-synthesized nanoparticles adopt a more amorphous structure. The results demonstrate distinct features from that of high crystallinity of ammonium citrate dibasic (data not shown). No obvious D or G bands were detected in the Raman spectrum of CNPs, possibly due to low carbon-lattice-structure content.[137] In addition, the unsuccessful attempts to record Raman spectra even using lasers with various wavelengths (such as 514, 633 and 785 nm) exclude the possible fluorescence effect on the Raman spectra. The structure and composition of carbon nanoparticles could be detected by FTIR spectroscopy. Figure 5.2D shows FTIR results of carbon nanoparticles. Several peaks are present such as 1715 cm^{-1}, 1635cm^{-1}, 1364 cm^{-1}, which correspond to the C=O bond. In addition, the IR absorption bands at 1570, 1293, 1233 and 1203 cm^{-1} are assigned to N-H group, C-N of aromatic amines, C-O carboxylic group, and C-N aliphatic amines. The presence of these functional groups on the surface of nanoparticles endows the hydrophilicity and stability in aqueous conditions.

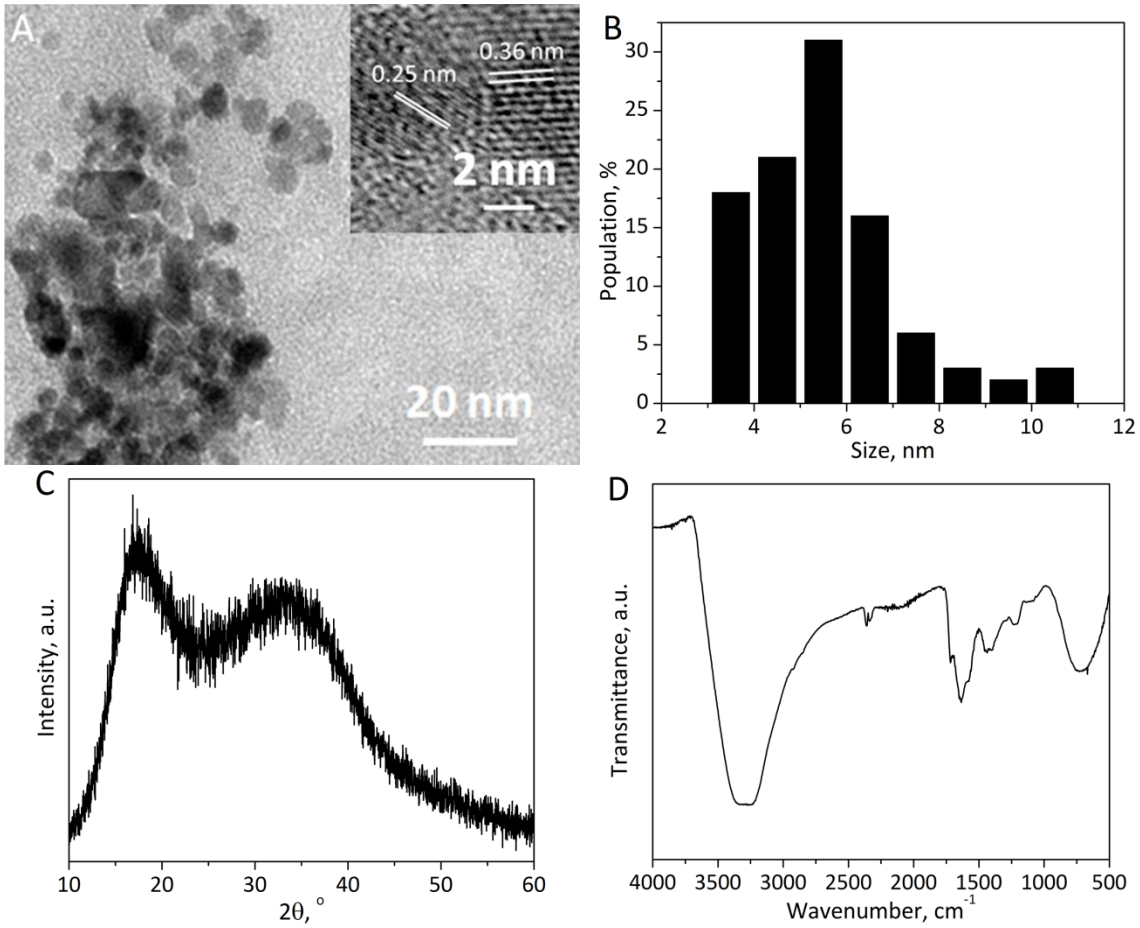

Figure 5.2 (A) TEM graphs of carbon nanoparticles, inset shows HR-TEM of carbon nanoparticles. (B) Size distribution of CNPs from TEM graph. (C) XRD patterns of carbon nanoparticles; (D) FTIR spectrum of fluorescent carbon nanoparticles (CNPs).

Moreover, surface elements and groups were also investigated by XPS analysis (as illustrated in Figure 5.3). The XPS survey spectrum for the CNPs shown in Figure 5.3A indicates that the CNPs are mainly composed of carbon, nitrogen and oxygen. The high resolution of spectrum of C1s exhibits 4 main peaks (Figure 5.3B). The binding energy peaks at 284.6 eV, 285.4 eV, 286.9 eV, and 288.7 eV could be assigned to carbon in the form of C-C, C-N, C=O, and O-C=O respectively.[145,146] The N1s spectrum (Figure 5.3C) reveals the presence of C_3-N (graphite like, 401.9 eV), C-N-C (pyridinic-like and pyrrolic-like, 400.4 eV) and N-H (399.4 eV) groups, respectively.[53,147] This verifies that the synthesized CNPs are nitrogen-doped CNPs. The O1s XPS spectrum (Figure 5.3D)

could be decomposed into peaks at 531.1eV, 532.2 eV and 533.4 eV, indicating the presence of –OH, *O=C-O, C-O, and O=C-O*.[147]

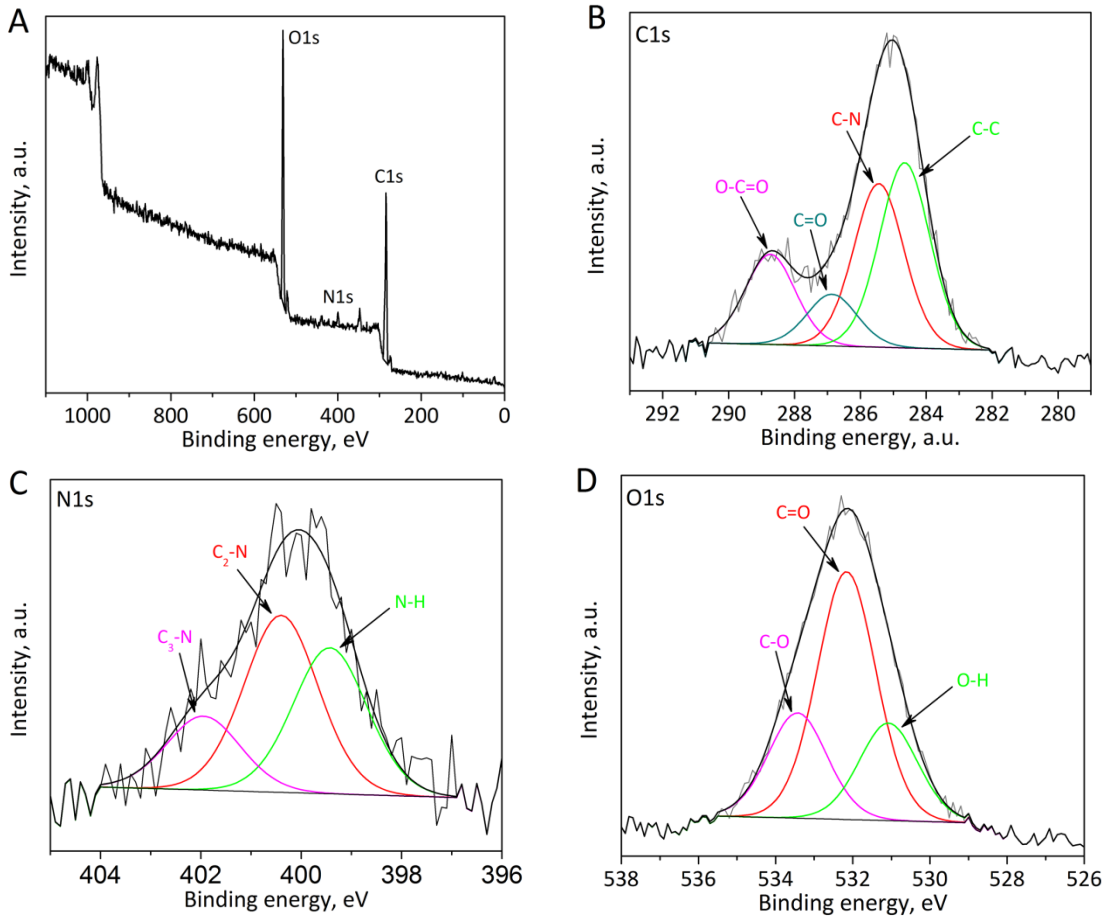

Figure 5.3 XPS spectra of CNPs. (A) XPS survey spectrum; (B) High resolution of C1s; (C) High resolution of N1s; (D) High resolution of O1s.

5.2.2 Optical Properties of CNPs

Figure 5.4A shows the absorption, excitation and emission spectra of carbon nanoparticles. A large absorption peak at 330 nm and a tiny peak at 244 nm could be observed. The two peaks represent an aromatic π system, π-π* transition of the C=C bond and n-π* transition of C=O bond respectively.[145,146] We also observed two peaks in excitation spectrum (with emission wavelength of 435 nm) of carbon nanoparticles locating at 342 nm and 239 nm, implying that more than one kind of excitation energy

trapped on the surface of the carbon nanoparticles.[148] The emission spectrum of carbon nanoparticles with excitation of 340 nm is also presented in Figure 5.4A, an emission peak at 435 nm is observed, inferring the formation of blue emission of carbon nanoparticles. The insets of Figure 5.4A illustrate graphs of CNPs solution under visible light and 365 nm UV light, under which the CNPs solution showed pale yellow and blue emission color, respectively.

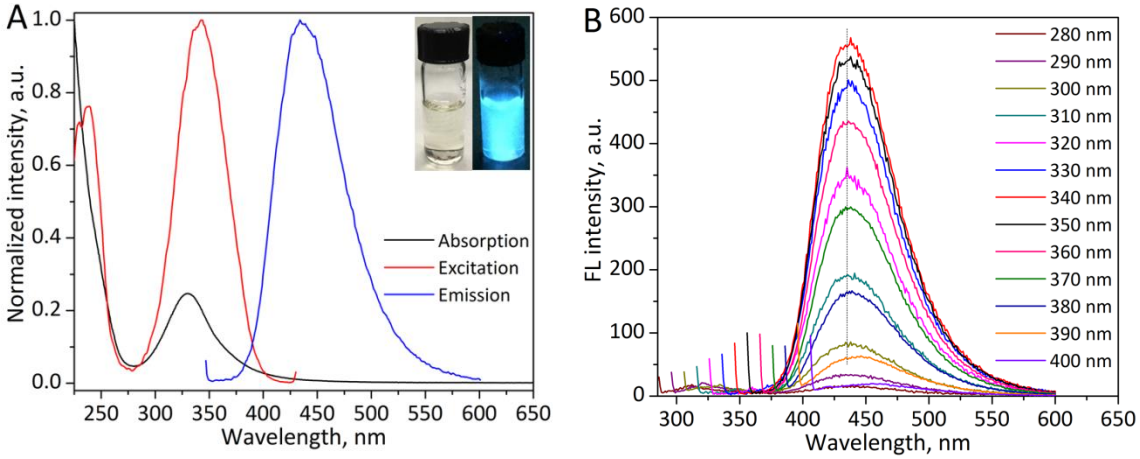

Figure 5.4 (A) Normalized UV-vis absorption, excitation and emission spectra of carbon nanoparticles diluted in DI water. Insets show the graphs of NPs solution under visible and UV light. (B) Emission spectra of a dilute aqueous solution of carbon nanoparticles at various excitation wavelengths in the range of 280 – 400 nm.

Figure 5.4B illustrates the detailed emission spectra with various excitation wavelengths. When excitation wavelength is changed from 280 to 400 nm, no obvious shift was observed for the fluorescence emission peaks, which center at ~435 nm. The excitation-independent behaviour is due to less surface defects and more uniform of carbon nanoparticles.[145] Furthermore, we note that excitation wavelength above 400 nm induces very little emission. The fluorescence QY is one of the most important properties for fluorescent materials. The fluorescence quantum yield was calculated to be about 19.8%, which is higher than or comparable to previous carbon nanoparticles reports.[138,145,149]

The emission intensity of carbon nanoparticles diluted in various pH buffer solutions was investigated, and the results are depicted in Figure 5.5A. Under low pH range (2-6), the fluorescence intensity increases with increasing of pH; further increasing pH (6-10) nearly stabilizes nanoparticle emission. When pH of the solution is higher than 10, the fluorescence intensity decreases gradually with increasing of pH. The pH dependent properties could be utilized in pH sensing applications. The properties may be attributed to aggregation of the as-synthesized CNPs by their surrounding carboxyl acids at lower pH, leading to the fluorescence quenching.[145] Protonation-deprotonation of amides group on the nanoparticle surface is possible another reason for the pH dependent fluorescence properties.[136] In addition, the stability of carbon nanoparticles in the presence of various concentrations of NaCl was investigated (Figure 5.5B). The fluorescence intensity remains almost unchanged from 0 to 2 M NaCl solution, revealing the potential application in high ionic conditions such as brackish water or ocean water.

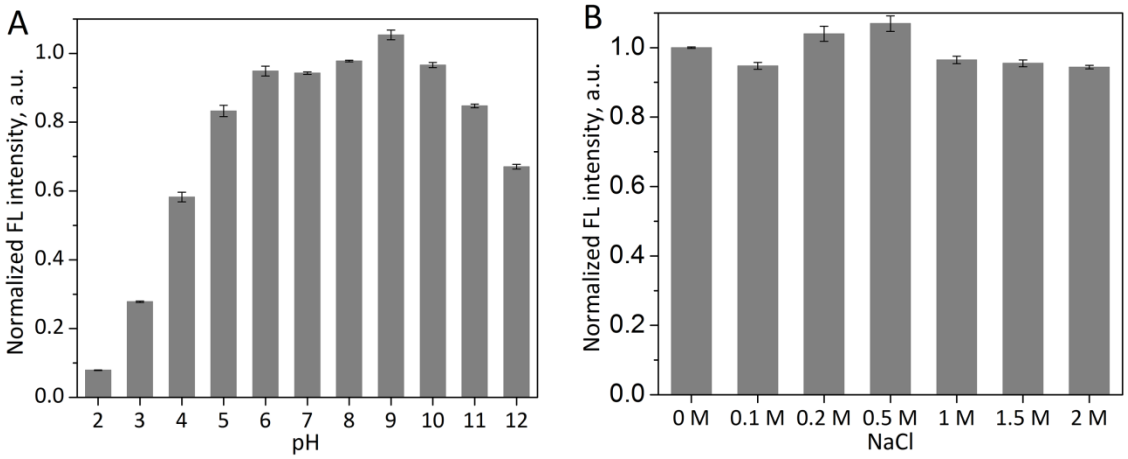

Figure 5.5 (A) pH and (B) salt effect on fluorescence intensity of diluted carbon nanoparticles in aqueous solutions.

5.2.3 Synthesis of Fluorescent Carbon Nanoparticles

To probe the mechanism of nanoparticles synthesis, CNPs were prepared with different microwave reaction times (30s, 35s, 40s, and 45s), while the color shows colorless to

yellow, brown and dark brown solid, respectively. The differences of nanoparticles were firstly characterized by absorption spectroscopy as illustrated in Figure 5.6A.

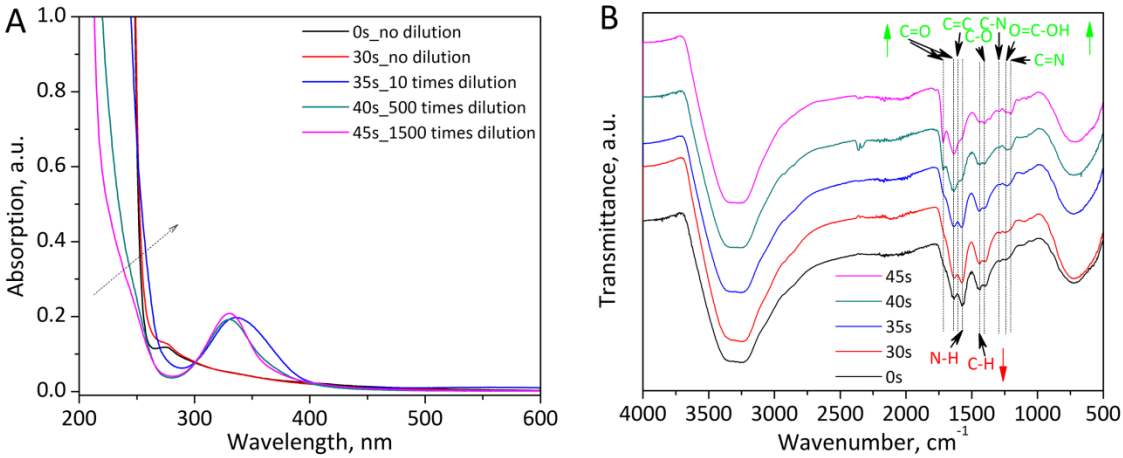

Figure 5.6 (A) UV-vis absorption spectra of diluted CNP solutions obtained by tuning the microwave reaction time. (B) FTIR spectra of CNPs prepared through different reaction time.

Comparing with UV-vis spectrum of ACD (0s), with increasing of reaction time, one obvious broad peak at ~330 nm gradually appears. For the solution of 30s, the absorption spectrum changes a little compared with that of ACD, and almost no peak at ~330 nm could be observed, suggesting little fluorescence formation, which is also verified by the weak emission under UV light and the corresponding low quantum yield in Table 5.1. For the UV-vis absorption spectra of ACD (0s) and the CNPs for 30–45s (diluted through different times), the peak at 330 nm (π-π^* transition of the C=C bond, surface/molecule center) and the peak at 244 nm (n-π^* transition of C=O bond, carbonic core center) enhance simultaneously with reaction time, indicating the enhancement of synergistic effects between the surface/molecule state and carbon core and its contribution to PL intensity. The greatly increasing of absorption implies that the reaction yield of carbon nanoparticles increases with prolonging of the microwave reaction. The reaction yield of carbon nanoparticles increases greatly, also verifying by the color changes.

In addition, the FTIR spectra of ACD control (0s) and carbon nanoparticles solution with various reaction times are shown in Figure 5.6B. With prolonging of the microwave reaction, several functional groups gradually increases such as C=O ketone, C-N, C=N, carboxylic groups, and several functional groups gradually decreases such as C-H, and N-H groups, inferring that new products are formed during the reaction.

For fluorescent CNPs synthesized by various reaction times, it is found that the quantum yields are different as shown in Table 5.1. In the first period under microwave reaction (0s–30s), the fluorescence quantum yield changes a little, due to the short reaction time, low temperature, and limited formation of the fluorescent NPs. With the prolonging of reaction time, the quantum yield increases greatly (30s–35s), but further increasing reaction time decreases the quantum yield. This finding is similar to the temperature effect on the formation of nanoparticles.[136] Long reaction time results in the too high reaction temperature, thus leading to the formation of a large amount of fluorophores as building blocks of the carbogenic domains, and decreasing the quantum yield simultaneously. Trading-off the reaction yield and fluorescence quantum yield of the CNPs, the reaction time of 40s was used in this study if without notification.

Table 5.1 Fluorescence quantum yield of carbon nanoparticle solutions in water

Reaction time, s	30	35	40	45
QY	0.043	0.281	0.198	0.137

It is believed that the fluorescent nanoparticles are formed due to polymerization of the precursor ammonium citrate dibasic followed by partial carbonization of the resulting polymer.[145] ACD is condensed and intermolecularly dehydrated to form oligomers when the reaction temperature is relatively low. Further increasing the temperature produces a burst of high concentration of nucleation, which grows uniformly and is further

carbonized to form noncrystalline CNPs with hydrophilic functional groups.[136,144,150] Both the ammounium and citrate groups in ACD affect the formation of fluorescent carbon nanoparticles. Control experiments with similar conditions, using citric acid and ammonium carbonate respectively were conducted, and after microwave heating we observed little fluorescence under UV lamp.

5.2.4 Sensitive and Selective Detection of Picric Acid

Due to their unique fluorescence and water solubility, fluorescent carbon nanoparticles have found wide applications not only for chemical sensing, but also biosensing.[151] Only a few cases of CNPs for nitroaromatic explosives detection have been reported. Sun's research exhibited non-selectivity towards a specific nitroaromatic in organic solvent through photoinduced electron transfer.[152] The selective detection of picric acid through carbon dots was investigated by Wu and co-workers in a later study.[42] However, both of the reports for nitro-explosives demonstrated poor sensitivity, and the sensing mechanisms to nitro-explosives detection through this kind of carbon dots have remained elusive.

The diluted as-synthesized CNPs (~0.1mg/ml) were used for nitro-explosives sensing. As shown in Figure 5.7A, with incremental addition of picric acid in the range of 0.5-100 μM to carbon NPs solutions in phosphate buffer (0.01 M, pH=7.5), the fluorescence intensity is gradually quenched. A detection limit was calculated to be 0.25 μM (by using 3σ/k, σ is standard deviation and k is the slope). Furthermore, the quenching results could be quantitatively analyzed with Stern-Volmer (S-V) equation,

$$I_0/I = K_{SV}[A]+1 \quad (5.3)$$

where I_0 is the initial fluorescence intensity in the absence of analytes, I is the fluorescence intensity in the presence of analytes, [A] is the molar concentration of analytes, and K_{SV} is the quenching constant in M^{-1}.

The intensities for CNPs emission peak at ~435 nm were plotted versus the concentration of various analytes and are shown in Figure 5.7B. We can see that picric acid shows an exponential S-V curve. From the inset of Figure 5.7B, a linear curve at lower concentrations (0-20 μM) could be observed. But for higher concentrations, it deviates from linearity and increases exponentially. The similar phenomenon has also been reported by various researchers.[22,153,154] This nonlinearity of the S-V plot for picric acid is possibly due to self-absorption, or a combination of static quenching and dynamic quenching.[21,71,130] This kind of nonlinear plot for picric acid also suggests an effective fluorescence energy transfer mechanism present in the quenching process. In order to fit the nonlinear S-V curve, an exponential quenching equation is applied,

$$I_0/I = a \exp(k[A])+b \qquad (5.4)$$

where a, b and k are constants. The result shows that the plot can be fitted to $I_0/I=1.50 \exp(0.0212[A])–0.49$ perfectly, and the correlation coefficient (R^2) reaches 0.9997 as displayed in Figure 5.7B. The quenching constant value for picric acid was calculated to be 3.18×10^4 M^{-1}, using the product of constants a and k.[153,154]

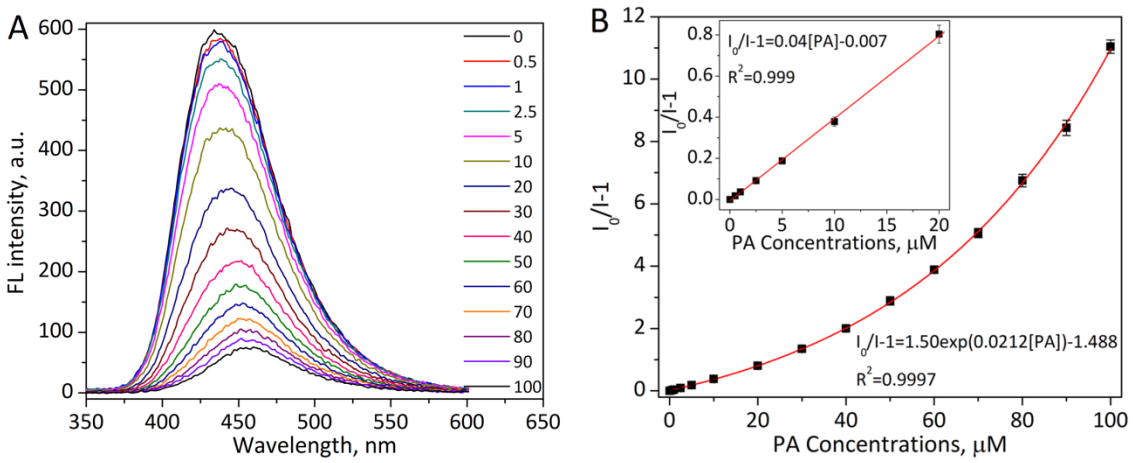

Figure 5.7 (A) Fluorescence spectra of carbon nanoparticles upon addition of various PA concentrations in water. (B) Fitting curve of the nonlinear Stern-Volmer plot for PA by exponential quenching equation, Inset shows the fitting curve of the linearity of Stern-Volmer plot for PA of 0-20 μM.

To check the selectivity of fluorescent CNPs toward picric acid, fluorescence quenching titrations were conducted with other nitro explosives such as TNT, DNT, 2-NT, DNB, RDX and NM. One can see from Figure 5.8A that the fluorescence quenching efficiency for 50 μM PA is about 75%, while the same concentration of all the other analytes only quenches less than 9%. These results reveal that the carbon nanoparticles are much more sensitive to picric acid than to the other nitro compounds. The intensities for CNPs emission peak at ~435 nm were plotted versus the concentration of various analytes and are shown in Figure 5.8B. The quenching constant values for various nitro-explosive analytes are also shown in Table 5.2, and the quenching constant for PA is about 20 times larger than for other nitro-explosives, indicating very predominant selectivity of picric acid over others nitro-compounds.

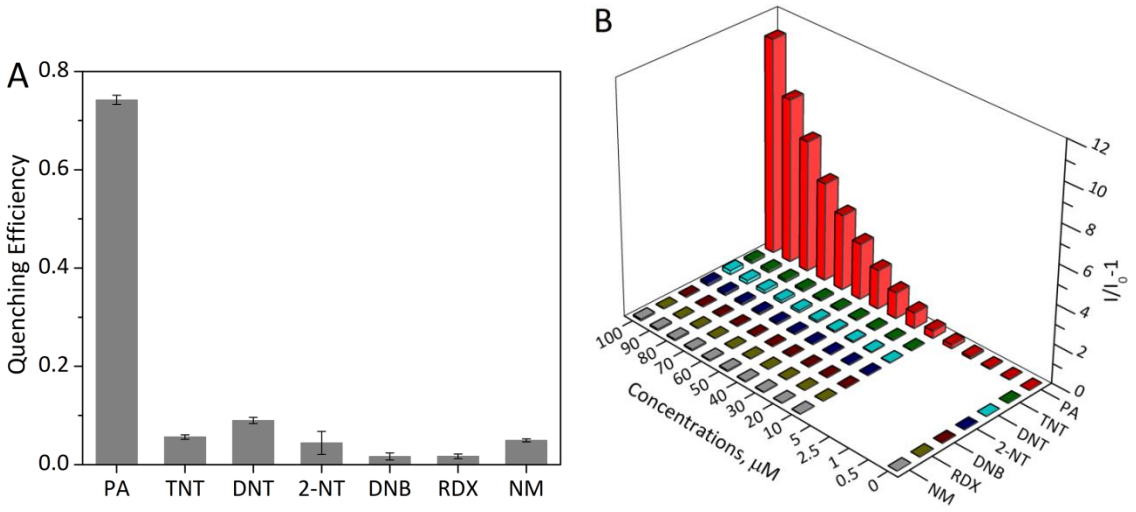

Figure 5.8 (A) Fluorescence quenching efficiency obtained for carbon nanoparticle sensors upon addition of 50 μM of different nitro-explosives, indicating excellent selectivity for picric acid. (B) Stern-Volmer plots of carbon nanoparticle sensors with different nitro-based explosives.

Table 5.2 Fluorescence quenching constant K_{SV} values for the various explosive analytes ([a] implying that K_{SV} constant for PA was obtained in the linear range of 0-20 μM, [b] implying that quenching constant was obtained from exponential fitting, and / implying that the values of K_{SV} constant were less than 800 M^{-1}).

Analytes	K_{SV} (M^{-1})
PA	4.01×10^{4} [a]
	3.18×10^{4} [b]
TNT	1.34×10^{3}
DNT	1.99×10^{3}
2-NT	1.25×10^{3}
DNB	/
RDX	/
NM	/

5.2.5 Sensing Mechanism for Picric Acid Detection

In order to understand the origin of the high sensitivity and selectivity of fluorescent carbon nanoparticles towards picric acid, the mechanism of quenching was investigated. Generally, photoinduced electron transfer (PET) plays a pivotal role in explosive quenching because of the electron-deficient nature of explosives.[21,30,112] During the PET process, the excited-state of fluorophore is likely to donate an electron to the ground-state of explosive compounds (as shown in Figure 5.9), and leading to fluorescence quenching. The energy gap between the lowest unoccupied molecular orbital (LUMO) of donor fluorophore and that of the acceptor explosive is approximately the PET driving force.

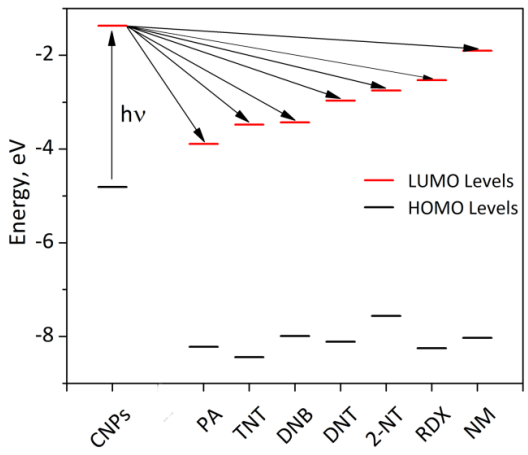

Figure 5.9 Illustration of PET mechanism between CNPs and explosive analytes and the corresponding energy profile diagram (LUMO and HOMO levels).

The molecular orbitals of carbon nanoparticles were obtained through absorption spectra and cyclic voltammetry.[112,137] UV-vis spectra was used to obtain the band gap (E_g) of carbon nanoparticles[112], and the value of the direct optical band gap was determined by the extrapolation of the linear region to zero absorption (Eq. 5.5), and the extrapolating graph is illustrated in Figure 5.10.

$$Ah\nu = (h\nu - E_g)^{1/2} \quad (5.5)$$

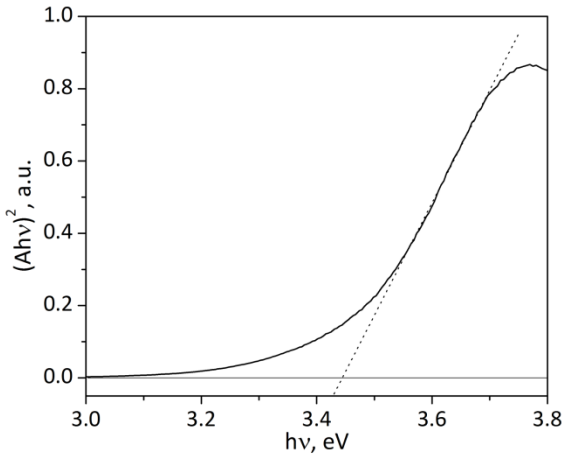

Figure 5.10 $(Ah\nu)^2$ versus the photon energy hν. The extrapolation of the linear region to zero absorption allows us to determine the gap energy of CNPs (the data from Figure 5.4A).

The HOMO and LUMO energy levels could be estimated through onset potentials of cyclic voltammetry.[112,137] The onset potential of oxidation of CNPs from CV is shown in Figure 5.11. The relationship between the onset potential of oxidation (E_{ox}') and HOMO energy levels can be expressed as the following equation:

$$E_{HOMO} = -(E_{ox}' + 4.4)\ eV \quad (5.6)$$

The LUMO energy levels of NPs could be obtained by adding the HOMO energy levels and band gap as follows:

$$E_{LUMO} = E_{HOMO} + E_g \quad (5.7)$$

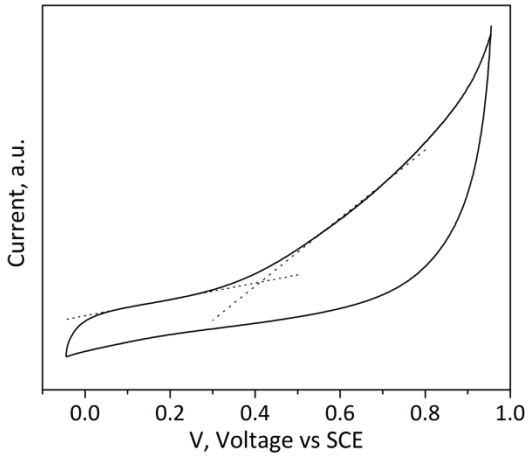

Figure 5.11 Cyclic voltammograms of fluorescent carbon nanoparticles in DMF with 0.1 M of $(Bu)_4NPF_6$.

We have also obtained the corresponding HOMO - LUMO energy levels for the acceptor explosives.[130] The molecular orbitals and the corresponding increasing order of LUMO levels for niro-explosives are illustrated in Figure 5.9. Expectedly, the driving force for picric acid is largest due to its lowest LUMO value during all the investigated analytes. However, the order of fluorescence quenching is not in complete accordance with LUMO energy sequences. The finding here indicates that PET is not the only mechanism for the observed fluorescence quenching.

As mentioned previously, the non-linearity of the S-V plot for PA suggests that energy transfer mechanism is possibly present in the quenching process. According to FRET theory[12,135], the rate of energy transfer depends on the relative orientation of the donor and acceptor dipoles, the extent of overlap of fluorescence emission spectrum of the donor (the fluorophore) and absorption spectrum of the acceptor (the analyte), and the distance between the donor and the acceptor. The probability of resonance energy transfer depends upon the extent of overlap between these molecules. Absorption spectra of various explosive analytes and the emission spectrum of carbon nanoparitcles are depicted in

Figure 5.12, and it can be observed that absorption spectrum of picric acid largely overlap with emission spectrum of carbon nanoparticles, while there is almost no overlap for other analytes. The integral of overlap J expresses the degree of spectral overlap between the donor emission and the acceptor absorption, and represents the extent of energy transfer. J (M^{-1} cm^{-1} nm^4) is given by[12]:

$$J = \frac{\int_0^\infty F(\lambda)\varepsilon(\lambda)\lambda^4 d\lambda}{\int_0^\infty F(\lambda)d\lambda} \quad (5.8)$$

where $F(\lambda)$ is the corrected fluorescence intensity of the donor in the wavelength λ to $\lambda+\Delta\lambda$, $\varepsilon(\lambda)$ is the extinction coefficient of the acceptor at λ in M^{-1} cm^{-1}. The overlap value as high as 7.36×10^{13} M^{-1} cm^{-1} nm^4 for picric acid was obtained, which is about two orders of magnitude larger than those of other analytes as shown in Table 5.3. Therefore, the various overlap values demonstrate the different probability of resonance energy transfer and confirm the high sensitivity and selectivity of fluorescent carbon nanoparticle sensors to picric acid.

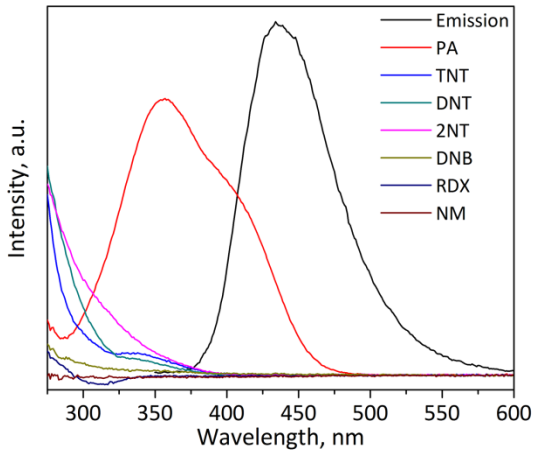

Figure 5.12 Absorption spectra of various explosive analytes and the emission spectrum of carbon nanoparitcles in aqueous solution.

Table 5.3 Degree of spectra overlap integral J values for the various explosive analytes

Analytes	J(λ) (M^{-1} cm^{-1} nm^4)
PA	7.36×10^{13}
TNT	5.21×10^{11}
DNT	1.76×10^{11}
2-NT	6.56×10^{11}
DNB	1.17×10^{12}
RDX	6.98×10^{11}
NM	5.65×10^{11}

Furthermore, carbon nanoparticles have unsaturated pyridine nitrogen and amine groups on the surface; so, to trace the presence of explosives, electrostatic interactions may lead to the special selectivity of fluorescent CNPs for picric acid. In the aqueous solution, PA acts as a strong protonic acid due to the bonding of three electron-withdrawing nitro groups on the benzene ring, and it easily forms a charged anion. In contrast, carbon nanoparticles possess abundant nitrogen atoms on the surface. Through IR studies, we observed C-N groups and N-H groups on the surface. Further XPS studies demonstrate that there are pyridinic-N, pyrrolic-like N and amine groups on the surface of carbon nanoparticles. It has been reported that pyridinic nitrogen or amine groups could effectively bind to PA by the acid-base pairing interactions, thus leading to fluorescence quenching of carbon nanoparticles.[21,130,155] In order to verify that the acid-base interactions affect the quenching process, fluorescence quenching experiments using various nitrophenols with different acidity were conducted. As shown in Figure 5.13, the quenching efficiencies follow the order PA>DNP>4-NP, which is in complete agreement with the order of acidity of these analysts, where the pKa values of the quenchers are 0.38 for PA, 4.89 for DNP, 7.15 for 4-NP.

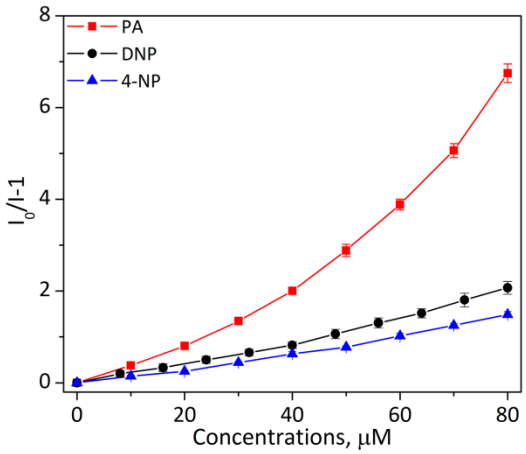

Figure 5.13 Stern-Volmer plots of carbon nanoparticles with picric acid and other nitrophenols in aqueous solutions.

In addition, compared with their corresponding structure-similar nitro compounds (such as TNT, DNT and DNB), the quenching efficiencies for PA and DNP are much higher, and the finding here indicates the effect of the hydroxyl group and the acidity on the fluorescence quenching. Besides, an obvious red shift (in Figure 5.7A) in the emission maxima upon the addition of picric acid also suggests the molecular interactions during the sensing process.[55,156] This feature when coupled with the molecular orbitals and magnitudes of the overall integrals may explain the molecular basis of current fluorescent sensor for the high sensitivity and selectivity to PA, as other nitro compounds do not have a hydroxyl group and so they cannot interact efficiently with carbon nanoparticles and result in a very low quenching efficiency.

5.3 Conclusions

In summary, we have synthesized fluorescent carbon nanoparticles using a single precursor through a microwave-assisted, facile and ultrafast method. The results from various characterization methods suggested the formation of fluorescent nitrogen-doped carbon nanoparticles. The fluorescent nanoparticles exhibited pH-dependent, excitation

wavelength-independent properties, and high stability in high salt solutions. In addition, the mechanism of carbon nanoparticles formation was investigated through tuning the microwave reaction time, which affects the CNPs absorption, IR spectra and fluorescence quantum yields. The fluorescent titrations have displayed that fluorescence quenching of CNPs were sensitive and efficient for picric acid detection with a quenching constant of 3.18×10^{4} M^{-1} and a limit of detection of 0.25 μM. The nanoparticles also revealed high selectivity to PA over a number of other explosives interferents such as TNT, DNT, 2-NT, DNB, RDX and NM in aqueous solution. The excellent quenching performance to picric acid could be attributed to the synergistic effect of photo-induced electron transfer, fluorescence resonance energy transfer and strong electrostatic interaction between the carbon nanoparticles and picric acid. The findings here suggest a simple way to prepare highly fluorescent CNPs, which also hold great promise in the development of sensitive and selective sensors for PA detection.

Chapter 6

Carbon Dots Co-doped with Nitrogen and Phosphorus for High Quantum Yield, Dual Fluorescence Emission and Nitro-explosives Detection

Obtaining fluorescence emission with different colors has been considered as a key requirement for successfully utilizing carbon dots (CDs or carbon nanoparticles) in various applications.[157] So far most of carbon dots emit blue color under ultraviolet excitation. Although the excitation-dependent fluorescence emission has been reported, a significant decrease in fluorescent intensity was also observed with changing of excitation wavelength.[136,137,158] Researchers are trying to develop synthetic methods to shift the maximum emission light from blue, to green, yellow, and red. These synthesis endured issues such as complex procedures, toxic components or low quantum yield.[138,157,159-162] It is still difficult to synthesize CDs through a facile strategy with different fluorescence emission and high quantum yield in one single material.

The emission of CDs could be tuned by controlling the dehydration reaction, chemical manipulation, doping of other elements.[67,146,157] Nitrogen is by far the most prominent doping candidate into carbon to obtain fluorescent CDs. Co-doping the carbon materials with nitrogen and other heteroatoms such as boron (B), and sulfur (S) has also been reported.[146,163-165] As far as we are aware, however, the co-doping of Nitrogen (N) and Phosphorus (P) in carbon nanoparticles to improve the fluorescent properties has not been exploited.

Abstract

In this work, we report a novel CDs with high quantum yield and dual fluorescence emission. The CDs were synthesized using nitrogen and phosphorous co-doped carbon sources through one simple and fast microwave-assisted method. The as-synthesized nitrogen and phosphorus co-doped CDs (N, P-CDs) were thoroughly characterized using various characterization techniques such as TEM, XRD, FTIR, XPS, etc. The optical results suggest that more than one type of excitation energy trapped on the surface of CDs and the CDs demonstrated excitation-dependent and pH-independent emission properties. Especially, under different excitation wavelengths, the CDs showed blue and green emission, the quantum yields of which were 0.51 and 0.38, respectively. The nitro-explosives detection through the quenching of different emission were investigated, in which picric acid quenched both blue and green emission, while TNT only quenched green emission to some extent. We expect that the nanoparticles provide new insights into the development of a ratiometric sensor to various targets because of their dual fluorescence emission.

6.1 Experimental

6.1.1 Reagents and Chemicals

m-Phenylenediamine (mPDA, >99%) was purchased from Acros Organics, Ethylenediamine (EDA, Sigma Ultra) was obtained from Sigma Aldrich. *o*-Phosphoric acid (85%, ACS certified) was bought from Fisher Scientific. Picric acid (≥99%) was purchased from Sigma Aldrich, while 2,4,6-trinitrotoluene (TNT, 1000 μg/ml in acetonitrile) was obtained from Ultra Scientific. All the other chemicals were of analytical grade. Buffer solution (pH=7.50) was prepared using sodium phosphate dibasic and sodium phosphate monobasic.

6.1.2 Synthesis of Fluorescent N, P-CDs

0.5 g of mPDA was dissolved in 2 ml deionized water, and then 1 ml of phosphoric acid and 0.5 ml EDA were added into the prepared solution subsequently to form a homogeneous and transparent solution. The solution was then heated in a domestic 800 W oven for 40s (Caution: Please do not overheat the solution to avoid potential explosion). After that, 3 ml deionized water was added to the resultant vial in order to dissolve the solid. An aqueous solution of the CDs was purified in a centrifuge (10,000 rpm/min, 20 min) to remove large or agglomerated particles. Buffer solutions with different pH were prepared using chemicals (such as sulphuric acid, citric acid, sodium phosphate dibasic, sodium phosphate monobasic, sodium carbonate, sodium bicarbonate and sodium hydroxide) dissolved in DI water.

6.1.3 Characterization

The high resolution transmission electron microscope (HRTEM, JEOL JEM-2010 FasTEM) at an operating voltage of 200 kV was used to observe the morphology and microstructures of CDs. The X-ray diffraction (XRD) patterns were obtained on a Bruker D2 Phaser X-ray diffractometer with Cu Kα radiation and operating at 30 kV and 10 mA. Fourier transform infrared (FTIR) spectra were collected on Nicolet 560 Fourier spectrometer with Diamond ATR accessory. In order to collect the X-ray photoelectron spectra (XPS) of the samples, a PHI model 590 spectrometer equipped with multiprobes (Φ Physical Electronics Industries Inc.), using a monochromatic Al Kα X-ray source (hν=1486.6 eV) was employed. The absorption spectra were performed on a Cary 50 UV-vis spectrophotometer (Agilent Technologies). Fluorescence emission spectra

and excitation spectra were measured using a Varian Cary Eclipse fluorescence spectrometer (Agilent Technologies).

6.1.4 Quantum Yield Measurements

Quantum yield (QY) of fluorescent CDs was calculated using standard reference fluorophore quinine sulphate (dissolved in 0.1 mol/l H_2SO_4, excited at 350 nm, QY=0.58) and fluorescein (dissolved in 0.1 mol/l NaOH, excited at 440 nm, QY=0.95) according to the following equation:[12]

$$QY_C=QY_R(I_C/I_R)(OD_R/OD_C)(n_C^2/n_R^2) \quad (6.1)$$

where the subscripts C and R refer to the carbon nanoparticle samples and the standard reference fluorophore, respectively; QY is the quantum yield; I is the integrated intensity, OD is the optical density of the samples at the excitation wavelength, and n is refractive index of the solutions.

6.1.5 Detection of Nitro-explosives

The sensing experiments were carried out by monitoring the fluorescence quenching behavior of carbon dots solution upon the addition of target explosives at room temperature through a fluorescence spectrometer, with the excitation and emission slit widths of 5 nm. Briefly, 3 ml of the diluted CDs solution in buffer solution (0.01 mol/l, pH=7.5) was placed in a disposal cuvette and then the target analyte was added successively. The fluorescence emission experiments were excited at 350 nm and 440 nm, while the emission data were collected in the wavelength range of 360–650 nm and 450–650 nm, respectively.

6.2 Results and Discussion

6.2.1 Materials Characterization

The obtained CDs solution exhibits a long-term homogeneous phase without any noticeable precipitation at room temperature. The transmission electron microscopy (TEM) image (Figure 6.1A) shows the size of the as-prepared CDs, and the diameters of nanoparitcles are 8.1±2.7 nm. Also in the TEM image, a few large nanoparticles are observed with the diameters of larger than 15 nm. Due to the presence of carbon on TEM grid, the morphology of carbon nanoparticles is not very clear, especially for completely amorphous carbon nanoparticles. After a careful analysis, the size distribution of the prepared CDs were obtained and are shown as Figure 6.1B. High-resolution TEM (HRTEM) images suggest that the as-prepared CDs have complicated structures. Some nanoparticles demonstrate completely amorphous structures, while as shown in Figure 6.1C-E, some carbon nanocrystals are also observed with lattice spacings of 0.24 nm, 0.35 nm, and 0.51 nm, respectively, revealing the crystallinity of some CDs. The lattice spacings agree well with interspacing of the (100), (220) and (002) planes of carbon materials.

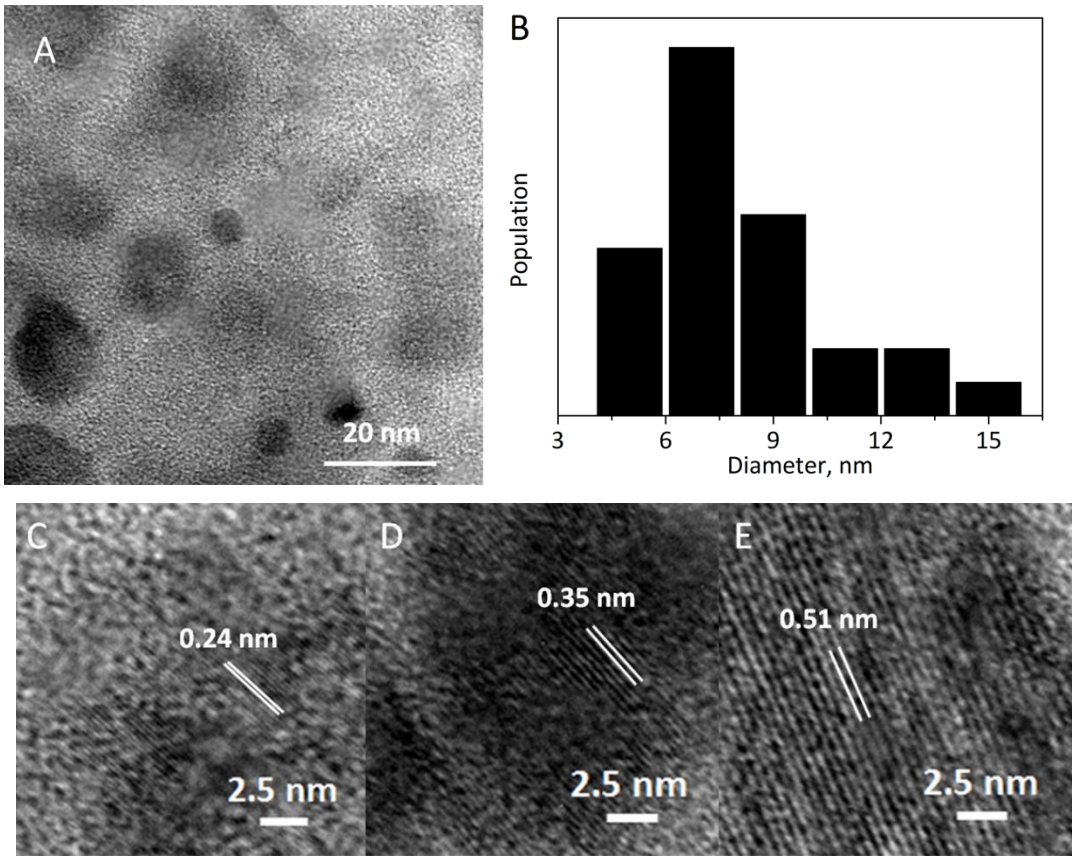

Figure 6.1 (A) TEM graph of the synthesized N, P-CDs, (B) Size distribution diagram. (C-E) HRTEM images and lattice structures of N, P-CDs.

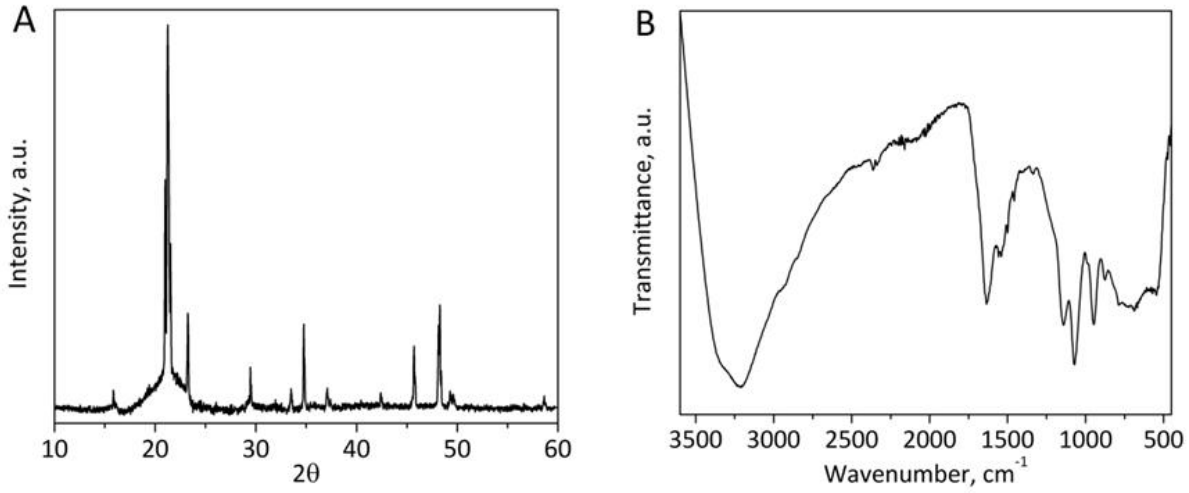

Figure 6.2 (A) XRD patterns and (B) FTIR spectrum of N, P-CDs.

The XRD patterns (Figure 6.2A) of the carbon dots show several crystal peaks such as ~15.8^{o}, ~23.2^{o}, ~34.7^{o}, corresponding to d lattice spacings of 5.16 Å, 3.83 Å and 2.58 Å, which are consistent very well with the d lattice spacing obtained from HRTEM graphs in Figure 6.1C-E. The XRD patterns of CDs are similar to that of carbon materials. IR spectroscopy is a powerful technique to characterise the surface functionality of the nanoparticles, and the results are shown as Figure 6.2B. The presence of absorption band at 687 cm^{-1} and 785 cm^{-1} are assigned to aromatic sp^2 C-H bending from mPDA. The absorption band at 1541 cm^{-1} is related to the plane blending vibration and the stretching vibration of N-H from EDA or mPDA. In the spectrum of carbon dots, these groups are maintained. In addition, the strong absorption bands of the aniline-phosphoric acid systems observed in the range of 850–1200 cm^{-1} are assigned to phosphate group and protonated -NH- groups, suggesting the formation of aniline-phosphoric acid salt.[166] The appearance of 944 cm^{-1} and 878 cm^{-1} assigned to vibration of P=O phosphate group, suggests the presence of phosphoric acid. As reported, the presence of phosphate group is crucial for stacking and stabilization of carbon nanoparticles during the polymerization process.[166] There are new peaks appearing in CDs compared with raw materials. For example, absorption bands at 543 cm^{-1} emerge, which reflects the deformation vibration in plane of secondary amines -NH-; and the new appeared band at 1634 cm^{-1} are attributed to C-X (X=C, N, or O) stretching vibration, while a new appeared peak at 1142 cm^{-1} in CDs are possibly assigned to the vibration of the -NH^{+}= structure, or stretching of P-O, P=O or P=N groups. The results here suggest a new product is formed after microwave heating.

In order to further characterize the newly formed N, P-CDs, XPS was employed. The XPS survey spectrum for the CDs shown in Figure 6.3A indicates that the CNPs are mainly composed of carbon, oxygen, nitrogen and phosphorus. The CDs compositions are obtained, showing that there are 66.6%, 27.8%, 3.3% and 2.3% for carbon, oxygen, nitrogen and phosphorous, respectively. O1s XPS spectrum (Figure 6.3B) could be deconvoluted into four peaks, at 529.9 eV (C=O), 531.2 eV (P=O), 532.4 eV (-O-) and 533.8 eV (COO and H_2O).[167] The N1s spectrum (Figure 6.3C) reveals the presence of C_3-N (graphite like, 403.3 eV), C-N-C (pyridinic-like and pyrrolic-like, 400.7 eV) and N-H (398.5 eV) groups, respectively. The P2p XPS spectrum (Figure 6.3D) shows two decomposed peaks at 132.1 eV and 133.2 eV, which can be assigned to P-C and P-O groups through charge-transfer interaction of P with conjugated aromatic C rings. The results here indicate the successful co-doping of nitrogen and phosphorus into the carbon materials.

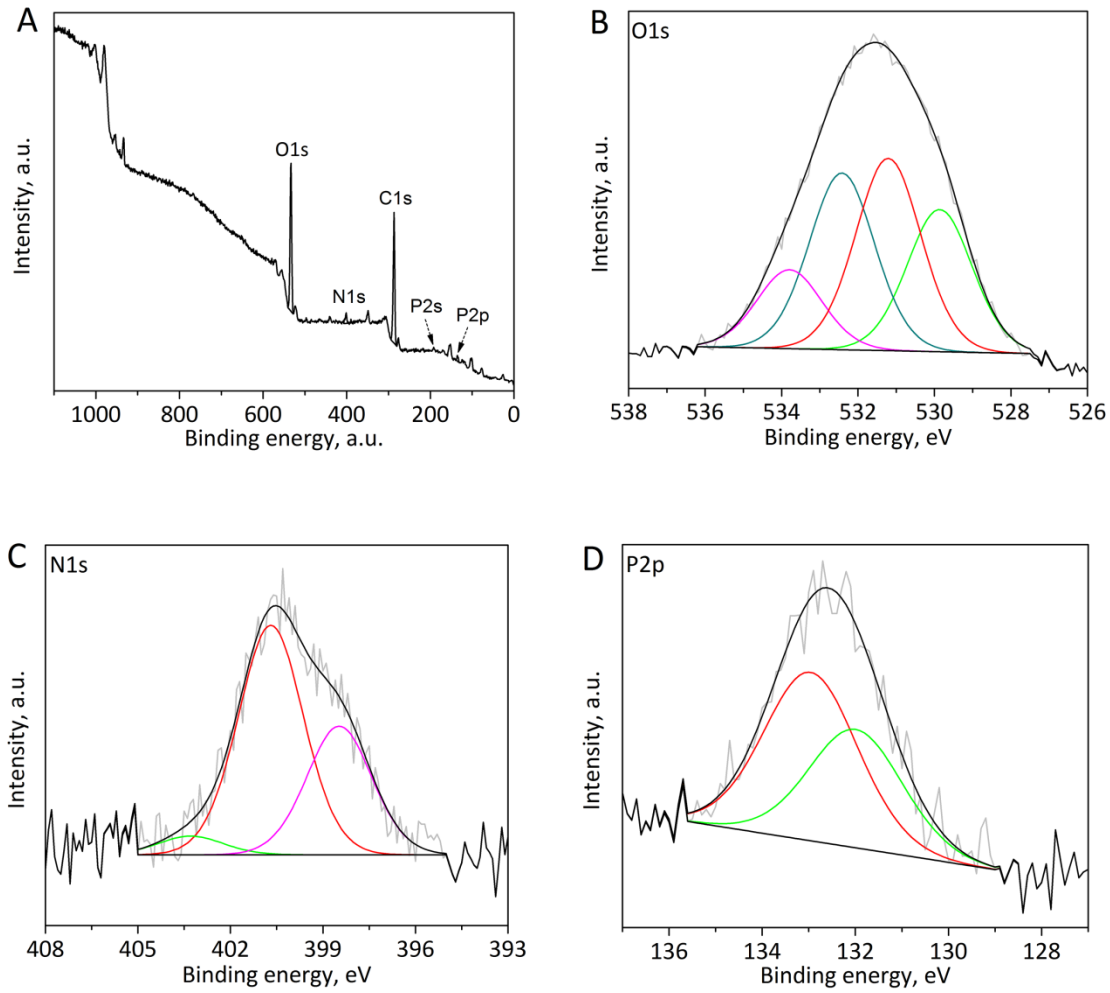

Figure 6.3 XPS spectra of CDs. (A) XPS survey spectrum; (B) High resolution of O1s; (C) High resolution of N1s; (D) High resolution of P2p.

mPDA is a derivative of aniline. Therefore, the polymerization can be occurred through solubilisation of aniline (mPDA) in aqueous solution containing phosphoric acid and EDA as a result of the formation of soluble anilinium salt (aniline-phosphoric acid) via an acid-base interaction.[166] The microwave conditions sped up polymerization to form polyaniline fluorescent CDs. The protonation of polyaniline was achieved by the presence of phosphoric acid. Especially phosphate groups can interact with several polyaniline

chains to form a cross-linked network structure and the excess of phosphoric acid remains after polymerization.

6.2.2 Optical Properties

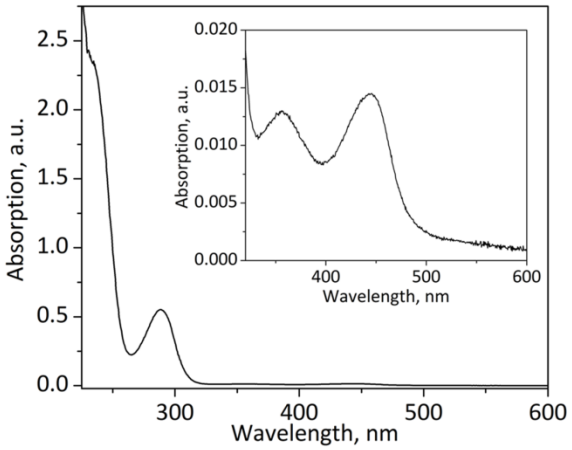

Figure 6.4 UV-vis absorption of CDs, the subset shows the UV-vis absorption in the range of 320-600 nm of CDs.

For the diluted carbon dots solution, one large peak at 288 nm is observed (Figure 6.4), which is attributed to the π-π* transition of aromatic C=C phenyl group. Although the intensities are much lower, the other two peaks centered at 355 nm and 444 nm are also oberved (inset of Figure 6.4), due to the aromatic structures with extended conjugation or possibly formed polyaninline in the acidic condition[168].

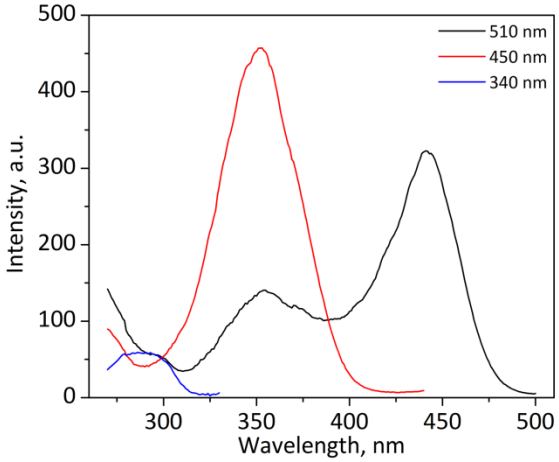

Figure 6.5 Excitation spectra of CDs with various emission wavelengths.

The excitation spectra of carbon dots are shown in Figure 6.5. It is observed that different excitation spectra are observed with various emission wavelengths (such as 510 nm, 450 nm and 340 nm). With the emission wavelength of 510 nm, two obvious excitation peaks at about 354 nm and 441 nm are clearly seen. When the emission wavelength is changed to 450 nm, one large excitation peak of 352 nm is observed. With the emission of 340 nm, one broad excitation peak at ~290 nm could be noticed. The three excitation peaks appeared under different emission wavelengths are in agreement with the absorption peaks. The results here infer that more than one kind of excitation energy is entrapped on the surface of nanoparticles.

When the excitation wavelengths are chosen from 290–500 nm, the emission spectra are shown in Figure 6.6A. When the excitation wavelength is no more than 300 nm, the energy is even strong enough to excite three types chromophores (emission peaks at about 340 nm, 450 nm and 500 nm) for emission. With the increasing of the excitation wavelengths (320–370 nm), the energy decreases, and only one blue emission peak (~450 nm) is observed. Further increasing the excitation wavelengths (380, 390 nm) excites both blue and green emission. While at even higher excitation wavelengths (400–470 nm), only one green emission peak (centered at about 510 nm) is observed. Finally, it is worth noting that excitation with wavelengths above 480 nm significantly reduces the fluorescent intensity and fails to induce fluorescence emission. The results here suggest the excitation dependent properties as-synthesized CDs.

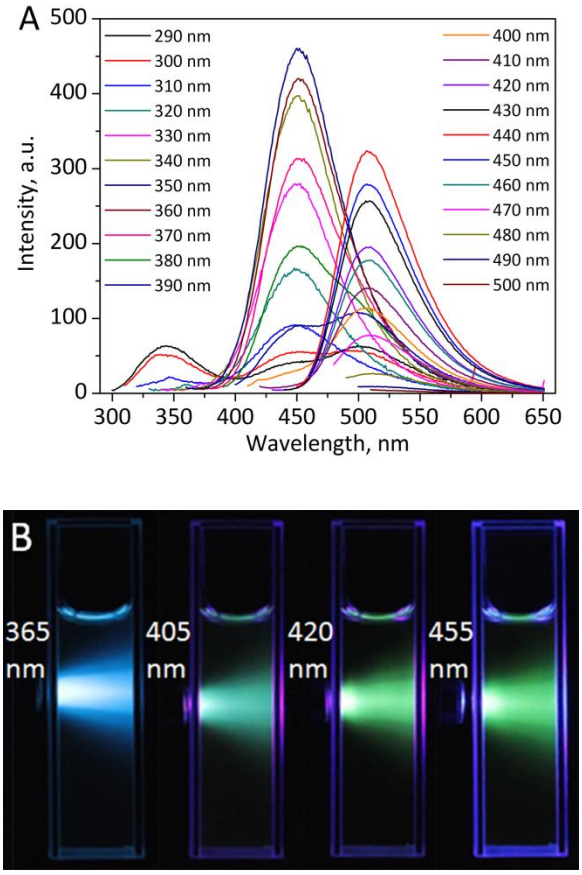

Figure 6.6 (A) Emission spectra of N, P-CDs with various excitation wavelengths, showing the excitation dependent properties. (B) Photographs of diluted CDs solutions in quartz cuvette with different excitation wavelengths (left to right: 365 nm, 405 nm, 420 nm, and 455nm) using LED light, show the emission colors of blue, cyan, green and green, respectively.

In addition, we find that the as-synthesized CDs solutions may show dual emission visible colors (blue and green), which differentiates obviously from traditional blue light emitting CDs. In Figure 6.6A, upon excitation at 350 nm, one strong emission peak centers at about 450 nm (blue); while one emission peak at about 510 nm (green) is observed with excitation of 440 nm. In order to verify their excitation dependent properties and dual fluorescence emission of the CDs, the photos with fluorescence emission colors were recorded under different excitation light (LED with various wavelengths). Figure 6.6B shows the emission colors of diluted CDs solution in quartz cuvette with various

excitation wavelengths (365 nm, 405 nm, 420 nm and 455 nm), consequently various colors (blue, cyan, green and green) are clearly observed.

The quantum yield is of great importance for the application of fluorescent materials. It is noted that most of reported CDs remained low in quantum yield especially for the green fluorescence carbon dots, which is usually no more than 10%. The strongest green fluorescence emission is observed centered at 510 nm under 440 nm excitation with a high quantum yield of 0.38; while the strongest blue fluorescence emission band, located at 450 nm, is observed under 350 nm excitation and has a quantum yield of 0.51. Quantum yields for both emission are higher than those of previous reports.[157,159-162,169-171]

The pH stability of the CDs are investigated through recording the fluorescence spectra (λ_{ex} of 350 nm and 440 nm) of the CDs solutions from pH 2 to pH 12 and the corresponding fluorescent intensity at ~450 nm and ~510 nm are shown in Figure 6.7A and 6.7B. The results indicate that the fluorescence of CDs is very stable over a wide pH range; only in strongly acidic or basic solutions do the fluorescent intensities decrease (by about 30%). The stable fluorescent intensity against a wide range of pH is unique since most of previously reported CDs showed pH-dependent properties.

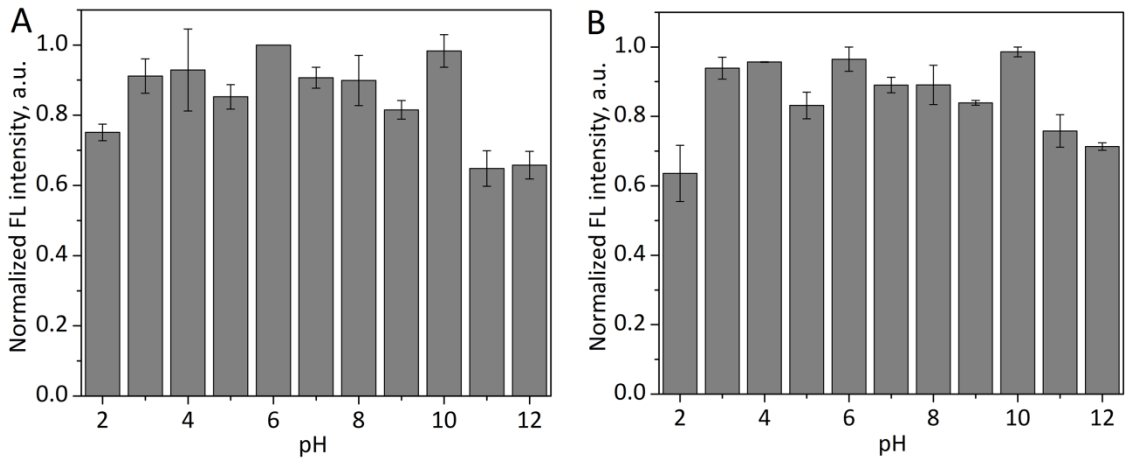

Figure 6.7 Normalized fluorescent intensity changes with pH in the range of 2-12. (A) Fluorescent intensities at ~450 nm excited at 350 nm. (B) Fluorescent intensities at ~510 nm excited at 440 nm.

The exact formation mechanism of the CDs with dual emission colors and high quantum yield currently remains elusive. Although the blue emission of CDs has been already extensively reported, the origin of green emission is still under debate. For green fluorescence, Yang and co-workers proposed that the fluorescence emission originates from the formation of special molecule-like states containing carboxyl groups and carbonyl groups in CDs.[171] We believe that co-doping of nitrogen and phosphorus into carbon nanomaterials affects the emission of CDs. It is found that the phosphorus element was introduced into the synthesis reaction for almost all the green fluorescent CDs in the literature.[157,159,160,162,169,170] Possibly the doping of phosphorus is the origin of the green fluorescence emission, which is under investigation in our group. Co-doping in N-doped carbon nanomaterials with a second heteratom (such as, P) can modulate the electronic properties, tune carbonaceous structure polarizability and exhibit excellent catalytic activity.[166,172,173] In addition, theoretical studies have predicted that defect induced by P doping or P, N co-doping can lead to the presence of a highly localized state close to the Fermi level.[172,174] Possibly co-doping of nitrogen and phosphorus affects the degree of

polymerization and graphitization. A higher graphitization degree induces a red-shift of fluorescence, resulting from the enhanced degree of π conjugation and the decreased band gaps.[159] The red shift of absorption and appearance of band at about 440 nm are consistent with enhanced degree of π conjugation.

6.2.3 N, P-CDs Application as Nitro-explosives Sensors

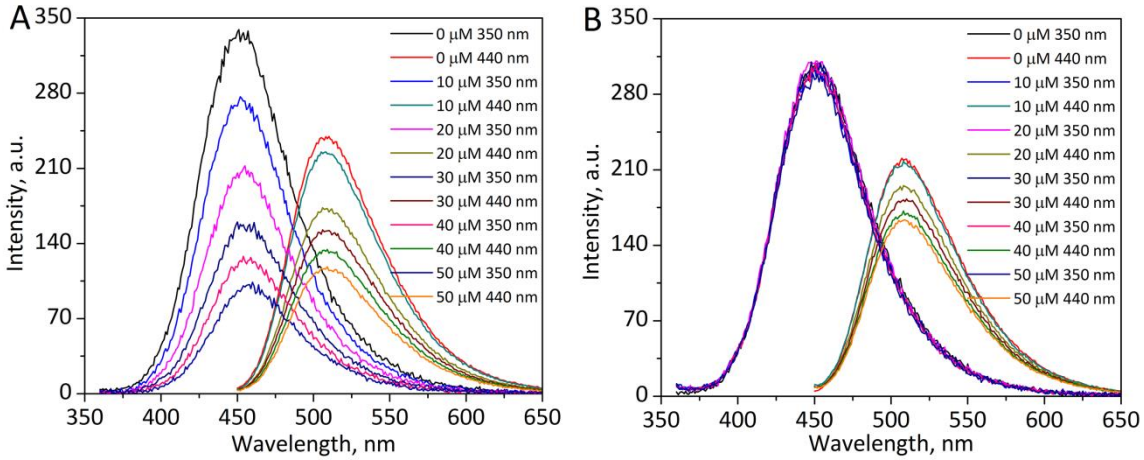

Figure 6.8 Explosives detection using diluted CDs solutions with incremental addition (0-50 μM) of (A) picric acid; and (B) TNT, respectively.

The carbon dots have dual fluorescence emission under different excitations. Due to their dual fluorescence emission and high quantum yield, the nanoparticles may have great potentials into the development of ratiometric sensors through using fluorescence changes of different emission peaks. Herein the detection and differentiation of nitro-explosives (picric acid and trinitrotoluene) was demonstrated through analysis of fluorescent intensities changes of different peaks. As shown in Figure 6.8A, with incremental addition of picric acid to diluted CDs solution in buffer solution (pH=7.50), the fluorescent intensities quench greatly for both blue and green emission. While TNT only quenches the green fluorescence emission, and the blue emission intensity keeps stable with increasing addition of TNT (0–50 μM) as shown in Figure 6.8B. Through integration

of blue and green emission quenching, differentiation and selective detection of picric acid and TNT is achieved.

The blue emission quenching by picric acid is possibly due to the overlap of picric acid absorption and blue emission peak, which has been already investigated in detail as Figure 5.12. The large overlap suggests the possibility of FRET process besides PET process, which leads to the fluorescence quenching. While little overlap between blue emission and TNT absorption excludes the presence of FRET process, therefore almost no quenching to blue emission by TNT is observed. While for green emission, both TNT and Picric acid quench the emission peak at ~510 nm. The phenomena could be attributed to the formation of Meisenheimer complex between NH_2 group on CDs and electron deficient compounds.[23] It has been reported that Meisenheimer complex had an absorption band at ~520 nm, which coincidently overlapped with green fluorescence emission greatly. The presence of FRET process is responsible for fluorescence quenching by both TNT and picric acid for green emission at ~510 nm.

Besides the ratiometric explosives detection, we anticipate that the synthesized CDs could be utilized in broad applications such as chemical sensing, biosensing, bioimaging, illumination, electronic devices, electrocatalysts, etc. For example, the CDs open the possibility for monitoring multiple analytes or species simultaneously because of dual fluorescence emission and high quantum yield. Especially in bio-imaging, the new CDs with green fluorescence could decrease the “water window” effect, indicating the interference of blue emission light between cells and tissues with conventional CDs could be prevented. These new applications will be continuously investigated in our group.

6.3 Conclusions

In conclusion, for the first time we synthesized nitrogen and phosphorus co-doped CDs through a facile and ultrafast microwave-assisted method using mPDA, phosphoric acid, and EDA. The as-synthesized CDs demonstrate dual (blue and green) fluorescence emission under different excitation wavelengths and high quantum yields of 0.51 for blue emission and of 0.38 for green emission. In addition the CDs solutions show excitation-dependent emission and pH-independent properties. The unique emission properties are attributed to the synergistic effect of co-doping of nitrogen and phosphorus into carbon nanomaterials. Furthermore, the CDs could work as a ratiometric sensor for differentiation and selective detection of nitro-explosives (picric acid and TNT) due to their dual fluorescence emission. The developed CDs could be utilized in broad applications such as chemical sensing, biosensing, bioimaging, illumination, electronic devices, electrocatalysts, etc. In addition, the present work provides valuable insights in to the development of fluorescent carbon dots with various emissions and high quantum yield.

Chapter 7

Protein-based Sensitive, Selective and Rapid Fluorescence Detection of Picric Acid in Aqueous Phase

Although great progress has been made on the fluorescence based nitro-explosives detection in recent years, several challenging issues still exist in current fluorescent materials for explosive detection. First, although popular, the conjugated polymers are often hampered by their time-consuming, low-yield and multi-step synthetic routes.[7,51,68] Second, other fluorescent materials are toxic and their potential leakage into the environment has increased much concern recently. For example, the toxicity of pyrene and related compounds discourage their routine use;[13] heavy metals such as Cadmium which have been widely used in quantum dots and metal-organic frameworks are also toxic to the environment and thus hamper their wide application.[21,40,69] Furthermore, limited aqueous stability/solubility of current fluorescent materials is another impediment that limits real-world applications.[10,21,45] Besides the already developed pyrene-doped polymer systems and fluorescent carbon nanoparticles in the previous work, fluorescent protein has attracted much attention for explosives detection because of its bio-compatible and environmental-friendly and fluorescent properties. In this chapter, bovine serum albumin (BSA) was applied as explosive sensors.

BSA, a protein derived from cows, has numerous applications due to its medical importance, low cost, ready availability, stability, unusual ligand-binding properties, etc.[20,175-177] BSA has two tryptophan residues (Trp-134 and Trp-212) that contribute to its intrinsic fluorescence. However, the application of BSA as a fluorescent protein for explosive sensing has not been fully

investigated. The work reported herein demonstrates, for the first time, that ordinary BSA is capable of sensitive and fast detection of picric acid with unprecedented selectivity.

Abstract

Even though several reports on fluorescence sensors for picric acid (PA) detection are available in literature, most of them lack the combined merits of high selectivity, low detection limit and quick response which are highly desirable for practical applications. In this work, highly-sensitive, ultra-selective and rapid detection of PA in aqueous media is accomplished using a protein fluorophore bovine serum albumin (BSA). This extraordinary sensing performance is ascribed to electron transfer and Förster resonance energy transfer (FRET) mechanisms as well as acid-base pairing interactions between amino groups of BSA and picrate anions of PA in aqueous solution. These features suggest this fluorescent protein as a promising explosives sensory material, and further genetically engineered fluorescent protein with appropriate functions might be one of the attractive research directions in explosive detection.

7.1 Experimental

7.1.1 Reagents

Bovine serum albumin (BSA, ≥98%, agarose gel electrophoresis lyophilized) was purchased from Sigma Aldrich. Sodium phosphate buffer (0.01 M, pH=7.4) was used for preparation of BSA solution. Nitro based explosives such as picric acid (PA, ≥99%), 2,4-dinitrotoluene (DNT, 97%), 1,3-dinitrobenzene (DNB, ≥99%), 2,4-dinitrophenol (DNP, ≥98%), 4-nitrophenol (4-NP, 99%), and 3-nitrophenol (3-NP, 99%) were purchased from Sigma Aldrich. 1,3,5-trinitroperhydro-1,3,5-triazine (RDX) (1000 μg/mL in acetonitrile) was bought from Chem

Service. 2,4,6-trinitrotoluene (TNT, 1000 μg/mL in acetonitrile), 2,4,6-trinitrophenylmethylnitramine (Tetryl, 1000 μg/mL in acetonitrile) was obtained from Ultra Scientific, while nitromethane (NM, 99+%) was bought from Acros Organics. 2-Nitrotoluene (2-NT, ≥99.0%) was obtained from Fluka. Octogen (HMX, 1000 μg/mL in acetonitrile: methanol) was purchased from SPEX CertiPrep. Pentaerythritol tetranitrate (PETN, 1000 μg/mL in acetonitrile) was bought from Cerilliant.

7.1.2 Equipment

The absorption spectra were performed on a Cary 50 UV-vis spectrophotometer (Agilent Technologies). Fluorescence emission spectra were measured using a Varian Cary Eclipse fluorescence spectrometer (Agilent Technologies). Circular dichroism measurements were conducted on a JASCO (J-710) spectropolarimeter by fixing the concentrations of BSA while varying the analyte concentrations.

7.1.3 Detection of Nitro-explosives in Aqueous Samples

The sensing experiments were carried out by monitoring the fluorescence quenching behavior of BSA solution upon the addition of target explosives at room temperature through a fluorescence spectrometer, in which the excitation and emission slit widths were adjusted according to the fluorescence intensities. Briefly, 3 mL of BSA solution was placed in a disposal cuvette and then the target solution was added successively. Each titration was repeated at least three times and consistent results are reported. The fluorescence emission experiments were excited at 279 nm, and the emission data were collected in the wavelength range of 290-450 nm. The quenching percentage (QP) was calculated using the equation as follows:

$$QP\ \% = (1 - I/I_0) \times 100\% \quad (7.1)$$

where I_0 is the initial fluorescence intensity in the absence of analyte, I is the fluorescence intensity in the presence of corresponding analyte.

7.2 Results and Discussion

7.2.1 Nitro-explosives Detection Using Fluorescent Protein BSA

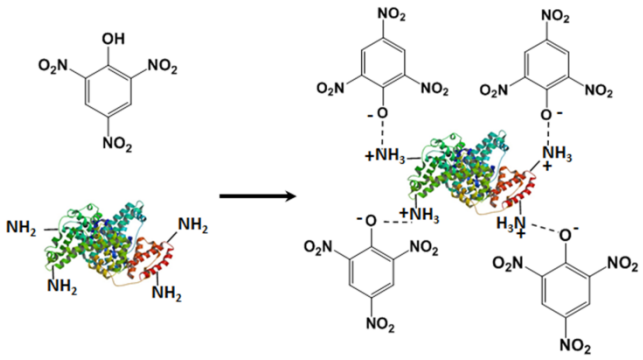

Scheme 7.1 Schematic illustration of the selective electrostatic interactions between BSA and picric acid.

BSA in water has an absorption peak at 279 nm and exhibits a broad strong emission peak at ~ 348 nm when excited at 279 nm (Figure 7.1). Fluorescence is strongly quenched upon incremental addition of PA to 0.5 µM BSA solution (Figure 7.2). Due to the curvature noted in the corresponding Stern-Volmer plot (0.5 µM BSA, red triangles, Figure 7.2 B), ground state association between BSA and PA was suspected (Scheme 7.1), and hence, the effect of BSA concentration on PA detection has been examined (Figure 7.2 B). Trading-off the sensitivity and detection range, 0.5 µM of BSA was used in the later study. The detection limit for PA is 17.2 nM (3.9 ppb) using 0.5 µM of BSA fluorophore. This sensitivity is better than those of most current fluorescent PA sensors (See Table 7.1). In addition, the response time of BSA sensors to PA was investigated by monitoring the fluorescence intensity as a function of time at different concentrations of the analyte. The response to PA is almost instantaneous, and the equilibrium is

also reached rapidly. The response and equilibrium time is less than 1 min, which is much better than the reported response time for PA fluorescence sensors.[155]

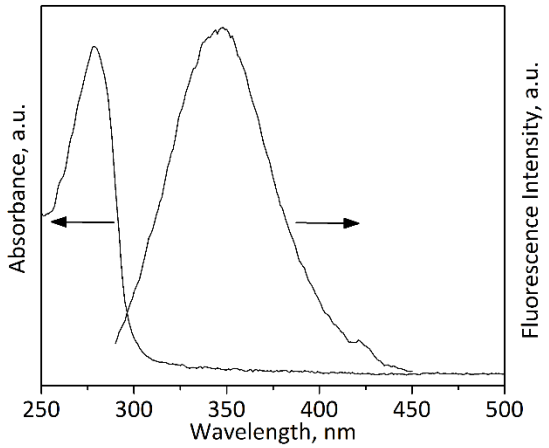

Figure 7.1 Absorption and emission spectra of BSA solution (emission spectrum upon excitation at 279 nm).

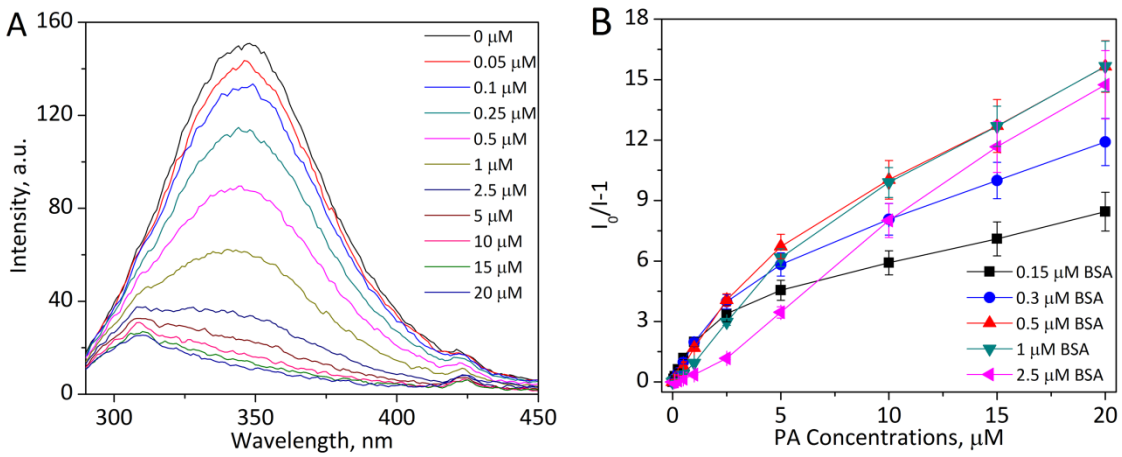

Figure 7.2 (A) Fluorescence spectra of 0.5 μM BSA upon addition of various PA concentrations in water. (B) Stern-Volmer Plots for PA detection using various concentrations of BSA.

Table 7.1 Comparison of present results with previous fluorescent picric acid sensors

Reference	K_{SV} (M^{-1})	Detection limit	Selectivity
J. Mater. Chem., 2009, 19, 7347	/	4.8 ppb	High
Adv. Funct. Mater., 2009, 19, 905;	1.09×10^5	0.2 ppm	High
Macromol. Rapid. Commun. 2010, 31, 834	9.09×10^3	1 ppm	/
Chem. Commun., 2011, 47, 4505	/	98.5 ppb	High
Chem. Commun., 2011, 47, 10046	2100	/	Low
J. Photochem. Photobiol., A 2011, 217, 356	5×10^4	2.3 ppb	Low
ACS Appl. Mater. Interfaces 2011, 3, 1245	5.7×10^3	70 ppb	High
Inorg. Chem. 2011, 50, 1506	1×10^5	/	Low
Inorg. Chem. 2012, 51, 13072	/	/	Low
Chem. Commun., 2012, 48, 7167	2.5×10^5	0.4 ppm	Low
J. Mater. Chem., 2012, 22, 11574	3.04×10^4	23 ppb	Moderate
Anal. Chem., 2012, 84, 8415	/	32.3 ppb	High
Chem. Commun., 2012, 48, 5007	9.9×10^4	3-300 ppb	Low
Angew. Chem. Int. Ed., 2013, 52, 2881	3.5×10^4	0.916 ppm	High
ACS Appl. Mater. Interfaces, 2013, 5, 672	1.55×10^4	80.2 ppb	Moderate
ACS Appl. Mater. Interfaces, 2013, 5, 5373.	3.2×10^6	0.9 ppb	High
Chem. Commun., 2013, 49, 4764.	1.9×10^4	/	High
J. Am. Chem. Soc., 2013, 135, 17310;	7.8×10^4	1 ppm	High
J. Org. Chem., 2013, 78, 1306	3.8×10^4	/	High
Chem. Commun., 2014, 50, 6031	5.28×10^4	/	Moderate
ACS Applied Mater. Inter. 2014, 6, 10722	1.32×10^5	125 ppb	High
Asian J. Org. Chem. 2014, 3, 805	3.57×10^5	0.23 ppb	High
Present Study	$\mathbf{1.65\times10^6}$	**3.9 ppb**	**Very high**

Fluorescence quenching titrations were also conducted with other nitro explosives. All the other analytes showed little effect on the fluorescence intensity of BSA (Figure 7.3A-I and Figure 7.4). One can see from Figure 7.4A that the fluorescence quenching percentage for 2.5 μM PA is 80.1%, while the same concentration of all the other analytes only quenches less than 8%. These results suggest that BSA fluorescent sensor possesses high selectivity toward PA against other nitro explosives.

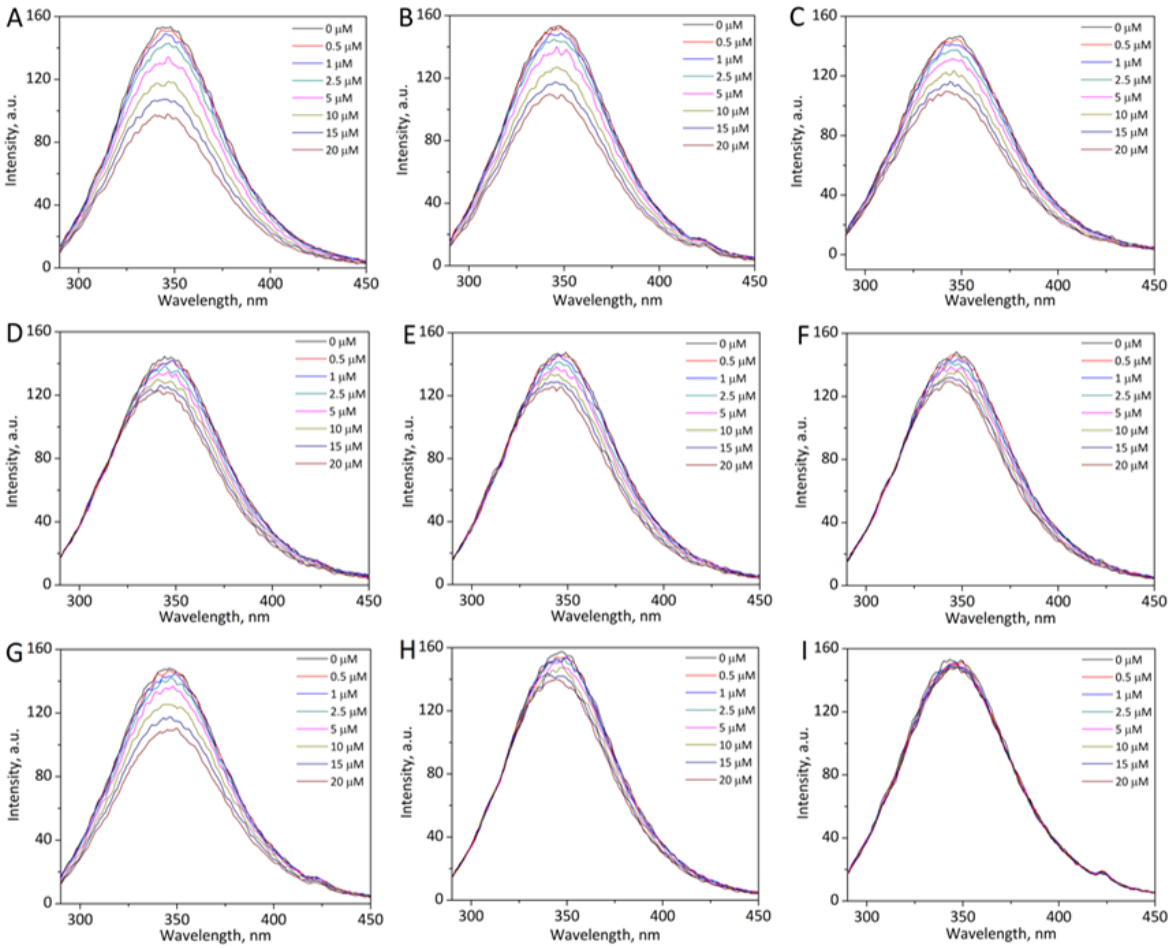

Figure 7.3 Fluorescence spectra of BSA upon addition of various nitro-explosives in aqueous solution. (A) Tetryl; (B) 2-NT; (C) TNT; (D) HMX; (E) PETN; (F) RDX; (G) DNT; (H) DNB; (I) NM.

The quenching behaviour is also characterized by the quenching efficiency (I/I_0) and quenching constant (K_{SV}) using the Stern-Volmer (S-V) equation, $I_0/I = K_{SV}[A] + 1$, where I_0 is the initial fluorescence intensity in the absence of analytes, I is the fluorescence intensity in the presence of analytes, [A] is the molar concentration of analytes, and K_{SV} is the quenching constant (M^{-1}). The intensity for BSA emission peak at ~348 nm are plotted versus the concentration of various analytes and shown in Figure 7.4B. As shown in Figure 7.5, the S-V plot for PA shows two linear regions at low and high concentration ranges, respectively, and bends downward at high concentrations. In the low concentration range, the K_{SV} value was calculated as 1.65×10^6 M^{-1},

and the correlation coefficient R^2=0.999; in the high concentration range, the K_{SV} value was calculated as 5.90×10^5 M^{-1}, and the correlation coefficient R^2=0.997. The phenomenon can be presumably attributed to the presence of two fluorophore populations, self-absorption or energy transfer processes.[8,21,71] For BSA intrinsic fluorescence, Trp-212 is located within a hydrophobic binding pocket of the protein and Trp-134 is located on the surface of the molecule.[177] The Trp fluorescence quenching is regarded as a sensitive technique for measuring ligand binding affinities.

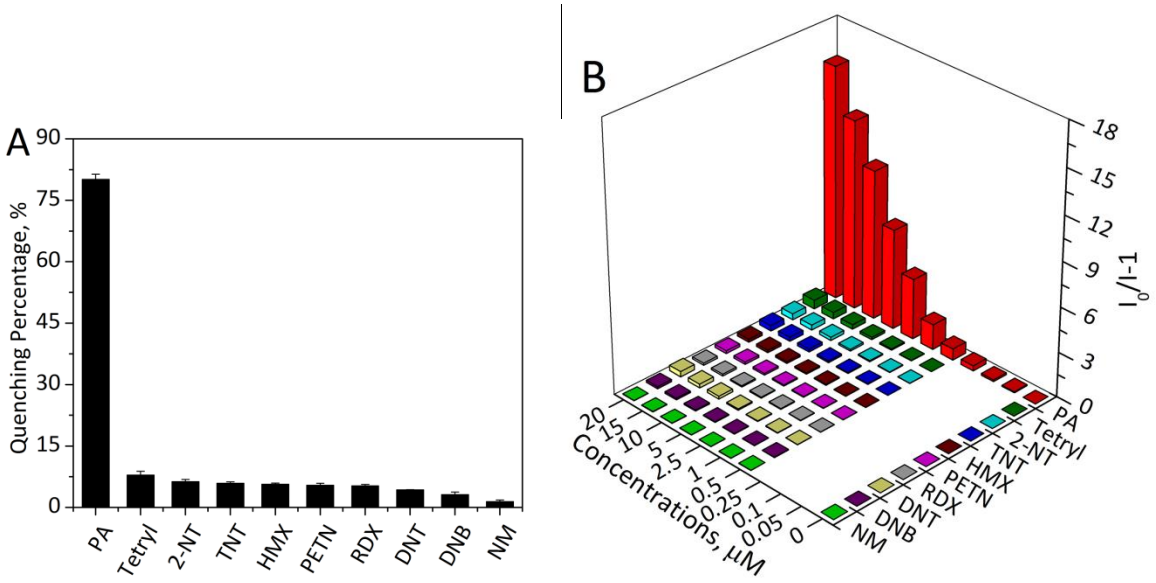

Figure 7.4 (A) Percentage of fluorescence quenching obtained for BSA fluorescent sensors upon addition of 2.5 μM of different nitro-explosives (BSA concentration is 0.5 μM BSA), indicating excellent selectivity for picric acid. (B) Stern-Volmer plots of BSA fluorescent sensors with different nitro-based explosives at 0.5 μM BSA.

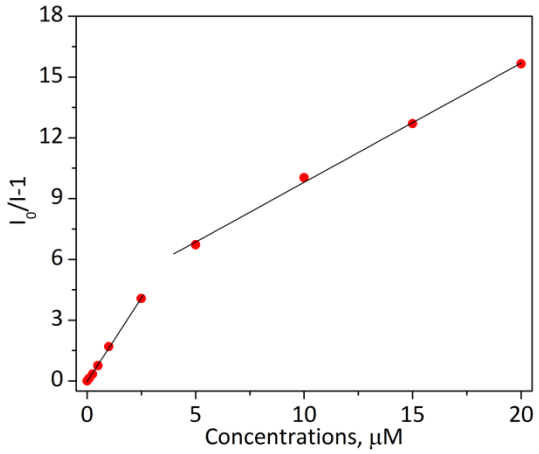

Figure 7.5 Linear fitting of Stern-Volmer plot for PA explosive detection using 0.5 μM BSA.

The quenching constant for PA is 1.65×10^6 M^{-1} in the low concentration range, which is almost the largest value during the reported fluorescence PA sensors (Table 7.1).[21,34,44,134,155,178-182] The calculated quenching constant for PA is about two orders larger than those for other nitro-explosives (Table 7.2, e.g., TNT of 1.64×10^4 M^{-1}; DNT of 1.77×10^4 M^{-1}, etc.), which is one of the highest value known, suggesting an unprecedented selectivity to PA of the as-developed sensor. [21,44,155,178-180]

Table 7.2 Fluorescence quenching constant K_{SV} values for the various explosive analytes

Analytes	K_{SV} (M^{-1})
PA	1.65×10^6
Tetryl	2.85×10^4
TNT	1.64×10^4
DNT	1.77×10^4
2-NT	1.98×10^4
DNB	5.39×10^3
NM	/
RDX	5.62×10^3
PETN	7.92×10^3
HMX	7.86×10^3

7.2.2 Sensing Mechanism for Selective and Sensitive Detection of PA

Generally, photo-induced electron transfer (PET) plays a key role in explosive quenching process due to the electron-deficient nature of explosives.[21,30,112] The driving force is the energy

difference between the lowest unoccupied molecular orbital (LUMO) of fluorophore and LUMO of analytes. The LUMO values for different nitro-explosives are summarized in Table 7.3. As expected, because of its small LUMO value, the PET driving force for PA is larger than that of other analytes. This may partly explain the sensitivity and selectivity of BSA sensors to PA detection. However, the order of fluorescence quenching percentage is not in complete accordance with LUMO energy sequences; in addition, although PA and Tetryl have very similar LUMO values, the quenching performance demonstrates a large difference. These findings suggest that PET is not the sole mechanism for the observed fluorescence quenching.

Table 7.3 LUMO and HOMO energies calculated for the various explosive analytes (at the B3LYP/6-31G* level of theory)[4,21,52]

Analytes	LUMO (eV)	HOMO (eV)	Band gap (eV)
PA	-3.89(-4.32)	-8.22(-8.60)	4.33(4.28)
Tetryl	-3.92	-8.11	4.19
TNT	-3.48	-8.44	4.96
DNT	-2.97	-8.11	5.14
2-NT	-2.75	-7.56	4.81
DNB	-3.43	-7.99	4.56
NM	-1.90	-8.03	6.13
RDX	-2.53	-8.25	5.71
PETN	-3.08	-8.71	5.63
HMX	-2.72	-8.30	5.58

The non-linearity of the S-V plot for PA possibly suggests ground state association of the donor and the acceptor followed by an energy transfer from the excited donor to the ground state acceptor. Energy transfer mechanism has been used to develop a number of elegant fluorescence sensors, and can dramatically enhance the fluorescence-quenching efficiency and also improve sensitivity.[21,23] According to Förster resonance energy transfer (FRET) theory,[6,12,20] the rate of energy transfer depends on: 1) the relative orientations of the donor and acceptor dipoles, 2) the extent of overlap of fluorescence emission spectrum of the donor (the fluorophore) and absorption spectrum of the acceptor (the analyte), and 3) the average distance between the donor and the acceptor. The probability of resonance energy transfer depends upon the extent of

spectral overlap between these molecules. Figure 7.6 depicts the absorption spectra of various analytes and emission spectrum of BSA.

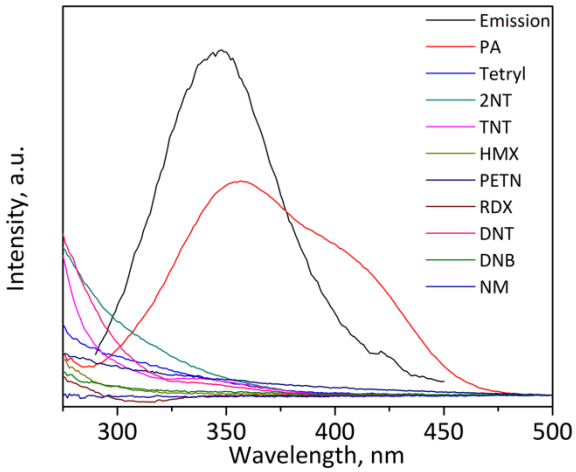

Figure 7.6 Absorption spectra of various explosive analytes and emission spectrum of BSA in aqueous solutions.

The large overlap between absorption spectrum of PA and emission spectrum of BSA was observed, while almost no overlap for other analytes. Degree of overlap J(λ) in M^{-1} cm^{-1} nm^4, expresses the degree of spectral overlap between the donor emission and the acceptor absorption, J(λ) is given by:

$$J(\lambda) = \frac{\int_0^\infty F(\lambda)\varepsilon(\lambda)\lambda^4 d\lambda}{\int_0^\infty F(\lambda)d\lambda} \qquad (7.2)$$

where F(λ) is the corrected fluorescence intensity of the donor in the wavelength λ to λ+Δλ, ε(λ) is the extinction coefficient of the acceptor at λ in M cm^{-1}. We could calculate that J(λ) for picric acid, $J(\lambda)=1.16\times10^{14}$ M^{-1} cm^{-1} nm^4. Degree of spectra overlap integral J(λ) values for various explosive analytes were calculated and shown in Table 7.4. Thus the efficient quenching at ~348 nm for PA demonstrates a much higher quenching response because of higher probability of resonance energy transfer.

In addition, the average distance (r_0) between the donor and the acceptor, picric acid was also calculated through the following steps. The efficiency of energy transfer between the donor and the acceptor, E, could be calculated by the following equation[12,20,183]:

$$E = 1 - \frac{F}{F_0} = \frac{R_0^6}{R_0^6 + r_0^6} \quad (7.3)$$

where r_0 represents the distance between the donor and acceptor, and R_0 is the critical distance at which energy transfer efficiency equals to 50%. The value of R_0 is calculated using the equation:

$$R_0^6 = 8.79 \times 10^{-5} K^2 n^{-4} \emptyset J(\lambda) \text{ (in Å}^6\text{)} \quad (7.4)$$

where K^2 is the orientation factor related to the geometry of the donor-acceptor dipole, n is the refractive index of the medium, ∅ is the fluorescence quantum yield of the donor. In the present case, K^2 =2/3, n=1.36, and ∅=0.15. When C(PA)=C(BSA)=0.50 μM, E=0.432, according to Eqs. (7.2)-(7.4), the donor-to-acceptor distance r_0 is obtained as 2.70 nm, on the 2-8 nm scale, which greatly satisfies FRET requirements.

Table 7.4 Degree of spectra overlap integral J(λ) values for the various explosive analytes.

Analytes	J(λ) (M^{-1} cm^{-1} nm^4)
PA	1.16×10^{14}
Tetryl	8.42×10^{12}
TNT	7.10×10^{12}
DNT	6.10×10^{12}
2-NT	1.19×10^{13}
DNB	2.12×10^{12}
NM	7.84×10^{11}
RDX	7.72×10^{11}
PETN	9.82×10^{12}
HMX	1.08×10^{12}

Furthermore, as a protein, BSA has a large number of amino groups, which might function as receptors for the nitroaromatic compounds. In the aqueous solution, PA behaves as a strong acid due to the three nitro groups affixed on the benzene ring, thus it can easily form a charged anion.

As expected, BSA with high content of electron-rich amino groups could effectively bind to PA by the acid-base pairing interactions, and the charge transfer complexing interactions would lead to BSA fluorescence quenching.[21,155,178] Since the electron-withdrawing effect of the nitro group plays a crucial role in the interaction between PA and BSA, further fluorescence quenching titrations were conducted using 2,4-dinitrophenol (DNP), 4-nitrophenol (4-NP) and 3-nitrophenol (3-NP). As shown in Figure 7.7, the quenching efficiency follows the order PA>DNP>4-NP>3-NP, which is in complete agreement with the order of acidity of these analytes, where the pKa values of the quenchers are 0.38 for PA, 4.89 for DNP, 7.15 for 4-NP, and 8.4 for 3-NP.

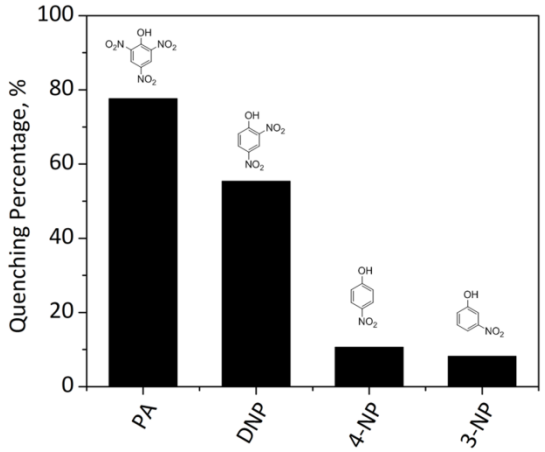

Figure 7.7 Comparison of quenching percentage of BSA fluorescent sensors upon addition of various 2.5 μM nitrophenols.

In addition, the quenching efficiencies of PA and DNP are much higher than their corresponding structurally similar nitro compounds (TNT, DNT and DNB). This feature when coupled with the magnitudes of the overall integrals may explain the molecular basis for the unprecedented selectivity for PA, as other nitro compounds do not have a hydroxyl group and so they cannot interact efficiently with amino groups of BSA, thus resulting in a very low quenching efficiency. In addition, the interaction of the hydroxyl groups with the basic sites in BSA is expected to follow the order of their acidity. PA, with its highly acidic hydroxyl group interacts strongly with

the fluorophore and the quenching effect is carried over long range dipolar interactions owing to energy transfer mechanism, thus resulting in an amplified response.

Circular dichroism (CD) is highly sensitive to protein conformational changes which normally accompany upon interactions with small molecules. As can be seen in Figure 7.8, BSA exhibits two negative CD bands at 208 and 222 nm in the ultraviolet region, characteristic of its typical α-helix structure.[20,183] The intensities of two double minimum reflect the amount of helicity of BSA and further indicate that BSA contains more than 50% of α-helical structure. Upon addition of PA to BSA solution, the intensities of double minimum were reduced which is directly related to the interaction between PA and BSA. Therefore, the α-helix content of the protein secondary structure decreases as PA interacts with the BSA molecule, providing direct evidence that protein secondary structural changes are responsible for the quenching of BSA fluorescence by PA. Thus, direct evidence for the origins of quenching is provided which is in support of the above proposed energy transfer mechanism for explosive detection.

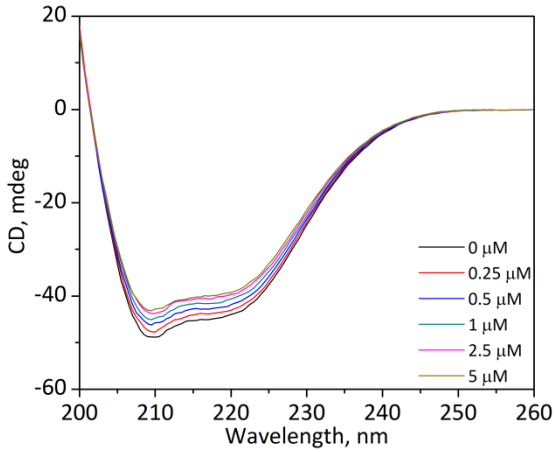

Figure 7.8 CD spectra of 0.5 μM BSA in the presence of various concentrations of PA.

7.3 Conclusions

We have successfully employed BSA as a fluorophore to detect PA in aqueous media, exhibiting high-sensitivity (LOD as low as 17.2 nM), ultra-selectivity (about two orders of K_{sv} values larger than that of other nitro-explosives), and short response time (less than 1 minute). These features can be explained by combined electron transfer and energy transfer due to large overlap between absorption spectrum of PA and emission spectrum of BSA as well as acid-base pairing interactions between amino groups of BSA and charged anion of PA. The present study provides insights into the design of a cheap and simple PA fluorescence sensor which is completely biodegradable and environmental-friendly.

Chapter 8

Summary, Future Prospects and Challenges

8.1 Summary

The reliable detection of explosives is one of the pressing concerns in anti-terrorism efforts and environmental pollution controls. Up to date, fluorescence-based sensing technology represents one of the most promising approaches for trace explosives detection due to the advantages such as short response time, excellent sensitivity, and instrumental simplicity. Chapter 1 briefly introduces the methods and mechanisms for fluorescence based explosives detection, and current fluorescent materials in explosives detection such as conjugated polymers, small molecule fluorophores, supramolecular systems and bio-inspired fluorescent materials. Fluorescent nanomaterials for explosives detection are also reviewed. This dissertation aims at developing novel fluorescent nanomaterials for fast, sensitive, selective, reliable and cost-effective detection of nitro-explosives.

Early research (Chapter 2-4) focused on the pyrene-doped polymer systems. Firstly in Chapter 2, a novel 3D nanoporous fluorescent film was prepared via simple dip-coating of PS and Py solutions, and then its application for the sensitive and selective detection of explosive vapor was investigated. Morphology investigations revealed that the fluorescent polymer films consisted of high-surface, three-dimensionally nanoporous array of holes. The possible molecular origin of fluorescence quenching was investigated through structural XRD studies and the electronic structure (optical properties, band gap and conduction band determinations) of the polymer films. Later super-hydrophobic

fluorescent sand was prepared and applied for buried explosives detection in Chapter 3. The results suggested that all the buried explosives could be successfully observed by naked eyes using a handheld UV lamp without advanced equipment. In order to detect nitro-explosives in aqueous phase, pyrene-polyethersulfone electrospun nanofibers were synthesized through electrospinning in Chapter 4. The effects of mixed solvent ratio and polymer/fluorophore concentrations on nanofiber's morphology as well as its sensing performance were systematically investigated and optimized. The current film sensor demonstrated excellent sensitivity, selectivity and reusability to nitro-explosives detection. FRET and PET mechanism were used to explain the fluorescent quenching phenomena by nitro-explosives. Further lifetime studies indicated a static quenching mechanism was dominant in fluorescence quenching process.

Considering the toxicity of pyrene as a fluorophore, we also developed fluorescent materials with low-toxicity for nitro-explosives detection. Carbon nanoparticles or carbon dots have received much attention because of their low toxicity, facile synthesis, great aqueous solubility and excellent optical properties. In Chapter 5, an ultrafast and facile method for the preparation of nitrogen-doped CNPs has been developed from a single precursor under microwave conditions. The obtained CNPs showed strong blue fluorescence with a quantum yield of ~20% and displayed excitation-independent fluorescence behavior. The mechanism of nanoparticle formation was also discussed and proposed. In addition, the fluorescence of CNPs could be quenched significantly by picric acid, while other nitro-explosives had little effect on the fluorescence intensity. In order to develop fluorescent carbon nanoparticles with high quantum yield, dual fluorescence emission and excitation-dependent properties, in Chapter 6, CDs co-doped with nitrogen and phosphorus were proposed and prepared using nitrogen, phosphorus and

carbon sources in one pot through a simple, fast and microwave-assisted method. The as-synthesized CDs demonstrated excitation-dependent properties, dual (blue and green) emission color, and high quantum yield (0.51 for blue emission and 0.38 for green emission). Because of their unique fluorescence properties, the CDs were applied as ratiometric sensors for selective detection and differentiation between picric acid and TNT. Finally in Chapter 7, a fully biodegradable and environmental-friendly biopolymer (protein) showed sensitive, selective and rapid detection of picric acid. This extraordinary sensing performance was ascribed to the synergistic effect of electron transfer and Förster resonance energy transfer (FRET) mechanisms as well as acid-base pairing interactions between amino groups of BSA and picrate anions of PA in aqueous solution.

Overall, this dissertation covers a broad range of fluorescent nanomaterials (such as pyrene-doped polymers, fluorescent carbon dots, and fluorescent proteins) for nitro-explosives sensing. The work here provides valuable insights into the rational design and synthesis of fluorescent nanomaterials, which could be utilized in a wide range of applications beyond nitro-explosives detection.

8.2 Future Prospects and Challenges

The needs for homeland security and demining activities result in an intense interest of the explosives detection. The fluorescence based methods hold much promise to satisfy most of the criteria required for an effective sensing platform, such as high sensitivity and selectivity, fast speed, simplicity, portability, and low-cost. The fluorescent materials integrating with other technologies such as electronics, imaging, and sensor design could play more important roles in

real explosives detection such as buried landmines, environmental contamination in soil, groundwater and seawater.

NAC explosives, such as TNT, DNT and picric acid, have been intensely investigated with established detection methods, however, direct detection of RDX, PETN and the continually increasing variety of explosives compounds encountered by police and security agencies worldwide are still remaining a huge challenge. It has been reported that using currently effective sensing tools such as FidoXT, IMS, mass spectrometry, are not able to directly detect RDX and PETN, or only able to detect the modified RDX or its degradation product.[184] Considering their vast use in plastic bonded explosives, RDX and PETN are important explosive targets for sensing and devote more efforts. It is highly desirable to develop a fluorescent detection system that not only detects a broad range of nitrated explosives, including NACs, nitroalkanes, nitroamines, and nitrate esters, but also differentiates them from each other. Through designing selective reactions between fluorescent materials and different explosives, it is possible to generate some novel fluorescent materials that can selectively detect and differentiate between different explosives.

Moreover, researchers should have more practical view on designing novel explosive sensing systems. Currently, most of explosives fluorescent probes are developed and tested in the laboratory environment. Although the detection sensitivities of fluorescent probes for NACs has reached satisfactory levels, their applicability for directly detecting TNT or DNT vapors from packed bombs or landmines under real circumstances is not addressed and unknown. Current technologies accomplish indirect explosive detection by sensing more volatile taggant, such as DMNB. Beyond laboratory tests, further development should be more focusing on real situations such as explosive detection in fields and transportation hub screenings. The demand to detect

explosives from a safe standoff distance presents another interesting direction for explosives detection in real applications. We already reported the naked-eye based detection of buried explosives, which is attractive.[38,113] Due to benefits such as the simplicity and without the use of advanced equipment, visual-based explosives detection could benefit a lot in real applications. In addition, for ease of visual detection, a change in the luminescence color in the presence of an analyte is a more desirable indicator than the disappearance of luminescence.

For any real application, sensory materials also need to meet several requirements such as low cost, environmental-friendly, and long term stability. PPE conjugated polymers are one kind of materials which have been used in commercialized devices. However, these polymers require complicated and time-consuming synthetic routes from monomer design to polymerization, which is a clear drawback for mass production. Photo-stability issues of conjugated polymers have also aroused much attention recently.[185] As well known, other popular fluorescent materials such as PAHs, quantum dots and MOFs also have problems such as toxicity, which may contaminate the environment and be toxic to the plants, animals or human beings. These potential issues requires researchers to develop novel, low-cost, environmental-friendly and stable fluorescent materials. In this regard, it seems to be a promising choice to use high-performance small molecule fluorophores as the model units to modify the side chains of commercially available conjugated polymers, as the modification on the side polymer chains could be accomplished in much simpler one-step reaction. By carefully designing the modification sites, the functionalized polymer may obtain higher sensitivities with extended exciton migration and better processability. Moreover, supramolecular systems were recently reported with excellent sensing performance, and could hold great promise in explosives detection if they could solve the issues such as high cost and low-scalability. Recently we used

fluorescent proteins to develop an environmental-friendly explosive sensor with high sensitivity and ultra-selectivity.[130] Such environmental-friendly fluorescent proteins can be mass-produced with low cost, therefore, genetically engineered fluorescent protein with appropriate functions might be one of the attractive research directions in explosive detection.

Regarding the sensing mechanism, PET mechanism plays a role in most quenching response in explosive detection, but this process is considered as trivial and non-selective in general, since the quenching of fluorescence may result from electron-deficient compounds other than nitrated explosives. Therefore, the sensing mechanisms relying on more selective and efficient interaction are predicted to further develop in next few years such as FRET, electron exchange, ICT, etc., which can be realized through rational design of the fluorescent sensory materials. For example, the introduction of primary amines has been applied to selectively sense nitroaromatics, such TNT and Tetryl, through FRET quenching.[186,187] The other perspective of FRET utilization is selective detection of picric acid through tuning the emission spectra of fluorophores to efficiently overlap with absorption spectrum of picric acid.

Fluorescence quenching method still dominates in fluorescence-based explosives detection, however, it is necessary to exploit other fluorescence phenomena for explosives sensing. Theoretically, any phenomenon that results in a change of fluorescence intensity (quenching or enhancement), wavelength, anisotropy, or lifetime can be used for sensing. It is expected that fluorescence enhancement is a more sensitive technique due to its little influence by fluorescence background. Generally, explosives lead to fluorescence quenching due to PET process from excited fluorophore to electron deficient explosives. Through optimization of molecular orbitals of fluorophores, it is expected that electron transfer direction is reversed for some explosives, thus leading to reversed sensing phenomena for different explosives. Furthermore, it is highly

attractive to design a sensing system in which nitro-explosives can interrupt the already existed quenching process, thus leading to fluorescence enhancement. Phenomena of spectra shift and lifetime changes can also be applied for explosives sensing. Through harnessing these phenomena, the future will witness that fluorescence methods play more important roles in sensing explosives.

It is also very attractive to develop bi-modual sensors for explosive detection as they can greatly enrich the information output. Bi-modular sensor can be realized by integrating fluorescence technology with other sensing technologies.[188] For example, conjugated polymers are one of the most popular fluorescent materials for the detection of nitro explosives. Besides fluorescence response, some polymers also showed resistivity/conductivity changes upon exposure to explosives. Sensing reliability, sensitivity or selectivity could be improved through integration of different sensing technologies into one sensor. As reported, through the integration of fluorescence quenching and photoconductivity experiments, TNT and DNT were detected and differentiated.[189] In addition, integration of fluorescence and surface enhanced Raman scattering (SERS) was another achieved solution in bi-modual explosive detection through metal enhanced fluorescence. For example, Pradeep's group designed Au core/silica shell structures for enhanced fluorescence and Raman scattering, thus realizing selective visual detection of TNT at the sub-zeptomolar level.[41] By combining the high sensitivity and selectivity offered by SERS with the fluorescence method, the accuracy and reliability of the detection technique was greatly enhanced.

The use of sensor arrays is another popular solution to address the issues of poor selectivity that perplexed explosive detection. In conjunction with artificial neural network, the data from sensor array can be used to detect and differentiate a broad range of explosives. Very recently, a sensor

array was achieved through utilization of 3 novel fluorescent polymeric sensory membranes.[190] Upon exposure to explosive vapors, the fluorescence variation, both turn-on and turn-off were recorded and simultaneous treated using multivariate techniques, thus permitting the differentiation of the explosives from explosive mimics or interferents, discrimination between explosives, the ability to assess the probability of false non-detection of an explosive and probability of false detection. The fluorescent spectra in terms of intensity vs. wavelength at various times for each of the 3 membranes had a highly defined internal structure, and only 3 principal components (PCs) were needed for the description of each membrane using principle component analysis (PCA). PCA allows for both discrimination between explosive and their mimics and for distinction between the 3 explosives.

Another future trend in fluorescence-based explosive detection is to better understand the involved sensing mechanisms and the relation between sensing material and sensing performance. Up to date, most of the fluorescent sensory materials used in explosive detection have been developed empirically and/or by a method of trial and error. Therefore, it is desirable to use theory prediction (such as molecular orbitals) to rationally design the sensory material. To accomplish this goal, simulation and theory studies are necessary to be integrated with material synthesis and rational design in order to achieve materials with better electronic structures and predictable sensing performance. For example, density functional theory computation is a powerful tool to study the electronic properties of luminescent materials and analyte interactions from a theoretical perspective. By deliberately tuning the crystal structures, composition and porosity, optimal electronic structures, optical emission and redox properties of sensing materials, the sensing performance of materials could be significantly improved, which could establish guidelines for the materials design and develop reliable criteria for predicting and

identifying the most suitable materials for sensitive and selective detection of explosives. Besides the materials development, understanding how the analyte molecules diffuse into the sensing films and interact with the chromophore is another direction for mechanism studies. Shaw and co-workers applied Quartz crystal microbalance (QCM) and neutron reflectance (NR) to analyze the diffusion of nitroaromatics to dendrimer films, they found that the sorption process was spontaneous and independent of the film thickness. Combination of QCM, NR, and ab initio quantum chemistry calculations may provide insights into ascertaining the sorption process in sensing materials for nitro-explosives.[191]

Although fluorescence-based explosive detection encounters many challenges in terms of sensitivity, selectivity, stability and cost, we believe, with current advances in rational design of sensory materials and progress in simulation and computation modeling, fluorescent-based explosive sensors will have a promising and bright future.

References

1. S. Singh. *J. Hazard. Mater.*, 2007, **144**, 15-28.
2. K. G. Furton and L. J. Myers. *Talanta*, 2001, **54**, 487-500.
3. J. Akhavan. *The chemistry of explosives*. (Royal Society of Chemistry, 2011).
4. J. C. Sanchez, A. G. Dipasquale, A. L. Rheingold and W. C. Trogler. *Chem. Mater.*, 2007, **19**, 6459-6470.
5. H. Östmark, S. Wallin and H. G. Ang. *Propellants, Explos., Pyrotech.*, 2012, **37**, 12-23.
6. S. W. Thomas, G. D. Joly and T. M. Swager. *Chem. Rev.*, 2007, **107**, 1339-1386.
7. M. E. Germain and M. J. Knapp. *Chem. Soc. Rev.*, 2009, **38**, 2543-2555.
8. Y. Salinas, R. Martinez-Manez, M. D. Marcos, F. Sancenon, A. M. Costero, M. Parra and S. Gil. *Chem. Soc. Rev.*, 2012, **41**, 1261-1296.
9. S. J. Toal, D. Magde and W. C. Trogler. *Chem. Commun.*, 2005, 5465-5467.
10. X. Wang, Y. Guo, D. Li, H. Chen and R.-C. Sun. *Chem. Commun.*, 2012, **48**, 5569-5571.
11. A. Pettersson, S. Wallin, B. Brandner, C. Eldsäter and E. Holmgren. *Explosives detection-a technology inventory*. (Weapons and Protection, Swedish Defence Research Agency (FOI), 2006).
12. J. R. Lakowicz. *Principles of Fluorescence Spectroscopy*. 3rd. edn, (Springer, 2006).
13. M. S. Meaney and V. L. Mcguffin. *Anal. Chim. Acta*, 2008, **610**, 57-67.
14. G. He, N. Yan, J. Yang, H. Wang, L. Ding, S. Yin and Y. Fang. *Macromolecules*, 2011, **44**, 4759-4766.
15. H. Nie, Y. Lv, L. Yao, Y. Pan, Y. Zhao, P. Li, G. Sun, Y. Ma and M. Zhang. *J. Hazard. Mater.*, 2014, **264**, 474-480.
16. S. Madhu, A. Bandela and M. Ravikanth. *R. Soc. Chem. Adv.*, 2014, **4**, 7120-7123.
17. S. Pramanik, C. Zheng, X. Zhang, T. J. Emge and J. Li. *J. Am. Chem. Soc.*, 2011, **133**, 4153-4155.
18. X. Liu, Y. Xu and D. Jiang. *J. Am. Chem. Soc.*, 2012, **134**, 8738-8741.
19. D. Banerjee, Z. Hu, S. Pramanik, X. Zhang, H. Wang and J. Li. *CrystEngComm*, 2013, **15**, 9745-9750.
20. Y.-Z. Zhang, X. Xiang, P. Mei, J. Dai, L.-L. Zhang and Y. Liu. *Spectrochim. Acta, Part A*, 2009, **72**, 907-914.
21. S. S. Nagarkar, B. Joarder, A. K. Chaudhari, S. Mukherjee and S. K. Ghosh. *Angew. Chem. Int. Ed.*, 2013, **52**, 2881-2885.
22. D. Dinda, A. Gupta, B. K. Shaw, S. Sadhu and S. K. Saha. *ACS Appl. Mater. Interfaces*, 2014, **6**, 10722-10728.
23. Y. Wang, A. La, C. Brückner and Y. Lei. *Chem. Commun.*, 2012, **48**, 9903-9905.
24. L. Feng, H. Li, Y. Qu and C. Lu. *Chem. Commun.*, 2012, **48**, 4633-4635.
25. E. R. Goldman, I. L. Medintz, J. L. Whitley, A. Hayhurst, A. R. Clapp, H. T. Uyeda, J. R. Deschamps, M. E. Lassman and H. Mattoussi. *J. Am. Chem. Soc.*, 2005, **127**, 6744-6751.
26. Y. Xia, L. Song and C. Zhu. *Anal. Chem.*, 2011, **83**, 1401-1407.
27. J. R. Cox, P. MüLler and T. M. Swager. *J. Am. Chem. Soc.*, 2011, **133**, 12910-12913.
28. D. A. Olley, E. J. Wren, G. Vamvounis, M. J. Fernee, X. Wang, P. L. Burn, P. Meredith and P. E. Shaw. *Chem. Mater.*, 2011, **23**, 789-794.
29. T. M. Swager. *Acc. Chem. Res.*, 1998, **31**, 201-207.
30. J. S. Yang and T. M. Swager. *J. Am. Chem. Soc.*, 1998, **120**, 5321-5322.
31. S. Rochat and T. M. Swager. *ACS Appl. Mater. Interfaces*, 2013, **5**, 4488-4502.
32. J.-S. Yang and T. M. Swager. *J. Am. Chem. Soc.*, 1998, **120**, 11864-11873.
33. Y. Hong, J. W. Y. Lam and B. Z. Tang. *Chem. Commun.*, 2009, 4332-4353.
34. Z. Li, Y. Q. Dong, J. W. Y. Lam, J. Sun, A. Qin, M. Häußler, Y. P. Dong, H. H. Y. Sung, I. D. Williams, H. S. Kwok and B. Z. Tang. *Adv. Funct. Mater.*, 2009, **19**, 905-917.

35. Y. Z. Liao, V. Strong, Y. Wang, X.-G. Li, X. Wang and R. B. Kaner. *Adv. Funct. Mater.*, 2012, **22**, 726-735.
36. K. K. Kartha, S. S. Babu, S. Srinivasan and A. Ajayaghosh. *J. Am. Chem. Soc.*, 2012, **134**, 4834-4841.
37. L. Ding and Y. Fang. *Chem. Soc. Rev.*, 2010, **39**, 4258-4273.
38. Y. Wang, A. La, Y. Ding, Y. Liu and Y. Lei. *Adv. Funct. Mater.*, 2012, **22**, 3547-3555.
39. S. Content, W. C. Trogler and M. J. Sailor. *Chem. Eur. J.*, 2000, **6**, 2205-2213.
40. K. Zhang, H. Zhou, Q. Mei, S. Wang, G. Guan, R. Liu, J. Zhang and Z. Zhang. *J. Am. Chem. Soc.*, 2011, **133**, 8424-8427.
41. A. Mathew, P. Sajanlal and T. Pradeep. *Angew. Chem. Int. Ed.*, 2012, **51**, 9596-9600.
42. Q. Niu, K. Gao, Z. Lin and W. Wu. *Anal. Methods*, 2013, **5**, 6228-6233.
43. H. Du, G. He, T. Liu, L. Ding and Y. Fang. *J. Photochem. Photobiol., A*, 2011, **217**, 356-362.
44. L. Ding, Y. Liu, Y. Cao, L. Wang, Y. Xin and Y. Fang. *J. Mater. Chem.*, 2012, **22**, 11574-11582.
45. S. Zhang, L. Ding, F. Lü, T. Liu and Y. Fang. *Spectrochim. Acta, Part A*, 2012, **97**, 31-37.
46. G. B. Demirel, B. Daglar and M. Bayindir. *Chem. Commun.*, 2013, **49**, 6140-6142.
47. W. Zhu, C. Wang, W. Li, C. A. Tao, J. Cui, H. Yang, Y. Jiang and G. Li. *J. Mater. Chem. A*, 2013, **1**, 11741-11747.
48. T. Naddo, Y. Che, W. Zhang, K. Balakrishnan, X. Yang, M. Yen, J. Zhao, J. S. Moore and L. Zang. *J. Am. Chem. Soc.*, 2007, **129**, 6978-6979.
49. S. Shanmugaraju, S. A. Joshi and P. S. Mukherjee. *Inorg. Chem.*, 2011, **50**, 11736-11745.
50. G. Tang, S. S. Y. Chen, P. E. Shaw, K. Hegedus, X. Wang, P. L. Burn and P. Meredith. *Polym. Chem.*, 2011, **2**, 2360-2368.
51. B. Gole, S. Shanmugaraju, A. K. Bar and P. S. Mukherjee. *Chem. Commun.*, 2011, **47**, 10046-10048.
52. Z. Hu, B. J. Deibert and J. Li. *Chem. Soc. Rev.*, 2014, **43**, 5815-5840.
53. M. Lan, J. Zhang, Y.-S. Chui, H. Wang, Q. Yang, X. Zhu, H. Wei, W. Liu, J. Ge, P. Wang, X. Chen, C.-S. Lee and W. Zhang. *J. Mater. Chem. B*, 2015, **3**, 127-134.
54. B. Gole, A. K. Bar and P. S. Mukherjee. *Chem. Eur. J.*, 2014, **20**, 13321-13336.
55. S. S. Nagarkar, A. V. Desai and S. K. Ghosh. *Chem. Commun.*, 2014, **50**, 8915-8918.
56. A. Gingras, J. Sarette, E. Shawler, T. Lee, S. Freund, E. Holwitt and B. W. Hicks. *Biosens. Bioelectron.*, 2013, **48**, 251-257.
57. Y. Ma, S. Wang and L. Wang. *Trends Anal. Chem.*, 2015, **65**, 13-21.
58. R. Li, Y. P. Yuan, L. G. Qiu, W. Zhang and J. F. Zhu. *Small*, 2012, **8**, 225-230.
59. Y. Xu, Y. Wen, W. Zhu, Y. N. Wu, C. Lin and G. Li. *Mater. Lett.*, 2012, **87**, 20-23.
60. S. B. Ding, W. Wang, L. G. Qiu, Y. P. Yuan, F. M. Peng, X. Jiang, A. J. Xie, Y. H. Shen and J. F. Zhu. *Mater. Lett.*, 2011, **65**, 1385-1387.
61. J. J. Qian, L. G. Qiu, Y. M. Wang, Y. P. Yuan, A. J. Xie and Y. H. Shen. *Dalton Trans.*, 2014, **43**, 3978-3983.
62. W. Zhang, L. G. Qiu, Y. P. Yuan, A. J. Xie, Y. H. Shen and J. F. Zhu. *J. Hazard. Mater.*, 2012, **221-222**, 147-154.
63. M. Jurcic, W. J. Peveler, C. N. Savory, D. O. Scanlon, A. J. Kenyon and I. P. Parkin. *J. Mater. Chem. A*, 2015, **3**, 6351-6359.
64. C. E. Agudelo-Morales, R. E. Galian and J. Pérez-Prieto. *Anal. Chem.*, 2012, **84**, 8083-8087.
65. K.-Y. Hua, C.-M. Deng, C. He, L.-Q. Shi, D.-F. Zhu, Q.-G. He and J.-G. Cheng. *Chin. Chem. Lett.*, 2013, **24**, 643-646.
66. H. Li, J. Wang, Z. Pan, L. Cui, L. Xu, R. Wang, Y. Song and L. Jiang. *J. Mater. Chem.*, 2011, **21**, 1730-1735.
67. S. N. Baker and G. A. Baker. *Angew. Chem. Int. Ed.*, 2010, **49**, 6726-6744.

68. V. Bhalla, A. Gupta, M. Kumar, D. S. S. Rao and S. K. Prasad. *ACS Appl. Mater. Interfaces*, 2013, **5**, 672-679.
69. R. Freeman, T. Finder, L. Bahshi, R. Gill and I. Willner. *Adv. Mater.*, 2012, **24**, 6416-6421.
70. H.-S. Jang, Y. Wang, Y. Lei and M.-P. Nieh. *J. Phys. Chem. C*, 2013, **117**, 1428-1435.
71. D. Zhao and T. M. Swager. *Macromolecules*, 2005, **38**, 9377-9384.
72. G. Widawski, M. Rawiso and B. Francois. *Nature*, 1994, **369**, 387-389.
73. M. Srinivasarao, D. Collings, A. Philips and S. Patel. *Science*, 2001, **292**, 79-83.
74. T. Hayakawa and S. Horiuchi. *Angew. Chem. Int. Ed.*, 2003, **42**, 2285-2289.
75. U. H. F. Bunz. *Adv. Mater.*, 2006, **18**, 973-989.
76. M. H. Stenzel, C. Barner-Kowollik and T. P. Davis. *J. Polym. Sci. Part A Polym. Chem.*, 2006, **44**, 2363-2375.
77. E. Ferrari, P. Fabbri and F. Pilati. *Langmuir*, 2011, **27**, 1874-1881.
78. M. S. Park and J. K. Kim. *Langmuir*, 2004, **20**, 5347-5352.
79. W. Madej, A. Budkowski, J. Raczkowska and J. Rysz. *Langmuir*, 2008, **24**, 3517-3524.
80. J. Peng, Y. Han, Y. Yang and B. Li. *Polymer*, 2004, **45**, 447-452.
81. B. You, L. Shi, N. Wen, X. Liu, L. Wu and J. Zi. *Macromolecules*, 2008, **41**, 6624-6626.
82. G. Yildirim, S. D. Senol, M. Dogruer, O. Ozturk, A. Senol, A. T. Tasci and C. Terzioglu. *Spectrochim. Acta, Part A*, 2012, **85**, 271-282.
83. A. Vu, J. Phillips, P. Bühlmann and A. Stein. *Chem. Mater.*, 2013, **25**, 711-722.
84. T. Liu, L. Ding, K. Zhao, W. Wang and Y. Fang. *J. Mater. Chem.*, 2012, **22**, 1069-1077.
85. L. A. Lucas, D. M. Delongchamp, L. J. Richter, R. J. Kline, D. A. Fischer, B. R. Kaafarani and G. E. Jabbour. *Chem. Mater.*, 2008, **20**, 5743-5749.
86. J. You, J. A. Yoon, J. Kim, C.-F. Huang, K. Matyjaszewski and E. Kim. *Chem. Mater.*, 2010, **22**, 4426-4434.
87. S. Lee, B. L. Chen, D. C. Fredrickson, F. J. Disalvo, E. Lobkovsky and J. A. Adams. *Chem. Mater.*, 2003, **15**, 1420-1433.
88. T. Devic, M. Yuan, J. Adams, D. C. Fredrickson, S. Lee and D. Venkataraman. *J. Am. Chem. Soc.*, 2005, **127**, 14616-14627.
89. M. Vybornyi, A. V. Rudnev, S. M. Langenegger, T. Wandlowski, G. Calzaferri and R. Häner. *Angew. Chem. Int. Ed.*, 2013, **52**, 11488-11493.
90. V. D. Deepak and S. K. Asha. *J. Phys. Chem. B*, 2009, **113**, 11887-11897.
91. Y. Zhu, M. M. Alam and S. A. Jenekhe. *Macromolecules*, 2002, **35**, 9844-9846.
92. K. Kawasumi, Q. Zhang, Y. Segawa, L. T. Scott and K. Itami. *Nat. Chem.*, 2013, **5**, 739-744.
93. J. Tauc, R. Grigorovici and A. Vancu. *Phys. Status Solidi B*, 1966, **15**, 627-637.
94. H. Usta, C. Risko, Z. Wang, H. Huang, M. K. Deliomeroglu, A. Zhukhovitskiy, A. Facchetti and T. J. Marks. *J. Am. Chem. Soc.*, 2009, **131**, 5586-5608.
95. Y. F. Li, Y. Cao, J. Gao, D. L. Wang, G. Yu and A. J. Heeger. *Synth. Met.*, 1999, **99**, 243-248.
96. J. L. Bredas, R. Silbey, D. S. Boudreaux and R. R. Chance. *J. Am. Chem. Soc.*, 1983, **105**, 6555-6559.
97. Z. K. Chen, W. Huang, L. H. Wang, E. T. Kang, B. J. Chen, C. S. Lee and S. T. Lee. *Macromolecules*, 2000, **33**, 9015-9025.
98. S. W. Hwang and Y. Chen. *Macromolecules*, 2002, **35**, 5438-5443.
99. S. Hwang, J. H. Lee, C. Park, H. Lee, C. Kim, C. Park, M.-H. Lee, W. Lee, J. Park, K. Kim, N.-G. Park and C. Kim. *Chem. Commun.*, 2007, 4887-4889.
100. M. Suresh, A. K. Mandal, E. Suresh and A. Das. *Chem. Sci.*, 2013, **4**, 2380-2386.
101. J. Zhao, T. Luo, X. Zhang, Y. Lei, K. Gong and Y. Yan. *Anal. Chem.*, 2012, **84**, 6303-6307.

102. C. Sánchez, H. Carlsson, A. Colmsjö, C. Crescenzi and R. Batlle. *Anal. Chem.*, 2003, **75**, 4639-4645.
103. M. K. Habib. *Biosens. Bioelectron.*, 2007, **23**, 1-18.
104. M. S. Atanassova and G. D. Dimitrov. *Spectrochim. Acta, Part A*, 2003, **59**, 1655-1662.
105. L. M. Hanssen and C. Zhu. in *Handbook of Vibrational Spectroscopy* (John Wiley & Sons, Ltd, 2006).
106. Y. Zhang, S. Yuan, W. Zhou, J. Xu and Y. Li. *J. Nanosci. Nanotechnol.*, 2007, **7**, 2366-2375.
107. A. M. Heyns and G. J. Van Schalkwyk. *Spectrochim. Acta, Part A*, 1973, **29**, 1163-1175.
108. H. Shinohara, Y. Yamakita and K. Ohno. *J. Mol. Struct.*, 1998, **442**, 221-234.
109. O. Péron, E. Rinnert, M. Lehaitre, P. Crassous and C. Compère. *Talanta*, 2009, **79**, 199-204.
110. E. Celia, T. Darmanin, E. Taffin De Givenchy, S. Amigoni and F. Guittard. *J. Colloid Interface Sci.*, 2013, **402**, 1-18.
111. C. J. Cumming, C. Aker, M. Fisher, M. Fox, M. J. La Grone, D. Reust, M. G. Rockley, T. M. Swager, E. Towers and V. Williams. *IEEE Transactions on Geoscience and Remote Sensing*, 2001, **39**, 1119-1128.
112. X. Sun, C. Brückner, M.-P. Nieh and Y. Lei. *J. Mater. Chem. A*, 2014, **2**, 14613-14621.
113. X. Sun, Y. Liu, S. Mopidevi, Y. Meng, F. Huang, J. Parisi, M.-P. Nieh, C. Cornelius, S. L. Suib and Y. Lei. *Sens. Actuators, B*, 2014, **195**, 52-57.
114. A. Greiner and J. H. Wendorff. *Angew. Chem. Int. Ed.*, 2007, **46**, 5670-5703.
115. N. Bhardwaj and S. C. Kundu. *Biotechnol. Adv.*, 2010, **28**, 325-347.
116. X. Wang, C. Drew, S.-H. Lee, K. J. Senecal, J. Kumar and L. A. Samuelson. *Nano Lett.*, 2002, **2**, 1273-1275.
117. Y. Long, H. Chen, Y. Yang, H. Wang, Y. Yang, N. Li, K. Li, J. Pei and F. Liu. *Macromolecules*, 2009, **42**, 6501-6509.
118. Z. Tang, C. Qiu, J. R. Mccutcheon, K. Yoon, H. Ma, D. Fang, E. Lee, C. Kopp, B. S. Hsiao and B. Chu. *J. Polym. Sci. Part B Polym. Phys.*, 2009, **47**, 2288-2300.
119. H. Fong, I. Chun and D. Reneker. *Polymer*, 1999, **40**, 4585-4592.
120. R. Nirmala, H. R. Panth, C. Yi, K. T. Nam, S.-J. Park, H. Y. Kim and R. Navamathavan. *Macromol. Res.*, 2010, **18**, 759-765.
121. C. Luo, M. Nangrejo and M. Edirisinghe. *Polymer*, 2010, **51**, 1654-1662.
122. X. Yuan, Y. Zhang, C. Dong and J. Sheng. *Polym. Int.*, 2004, **53**, 1704-1710.
123. W. Wei, J.-T. Yeh, P. Li, M.-R. Li, W. Li and X.-L. Wang. *J. Appl. Polym. Sci.*, 2010, **118**, 3005-3012.
124. Z. Qi, H. Yu, Y. Chen and M. Zhu. *Mater. Lett.*, 2009, **63**, 415-418.
125. E. Antoniou and P. Alexandridis. *Eur. Polym. J.*, 2010, **46**, 324-335.
126. N. Choktaweesap, K. Arayanarakul, D. Aht-Ong, C. Meechaisue and P. Supaphol. *Polym. J.*, 2007, **39**, 622-631.
127. H.-C. Chen, C.-H. Tsai and M.-C. Yang. *J. Polym. Res.*, 2011, **18**, 319-327.
128. T. Yang, D. Wu, L. Lu, W. Zhou and M. Zhang. *Polym. Compos.*, 2011, **32**, 1280-1288.
129. P. Beyazkilic, A. Yildirim and M. Bayindir. *ACS Appl. Mater. Interfaces*, 2014, **6**, 4997-5004.
130. X. Sun, X. Ma, C. V. Kumar and Y. Lei. *Anal. Methods*, 2014, **6**, 8464-8468.
131. N. Venkatramaiah, S. Kumar and S. Patil. *Chem. Commun.*, 2012, **48**, 5007-5009.
132. K.-S. Focsaneanu and J. Scaiano. *Photochem. Photobiol. Sci.*, 2005, **4**, 817-821.
133. L. Fan, Y. Hu, X. Wang, L. Zhang, F. Li, D. Han, Z. Li, Q. Zhang, Z. Wang and L. Niu. *Talanta*, 2012, **101**, 192-197.
134. S. Dalapati, S. Jin, J. Gao, Y. Xu, A. Nagai and D. Jiang. *J. Am. Chem. Soc.*, 2013, **135**, 17310-17313.

135. X. Sun, Y. Liu, G. Shaw, A. Carrier, S. Dey, J. Zhao and Y. Lei. *ACS Appl. Mater. Interfaces*, 2015, **7**, 13189-13197.
136. M. J. Krysmann, A. Kelarakis, P. Dallas and E. P. Giannelis. *J. Am. Chem. Soc.*, 2012, **134**, 747-750.
137. S. Zhu, Q. Meng, L. Wang, J. Zhang, Y. Song, H. Jin, K. Zhang, H. Sun, H. Wang and B. Yang. *Angew. Chem. Int. Ed.*, 2013, **52**, 3953-3957.
138. S. Qu, X. Wang, Q. Lu, X. Liu and L. Wang. *Angew. Chem. Int. Ed.*, 2012, **51**, 12215-12218.
139. H. Zhu, X. Wang, Y. Li, Z. Wang, F. Yang and X. Yang. *Chem. Commun.*, 2009, 5118-5120.
140. H. Liu, Z. He, L.-P. Jiang and J.-J. Zhu. *ACS Appl. Mater. Interfaces*, 2015, **7**, 4913-4920.
141. X. Zhai, P. Zhang, C. Liu, T. Bai, W. Li, L. Dai and W. Liu. *Chem. Commun.*, 2012, **48**, 7955-7957.
142. G. Sandeep Kumar, R. Roy, D. Sen, U. K. Ghorai, R. Thapa, N. Mazumder, S. Saha and K. K. Chattopadhyay. *Nanoscale*, 2014, **6**, 3384-3391.
143. B. Kong, A. Zhu, C. Ding, X. Zhao, B. Li and Y. Tian. *Adv. Mater.*, 2012, **24**, 5844-5848.
144. A. B. Bourlinos, A. Stassinopoulos, D. Anglos, R. Zboril, M. Karakassides and E. P. Giannelis. *Small*, 2008, **4**, 455-458.
145. Z. Yang, M. Xu, Y. Liu, F. He, F. Gao, Y. Su, H. Wei and Y. Zhang. *Nanoscale*, 2014, **6**, 1890-1895.
146. Y. Dong, H. Pang, H. B. Yang, C. Guo, J. Shao, Y. Chi, C. M. Li and T. Yu. *Angew. Chem. Int. Ed.*, 2013, **52**, 7800-7804.
147. X. Chen, Q. Jin, L. Wu, C. Tung and X. Tang. *Angew. Chem. Int. Ed.*, 2014, **53**, 12542-12547.
148. Z.-C. Yang, X. Li and J. Wang. *Carbon*, 2011, **49**, 5207-5212.
149. X. Jia, J. Li and E. Wang. *Nanoscale*, 2012, **4**, 5572-5575.
150. C. Shen, Y. Sun, J. Wang and Y. Lu. *Nanoscale*, 2014, **6**, 9139-9147.
151. S. Y. Lim, W. Shen and Z. Gao. *Chem. Soc. Rev.*, 2015, **44**, 362-381.
152. X. Wang, L. Cao, F. Lu, M. J. Meziani, H. Li, G. Qi, B. Zhou, B. A. Harruff, F. Kermarrec and Y.-P. Sun. *Chem. Commun.*, 2009, 3774-3776.
153. J. Liu, Y. Zhong, P. Lu, Y. Hong, J. W. Y. Lam, M. Faisal, Y. Yu, K. S. Wong and B. Z. Tang. *Polym. Chem.*, 2010, **1**, 426-429.
154. R. Lu and S. Tang. *J. Mater. Chem. A*, 2015.
155. G. He, H. Peng, T. Liu, M. Yang, Y. Zhang and Y. Fang. *J. Mater. Chem.*, 2009, **19**, 7347-7353.
156. M. Rong, L. Lin, X. Song, T. Zhao, Y. Zhong, J. Yan, Y. Wang and X. Chen. *Anal. Chem.*, 2015, **87**, 1288-1296.
157. S. Hu, A. Trinchi, P. Atkin and I. Cole. *Angew. Chem. Int. Ed.*, 2015, **54**, 2970-2974.
158. S. H. Jin, D. H. Kim, G. H. Jun, S. H. Hong and S. Jeon. *ACS Nano*, 2013, **7**, 1239-1245.
159. Y. Fang, S. Guo, D. Li, C. Zhu, W. Ren, S. Dong and E. Wang. *ACS Nano*, 2012, **6**, 400-409.
160. S. K. Bhunia, A. Saha, A. R. Maity, S. C. Ray and N. R. Jana. *Sci. Rep.*, 2013, **3**.
161. J. Zhou, P. Lin, J. Ma, X. Shan, H. Feng, C. Chen, J. Chen and Z. Qian. *R. Soc. Chem. Adv.*, 2013, **3**, 9625-9628.
162. S. Zhu, J. Zhang, C. Qiao, S. Tang, Y. Li, W. Yuan, B. Li, L. Tian, F. Liu, R. Hu, H. Gao, H. Wei, H. Zhang, H. Sun and B. Yang. *Chem. Commun.*, 2011, **47**, 6858-6860.
163. L. Zhang, Z.-Y. Zhang, R.-P. Liang, Y.-H. Li and J.-D. Qiu. *Anal. Chem.*, 2014, **86**, 4423-4430.
164. S. Jahan, F. Mansoor, S. Naz, J. Lei and S. Kanwal. *Anal. Chem.*, 2013, **85**, 10232-10239.
165. H. Ding, J.-S. Wei and H.-M. Xiong. *Nanoscale*, 2014, **6**, 13817-13823.
166. J. Zhang, Z. Zhao, Z. Xia and L. Dai. *Nat. Nanotechnol.*, 2015, **10**, 444-452.

167. X. Yan, Y. Yu, S.-K. Ryu, J. Lan, X. Jia and X. Yang. *Electrochim. Acta*, 2014, **136**, 466-472.
168. J. Stejskal, P. Kratochvíl and N. Radhakrishnan. *Synth. Met.*, 1993, **61**, 225-231.
169. X. Gong, Q. Hu, M. C. Paau, Y. Zhang, S. Shuang, C. Dong and M. M. F. Choi. *Nanoscale*, 2014, **6**, 8162-8170.
170. W. Wang, Y. Li, L. Cheng, Z. Cao and W. Liu. *J. Mater. Chem. B*, 2014, **2**, 46-48.
171. L. Wang, S.-J. Zhu, H.-Y. Wang, S.-N. Qu, Y.-L. Zhang, J.-H. Zhang, Q.-D. Chen, H.-L. Xu, W. Han, B. Yang and H.-B. Sun. *ACS Nano*, 2014, **8**, 2541-2547.
172. D. Yu, Y. Xue and L. Dai. *J. Phys. Chem. Lett.*, 2012, **3**, 2863-2870.
173. N. Ranjbar Sahraie, J. P. Paraknowitsch, C. Göbel, A. Thomas and P. Strasser. *J. Am. Chem. Soc.*, 2014, **136**, 14486-14497.
174. E. Cruz-Silva, D. A. Cullen, L. Gu, J. M. Romo-Herrera, E. Muñoz-Sandoval, F. López-Urías, B. G. Sumpter, V. Meunier, J.-C. Charlier, D. J. Smith, H. Terrones and M. Terrones. *ACS Nano*, 2008, **2**, 441-448.
175. E. Gelamo and M. Tabak. *Spectrochim. Acta, Part A*, 2000, **56**, 2255-2271.
176. Y.-J. Hu, Y. Liu, L.-X. Zhang, R.-M. Zhao and S.-S. Qu. *J. Mol. Struct.*, 2005, **750**, 174-178.
177. A. Papadopoulou, R. J. Green and R. A. Frazier. *J. Agric. Food Chem.*, 2005, **53**, 158-163.
178. Y. Peng, A.-J. Zhang, M. Dong and Y.-W. Wang. *Chem. Commun.*, 2011, **47**, 4505-4507.
179. X.-G. Hou, Y. Wu, H.-T. Cao, H.-Z. Sun, H.-B. Li, G.-G. Shan and Z.-M. Su. *Chem. Commun.*, 2014, **50**, 6031-6034.
180. Y. Xu, B. Li, W. Li, J. Zhao, S. Sun and Y. Pang. *Chem. Commun.*, 2013, **49**, 4764-4766.
181. D. Li, J. Liu, R. T. K. Kwok, Z. Liang, B. Z. Tang and J. Yu. *Chem. Commun.*, 2012, **48**, 7167-7169.
182. Y. Ma, H. Li, S. Peng and L. Wang. *Anal. Chem.*, 2012, **84**, 8415-8421.
183. N. Shahabadi and M. Maghsudi. *J. Mol. Struct.*, 2009, **929**, 193-199.
184. C. J. Mchugh, W. E. Smith, R. Lacey and D. Graham. *Chem. Commun.*, 2002, 2514-2515.
185. A. Tournebize, P. Wong-Wah-Chung, S. Thérias, P. O. Bussière, A. Rivaton, T. Caron, F. Serein-Spirau, J. P. Lère-Porte, P. Montméat and J. L. Gardette. *Polym. Degrad. Stab.*, 2012, **97**, 1355-1365.
186. J. Geng, P. Liu, B. Liu, G. Guan, Z. Zhang and M.-Y. Han. *Chem. Eur. J.*, 2010, **16**, 3720-3727.
187. Q. Fang, J. Geng, B. Liu, D. Gao, F. Li, Z. Wang, G. Guan and Z. Zhang. *Chem. Eur. J.*, 2009, **15**, 11507-11514.
188. L. Zhang, Y. Han, J. Zhu, Y. Zhai and S. Dong. *Anal. Chem.*, 2015, **87**, 2033-2036.
189. B. Balan, C. Vijayakumar, M. Tsuji, A. Saeki and S. Seki. *J. Phys. Chem. B*, 2012, **116**, 10371-10378.
190. J. L. Pablos, L. A. Sarabia, M. C. Ortiz, A. Mendía, A. Muñoz, F. Serna, F. C. García and J. M. García. *Sens. Actuators, B*, 2015, **212**, 18-27.
191. M. A. Ali, S. S. Y. Chen, H. Cavaye, A. G. R. Smith, P. L. Burn, I. R. Gentle, P. Meredith and P. E. Shaw. *Sens. Actuators, B*, 2015, **210**, 550-557.

Appendix A

Biography

Xiangcheng Sun was born on May 18th, 1986 in Xi'an, Shaanxi, China. He received his B.E. in Environmental Engineering in Harbin Institute of Technology, China in June 2008, and M.E. in Environmental Engineering in Graduate University of Chinese of Academy of Sciences in June 2011. In August 2011, Xiangcheng was admitted to the Department of Chemical and Biomolecular Engineering, University of Connecticut, where he will obtain his Ph.D. in Chemical Engineering in August 2015.

Appendix B

Patents, Journal Publications and Conference Presentations

Patents

1) Y. Lei, **Xiangcheng Sun**. Synthesis of nitrogen and phosphorus co-doped, fluorescent carbon dots with high quantum yield and dual fluorescence emission. Disclosure for US Provisional Patent, 2015.
2) Y. Lei, **Xiangcheng Sun**. Fluorescent polymer film with three-dimensionally ordered nanoporous array for sensitive and selective explosive detection. Disclosure for US Provisional Patent, 2014.

Journal Publications

1) **Xiangcheng Sun**, Y. Lei, et al. Synthesis, characterization and application of fluorescent carbon dots with high quantum yield and dual fluorescence emission. Nanoscale. 2015. (Under Preparation)
2) **Xiangcheng Sun**, Y. Lei, et al. Microwave-assisted ultrafast and facile synthesis of fluorescent carbon nanoparticles from single precursor: Preparation, characterization and its application for highly selective detection of explosive picric acid. Journal of Materials Chemistry A. 2015. (Submitted)
3) **Xiangcheng Sun**, Y. Wang, Y. Lei. Fluorescence based explosives detection: from mechanisms to sensory materials. Chemical Society Reviews. 2015. (Minor Revision)
4) **Xiangcheng Sun**, Y. Liu, G. Shaw, A. Carrier, S. Dey, J. Zhao, Y. Lei. Fundamental study of electrospun pyrene-polythersulfone nanofibers using mixed solvents for sensitive and selective explosives detection in aqueous solution. ACS Applied Materials and Interfaces. 2015(7): 13189-13197.
5) **Xiangcheng Sun**, X. Ma, C.V. Kumar, Y. Lei. Protein-based sensitive, selective and rapid fluorescence detection of picric acid in aqueous media. Analytical Methods. 2014(6): 8464-8468.

6) **Xiangcheng Sun**, C. Brückner, M. Nieh, Y. Lei. A fluorescent polymer film with self-assembled three-dimensionally ordered nanopores: preparation, characterization and its application for explosives detection. Journal of Materials Chemistry A. 2014(2): 14613-14621.
7) **Xiangcheng Sun**, Y. Liu, S. Mopidevi, Y. Meng, F. Huang, J. Parisi, M. Nieh, C. Cornelius, S.L. Suib, Y. Lei. Super-hydrophobic "smart" sand for buried explosive detection. Sensors and Actuators B. 2014(195): 52-57.
8) **Xiangcheng Sun**, Y. Liu, H. Gao, P. Gao, Y. Lei. Bimodular high temperature planar oxygen gas sensor. Frontiers in Chemistry. 2014(2): 1-7.
9) **Xiangcheng Sun**, S. Stagon, H. Huang, J. Chen, Y. Lei. Functionalized aligned silver nanorod arrays for glucose sensing through surface enhanced Raman scattering. RSC Advances. 2014(4): 23382-23388.
10) Y. Liu, **Xiangcheng Sun**, Z. Zhou, Y. Lei. Electrospun Ce-Ni-O composite nanofibers for highly selective propane detection at high temperature based on its rapid reaction kinetics. Journal of Materials Chemistry A. 2014(2): 14038-14047.
11) Y. Liu, **Xiangcheng Sun**, Y. Lei. Tunable p-n transition behaviour of p-$La_{0.67}Sr_{0.33}MnO_3$/n-CeO_2 nanofibers heterojunction for the development of selective high temperature propane sensor. Journal of Materials Chemistry A. 2014(2): 11651-11659.
12) Y. Liu, J. Parisi, **Xiangcheng Sun**, B. Li, Y. Lei. Solid-state gas sensors for high temperature application – a review. Journal of Materials Chemistry A. 2014(2): 9919-9943.

Conference Presentations

1) **Xiangcheng Sun**, K. Fu, W. Huang. Reinforced Cellulose for Sustainable Structures. BASF North American Science Competition, Jun. 4-5, 2015, Florham Park, NJ.
2) **Xiangcheng Sun**, Y. Lei. Polymer Doped Pyrene Nanomaterials Based Fluorescence Sensors for Nitro-explosives Detection. Graduate Student Poster Reception, Apr. 17, 2015. Storrs, CT.
3) **Xiangcheng Sun**, Y. Liu, G. Shaw, Y. Lei. Electrospun Nanofiber Sensor for Sensitive and Selective Sensing of Nitro-Based Explosives in Aqueous Solution. AIChE Annual Meeting, Nov. 16-21, 2014. Atlanta, GA.

4) **Xiangcheng Sun**, C. Brückner, M. Nieh, Y. Lei. Properties of Fluorescent Polymer Film with Three-Dimensionally Ordered Nanopores and Its Application in Explosive Detection. AIChE Annual Meeting, Nov. 16-21, 2014. Atlanta, GA.
5) **Xiangcheng Sun**, Y. Lei. Portable, Naked Eye-based, Ultrasensitive Explosive Vapors Detector. NSF SBIR/STTR 2014 Phase II Grantee Conference, May 12-15, 2014. Baltimore, MD.
6) **Xiangcheng Sun**, S. Stagon, H. Huang, Y. Lei. Glucose detection using functionalized silver nanorods surface through surface enhanced Raman scattering. 23rd Annual CMOC Symposium, Apr. 9, 2014. Storrs, CT.
7) G. Shaw, **Xiangcheng Sun**, Y. Lei. Fluorescence nitro-explosive detection through electrospun Pyrene-PES nanofibers. AIChE Annual Meeting, Nov. 16-21, 2014. Atlanta, GA.
8) **Xiangcheng Sun**, S. Mopidevi, Y. Liu, C. Silhavy, Y. Lei, M. Nieh. "Smart" sand for buried explosive detection by naked eye under handheld UV light. AIChE Annual Meeting, Nov. 3-8, 2013. San Francisco, CA.
9) **Xiangcheng Sun**, Y. Liu, H. Gao, Y. Lei, P. Gao. Bimodular high temperature planar oxygen gas sensor. AIChE Annual Meeting, Nov. 3-8, 2013. San Francisco, CA.
10) Y. Liu, **Xiangcheng Sun**, Y. Lei. Oxide nanofibers for high temperature sensing. AIChE Annual Meeting, Nov. 3-8, 2013. San Francisco, CA.
11) **Xiangcheng Sun**, H. Gao, Y. Liu, P. Gao, Y. Lei. High temperature potentiometric O_2 sensor based on stabilized zirconia and NiO electrode. AIChE Annual Meeting, Oct. 28-Nov. 2, 2012. Pittsburgh, PA.
12) **Xiangcheng Sun**, H. Gao, Y. Liu, P. Gao, Y. Lei. High temperature potentiometric type gas sensors. 21st Annual CMOC Symposium, Apr. 11, 2012. Storrs, CT.